The Dissertation Committee for Corwin Grant Olson
certifies that this is the approved version of the following dissertation:

Sequential Estimation Methods for Small Body Optical Navigation

Committee:

Ryan P. Russell, Supervisor

Maruthi R. Akella

Srinivas V. Bettadpur

Shyamkumar Bhaskaran

J. Russell Carpenter

Wallace T. Fowler

Sequential Estimation Methods for Small Body Optical Navigation

by

Corwin Grant Olson, B.S.As.E., M.S.E.

DISSERTATION

Presented to the Faculty of the Graduate School of
The University of Texas at Austin
in Partial Fulfillment
of the Requirements
for the Degree of

DOCTOR OF PHILOSOPHY

The University of Texas at Austin
August 2016

To my wife Lindsey

Acknowledgments

There are many, many people to thank for all they have done to help me on this journey to obtain my PhD. This accomplishment would not have been possible without their extensive help and encouragement.

First I must thank the members of my dissertation committee. And I must begin by thanking my advisor, Dr. Ryan Russell. He greatly assisted me in my graduate fellowship application even before he knew if I would choose to work with him at UT, and that generosity with his time and energy during even his busiest days has continued to impress me. He has been a source of invaluable guidance and inspiration since those early days.

Dr. Russell Carpenter I first met in 2007 when I worked at Goddard as an intern, and we worked together extensively on the NASA Magnetospheric Multiscale mission for several years. I learned through him of the wonderful NASA fellowship that I would receive for graduate studies during my PhD, and he would go on to serve as the primary NASA collaborator for the fellowship as well. His technical guidance and friendship has been enormously valuable to me.

I met Dr. Shyam Bhaskaran in 2007 as well, in one of the great serendipitous moments of my career. During an External Advisory Committee social event aboard a riverboat cruise, I sat next to him and we began discussing my research interests for graduate school. I mentioned I had recently started read-

ing about an onboard autonomous navigation system called AutoNav, which I was considering further researching. He then proceeded to tell me he was the chief architect of that system! He encouraged me to come intern at JPL, which I would do the following summer and which would turn into my key initial experience working on optical navigation around small bodies. This experience would evolve into the focus of my Masters Thesis, and would serve as a strong foundation for my successful NASA graduate fellowship application. In addition to the wonderful opportunities he has provided to me, he has been a wonderful advisor and teacher.

Dr. Wallace Fowler served on my Masters Thesis committee in 2009, and we first met when he was my instructor in a freshman seminar course in the Fall of 2002. I can confidently say he has been one of the most consistently great teachers I've had during all my years in the department. I've also taken several excellent courses from Dr. Maruthi Akella dating back to my undergraduate days in the UT Aerospace department, and Dr. Srinivas Bettadpur I have very much enjoyed working with since I returned to UT for my PhD.

There have been many others outside of my committee that have provided extensive technical assistance and guidance, including Kenny Getzandanner and Kevin Berry of NASA Goddard Space Flight Center. I must also thank those people who encouraged me to return for my PhD, when there were many other easier paths I could have followed, including Dr. Anne Long and Khashayar Parsay.

I have had the great privilege of possessing wonderful financial support from numerous sources throughout this experience. The work described in this dissertation was primarily funded by NASA's Chief Technology Office through a NASA Space Technology Research Fellowship (NSTRF), which also provided invaluable travel experiences to several NASA centers throughout my PhD program. These experiences would prove essential for obtaining specific research ideas that are not only novel contributions to the field of navigation, but also valuable to future NASA missions. I am also very grateful for the Thrust 2000 Fellowship I received from the Cockrell School of Engineering, as well as the UT Graduate Dean's Prestigious Fellowship.

I thank the many great friends I have made in the aerospace department during my PhD program, and in particular those within the Russell research group. I especially thank everyone that I spent countless hours studying with for qualifying exams: those friendships are forged in a very strong shared experience. I also want to deeply thank my parents for serving as amazing role models both during this PhD program and all the prior years of my life, as well my sister who has been a wonderful listener of all my daily graduate school tribulations.

Finally, and most importantly, I thank my wife Lindsey for her unending support and love during this experience. From the evening three days before our wedding when we made the fateful decision to return to UT for my PhD, to the present day as she cares for our newborn son Grant while I finish up this degree, she has been the bedrock and love of my life.

Sequential Estimation Methods for Small Body Optical Navigation

by

Corwin Grant Olson, Ph.D.
The University of Texas at Austin, 2016
SUPERVISOR: Ryan P. Russell

As humans explore further into the solar system, small bodies such as asteroids and comets serve as critical stepping-stone destinations. Highly accurate navigation about these small bodies is critical for any future missions, and as a result is listed prominently among NASA's future goals in the NASA Office of Chief Technologist Roadmap. Due to the long communication light-time delays with the Earth, advances in small body navigation may enable missions currently not feasible, as well as significantly reduce dependence on ground resources. Increased operational agility will enable rapid decisions and opportunistic science measurements not possible in previous missions to small bodies.

To assist NASA in accomplishing future small body navigation goals, several important advances are made. First, the effectiveness of modern orbit estimation techniques is investigated, with the higher order Additive Divided-Difference sigma point Filter (ADF) implemented and used along with the

standard Extended Kalman Filter (EKF) to estimate the spacecraft state from optical small body surface landmark measurements. The ADF performs consistently better than the EKF in the simulations performed, with increasing improvement for higher levels of initial state error and longer intervals between photos of the surface.

Second, a new method is created to improve onboard navigation filter performance in diverse and rapidly changing dynamical environments. The approach is to precompute a process noise profile along a reference trajectory using consider covariance analysis tools and filters. When used in an onboard navigation filter, the precomputed process noise allows the filter to account for time- and state-dependent perturbations in the dynamics. The new method also obviates the need for most or all traditional manual tuning of the filter, and provides significantly improved representation of the state uncertainty.

Finally, a Simultaneous Localization And Mapping (SLAM) algorithm is employed to estimate the spin state of a tumbling small body (which are expected to be a significant percentage of the small bodies in the solar system), as well as the spacecraft state and surface landmark locations. For the small body characterization phase of the Rosetta mission, the state estimates converge successfully for large initial state errors. The SLAM algorithm remains effective for a range of small body spin states and masses that correspond to expected tumbling small bodies throughout the solar system. The SLAM algorithm is successfully applied to high fidelity independently simulated imagery of a tumbling small body generated by the European Space Agency, and a method for initializing the small body landmark locations is provided.

Table of Contents

List of Tables

List of Figures

Chapter 1

Introduction

Navigation about small bodies such as asteroids and comets remains a challenging engineering problem. Similarities to the ubiquitous terrestrial navigation problem (e.g. autonomous robots, vehicles, and unmanned aerial vehicles) include the use of optical and range measurements, as well the need to identify and estimate the locations of landmarks used for navigation while also estimating the robotic vehicle state. The primary differences between the two problems are the magnitude of the distances to the landmarks, the dynamical environment, and the types of landmarks used (i.e. surface features on a small body versus hallway corners and traffic intersections). These differences drive the need for advances in navigation capabilities for spacecraft approaching, orbiting, and landing on small bodies. The 2015 NASA Technology Roadmap [28] describes the importance of further developing navigation technology for future spacecraft missions:

> Technology developments in Position, Navigation, and Timing (PNT) will benefit both human and robotic spaceflight. More precise positioning will facilitate higher quality data return from science instruments, such as high-resolution cameras, and will enable mission operations concepts, such as precise landing and deep space formation flying, that are not possible with today's navigation capability.

Spacecraft have been visiting small bodies since 1986, when the Giotto spacecraft flew by the Halley comet [39]. The first flyby of an asteroid took place when Galileo flew by 951 Gaspra on its way to Jupiter in October of 1991 [130]. Using optical navigation techniques previously pioneered for planetary exploration, the Galileo navigation team reduced the uncertainty of the Galileo position relative to Gaspra during the approach, enabling the spacecraft to obtain images much closer to the body than would have otherwise been possible given the 5 degree field-of-view onboard camera [129, 60].

Since those first missions, there have been a total eight flybys of asteroids and seven close flybys of comets. The use of optical navigation for small body flybys would eventually lead to software developed by the Jet Propulsion Laboratory (JPL) known as AutoNav, which has been employed for the Deep Space 1, Stardust, and Deep Impact missions (as well as the follow-on missions Stardust-NExT and EPOXI) [17]. The successful use of AutoNav for these flyby and impact missions at asteroids and comets has proven that autonomous navigation can be achieved for small body flybys.

While there have been fifteen flybys of small bodies, only five small bodies have been orbited by spacecraft: Eros, Itokawa, Vesta, Ceres (which may be more appropriately labeled a dwarf planet than a small body), and Comet 67P/Churyumov-Gerasimenko. The first spacecraft to orbit and land on a small body, NASA's NEAR-Shoemaker mission orbited the asteroid Eros from February 2000 to February 2001 before landing on the surface, used ground-in-the-loop navigation that employed standard DSN radiometric tracking as well as 47 manually identified crater landmarks on the surface. [137, 3]. The orbit

determination used data arcs of 5 and 30 days within a Batch Least Squares (BLS) formulation [121]. The NEAR Laser Ranging instrument was also employed as a secondary source for orbit determination, but it was primarily used for shape model generation of the body. The final landing of the spacecraft on the surface was performed open-loop, as the light-time delays would make ground-based navigation impossible.

The Hayabusa mission flown by the Japanese Space Agency (JAXA) arrived at the asteroid Itokawa in September 2005, and landed on the surface in November 2005 to collect samples that would eventually be returned to Earth in June 2010. Hayabusa employed two optical navigation cameras (narrow and wide angle), two laser ranging systems (for above and below 50 meters altitude), and an artificial landmark dropped to the surface from the spacecraft at 30 meters altitude. The measurements from these sensors were processed using an Extended Kalman Filter (EKF) [121] to perform ground-based orbit determination [68]. An experimental autonomous optical navigation (AON) capability for descent and landing on Itokawa was developed for Hayabusa [143, 69], but ground-in-the-loop navigation was used as the primary navigation method (with malfunctions in the experimental AON capability also limiting its accuracy) [51].

The Dawn mission orbited the asteroid Vesta from July 2011 to September 2012, and then made its way to its final home in orbit about Ceres, arriving in March 2015. At both bodies, radiometric tracking combined with optical navigation were used to performance orbit determination [80], with the measurements processed on the ground using BLS filtering. Optical landmarks

were constructed using the technique known as stereophotoclinometry (SPC), first introduced by Gaskell using optical data from the Eros mission [43].

The ESA mission Rosetta arrived at comet 67P/Churyumov-Gerasimenko in August 2014 and deployed the lander Philae in November 2014. The mission will end with a controlled descent to the comet surface on September 30, 2016. Navigation for the Rosetta is performed with a Square Root Information Filter [47], processing both radiometric tracking (2-way Doppler and range) and landmark observations from images of the surface taken by onboard cameras [86]. Initially a manual identification and selection process was used for the landmarks, employing a GUI to aid in the process. Eventually an automated process employing the SPC technique was employed, dramatically reducing the ground operations workload [96]. All navigation is performed on the ground. The limited accuracy of the ground-in-the-loop navigation also restricted the achievable landing accuracy of the lander Philae, hindering Rosetta mission planners when selecting a landing site (as no landing site on the Comet's surface was smooth and large enough to meet ideal landing conditions for a blind ballistic approach).

A common fact emerges from the four missions that have orbited a small body: all use ground-based orbit determination tools as the primary navigation method. This ground-based method limits navigation accuracy, and can require extensive ground resources. Autonomous navigation has the potential to provide significantly greater accuracy, as well as reduce required ground resources. Missions that require pinpoint landing on the order of less than one meter become possible [19], allowing science goals and possibly com-

mercial and planetary protection goals to be achieved. In particular, science goals of understanding the origins of the solar system are strongly assisted by accurate autonomous navigation, as it enables spacecraft to land at very specific locations a small body surface. Pinpoint landing is especially important because other means of positioning science instruments on the surface, such as rovers and walking by humans, are not practical in the ultra-low gravitational environment of most small bodies. Additionally the rugged surface of small bodies typically results in small and sparse safe landing spots, and the weak gravity field results in a very limited range of allowable landing speeds [110].

The benefits and types of missions enabled by accurate autonomous navigation for missions orbiting and landing on small bodies has motivated researchers and mission planners to pursue this technology [19, 63, 32], including working on enhancements to AutoNav to enable autonomous navigation for these missions [98]. The 2015 NASA Technology Roadmap [28] also emphasizes the importance of advances in autonomous navigation capabilities:

> As NASA's human exploration and science missions progress farther from Earth, the Agency must minimize and eventually overcome the impacts of latency on the navigation and maneuver planning or execution for varied space systems, such as spacecraft and planetary rovers. In the near-term, gradually increasing levels of autonomous navigation capabilities will **allow platforms to go longer between time and state vector updates from the Earth**. A significant benefit to be attained in this case will be a reduction in the burden of routine navigational support. ... An additional benefit that will accrue from having autonomous onboard

> navigation and maneuvering capabilities will be an increase in a platform's operational agility, enabling near-real-time re-planning and opportunistic science. In the longer term, fully autonomous navigational capabilities will **enable classes of missions that would otherwise not be possible due to round-trip light time constraints**.

Figure 1.1 illustrates how advances in various navigation technologies provide new near- and far-term capabilities for future NASA missions, including those to small bodies. A significant near- and far-term component of this development timeline is the further advancement of estimation filters used for spacecraft navigation. It is this need for development of estimation filters and greater autonomy for missions orbiting and landing on small bodies that provides the primary motivation and objective of the research described in this dissertation: to obtain innovative filtering solutions to the general problem of autonomous navigation for spacecraft missions orbiting and landing small bodies. There is a particular focus on challenges that small body missions such as the European Space Agency (ESA) Rosetta mission and NASA's OSIRIS-REx mission have faced or will face in the near future.

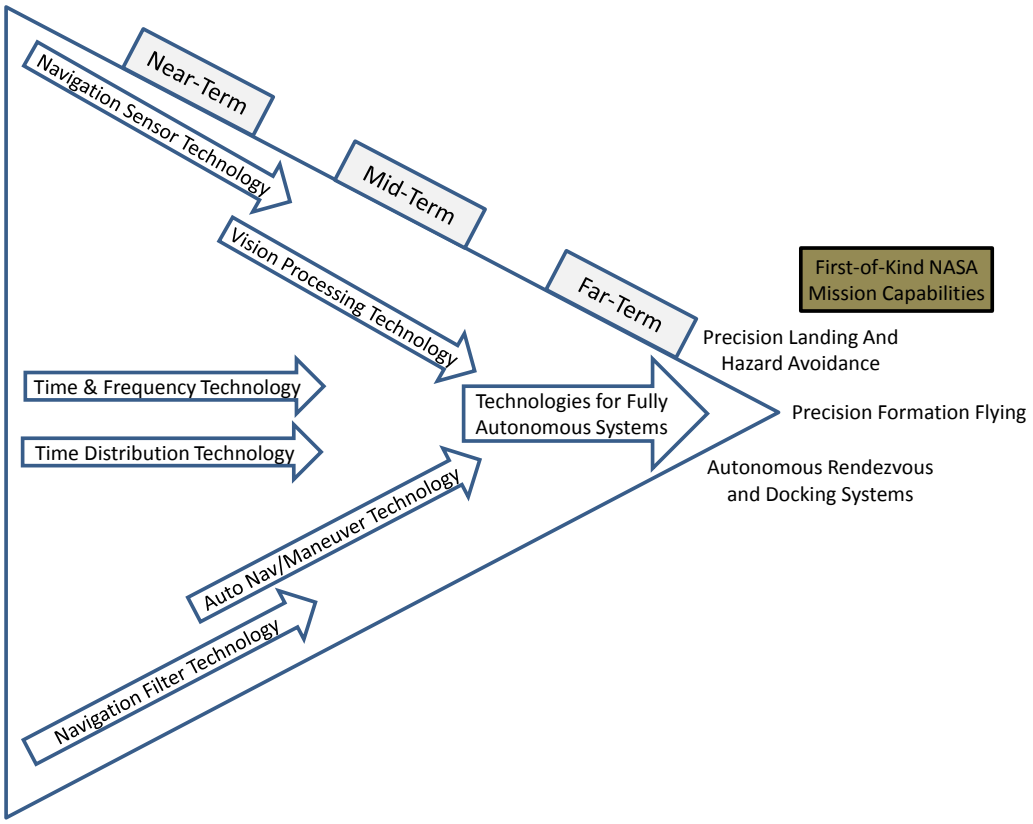

Figure 1.1: NASA Roadmap Position Navigation and Timing Development Timeline [28]

1.1 Optical Landmark Measurement Model

Many types of measurements can be used for navigation about small bodies, including radar, lidar, and optical measurements. Using cameras to produce optical measurements has strong advantages in terms of cost and ease of implementation. The optical measurements are the line-of-sight direction vectors from the spacecraft to landmarks on the surface of the small body. Surface landmarks can be identified in a variety of ways:

- Natural surface features such as craters and ridge-lines can be manually selected by the mission analyst or operator using a graphical user interface [44, 27], with the goal of consistently selecting features that are clearly identifiable on the surface in many different lighting conditions.

- Standard computer vision techniques such as SIFT or SURF [58] can be employed to identify consistent landmarks.

- The central points of "maplets" generated using the stereophotoclinometry (SPC) method (a correlation technique that uses detailed topographic and albedo maps of the surface) can serve as landmark observations [44, 81].

In the following chapters, the landmark body-fixed locations are either assumed known or are corrected by the estimation process. The term "body-fixed" refers to the frame fixed to and centered on the small body (not the spacecraft).

To compute the expected optical measurement for a particular landmark, first the vector from the spacecraft to the j^{th} landmark in the body-fixed frame is calculated as

$$\boldsymbol{O_j} = \boldsymbol{L_j} - \boldsymbol{r_{sc}^{bf}} \tag{1.1}$$

where $\boldsymbol{L_j}$ is the body-fixed landmark position, and $\boldsymbol{r_{sc}^{bf}}$ is the Cartesian spacecraft position in the body-fixed frame. This vector can be transformed to inertial coordinates using the rotation matrix $\boldsymbol{R_{bf2i}}$, which is computed using the small body orientation parameters at the picture time. The spacecraft-fixed frame is similarly defined by the rotation matrix $\boldsymbol{R_{i2sc}}$, and the camera

frame is defined relative to this spacecraft-fixed frame as $\boldsymbol{R_{sc2cam}}$ (with the camera boresight along the camera frame z-axis). Thus the complete rotation matrix that converts inertial vectors into the camera frame is

$$\boldsymbol{R_{i2cam}} = \boldsymbol{R_{sc2cam}}\boldsymbol{R_{i2sc}} \tag{1.2}$$

The vector from the spacecraft to the j^{th} landmark in camera coordinates is

$$\boldsymbol{O_{c_j}} = \boldsymbol{R_{i2cam}}\boldsymbol{R_{bf2i}}\boldsymbol{O_j} \tag{1.3}$$

which is transformed into the two-dimensional camera focal plane using the gnomonic projection (mapping points on a sphere onto a plane) [95]

$$\begin{bmatrix} x_j \\ y_j \end{bmatrix} = \frac{f}{O_{c_j}[3]} \begin{bmatrix} O_{c_j}[1] \\ O_{c_j}[2] \end{bmatrix} \tag{1.4}$$

where f is the camera focal length (typically in millimeters). These focal plane coordinates x_j and y_j are transformed into pixel and line values, i.e. the horizontal and vertical pixel location within the picture, with the equation

$$\begin{bmatrix} p_j \\ l_j \end{bmatrix} = \begin{bmatrix} K_x & K_{xy} & K_{xxy} \\ K_{yx} & K_y & K_{yxy} \end{bmatrix} \begin{bmatrix} x_j \\ y_j \\ x_j y_j \end{bmatrix} + \begin{bmatrix} p_0 \\ l_0 \end{bmatrix} \tag{1.5}$$

where the elements of the $\mathbf{K}$ matrix are the vertical and horizontal pixel densities of the sensor array (typically in pixels per millimeters), and are calibrated using star fields before arrival at the small body. The center pixel and line values are p_0 and l_0, respectively. Note that Eq. (1.5) can produce values in increments smaller than individual pixels, as modern image processing capabilities can generate landmark center values at sub-pixel precision. The process of using these landmark measurements to estimate the states of interest is described in detail in previous studies [19, 90].

1.2 Forces Acting On Spacecraft Near Small Bodies

It is important to understand the dynamical environment and forces that can affect the trajectory of a spacecraft in the vicinity of small bodies when designing navigation methods for missions to these small bodies. The dynamics of spacecraft orbital motion about small bodies such as asteroids, comets, and small planetary moons can be complex due to the variety of forces that act on spacecraft operating near these bodies. An exploration of these forces and the relative magnitudes for different scenarios is presented here, with a focus on those forces most relevant for orbital motion in navigation simulations (versus the design of the mission trajectory to and around the small body).

First each of the individual forces are described, from the dominant and relatively benign central body force to the more exotic and vastly more complex forces such as outgassing. Next the relative impact of these forces on spacecraft motion are described for different spacecraft locations relative to the small body, small body locations within the solar system, and small body sizes. Understanding the relative magnitude of these forces is important for navigation analyses, allowing the analyst to include only those forces relevant to a particular small body mission scenario. For more information on the forces that affect the dynamics of spacecraft about larger bodies such as dwarf planets Pluto and Ceres (and other spherical planets and moons), see Russell [104] and Scheeres [110].

1.2.1 Individual Forces on Spacecraft

The individual forces that can affect the trajectory of a spacecraft are described below. The models used for these forces are provided, allowing the analyst to incorporate the forces in simulations and estimation analysis.

1.2.1.1 Central Body Force

The central body gravitational force acting on the spacecraft is

$$\boldsymbol{F_{CB}} = -m\frac{GM}{r^3}\boldsymbol{r} \tag{1.6}$$

where m is the spacecraft mass, GM is the gravitational constant of the small body, $\boldsymbol{r}$ is the vector from the center of mass of the small body to the spacecraft center of mass, and r is the magnitude of the $\boldsymbol{r}$ vector. For small bodies, the GM is many orders of magnitude smaller than a typical planetary GM, and thus the central body gravitational force is many orders of magnitude smaller than for any planetary size body. The central body force can also be described as the gradient of the central body gravity potential function,

$$U_{CB} = \frac{GM}{r} \tag{1.7}$$

where $\boldsymbol{F_{CB}} = m\frac{\partial U_{CB}}{\partial \boldsymbol{r}}$.

For a given spacecraft mass, the central body force grows larger with increasing small body mass as a linear function. The central body force also increases with decreasing distance from the spacecraft center of mass to the central body center of mass according to the inverse square law. Thus, for a given percentage change in small body mass M and the distance r, the overall force will be more sensitive to changes in the distance r.

1.2.1.2 Gravity Perturbations from Non-Uniform Gravity Field

The term "gravity perturbations" refers to all non-central body gravity forces acting on a spacecraft. The potential function of these forces is described using spherical harmonic coefficients [121, 62] according to the equation

$$\begin{aligned} U_{\text{grav}} = & \frac{GM}{r}\left\{\sum_{l=1}^{N}\left(\frac{a_e}{r}\right)^l P_l(\sin\phi)C_{l,0} + \right. \\ & \left. \sum_{l=1}^{N}\sum_{m=1}^{l}\left(\frac{a_e}{r}\right)^l P_{lm}(\sin\phi)\left[C_{lm}\cos m\lambda + S_{lm}\sin m\lambda\right]\right\} \end{aligned} \tag{1.8}$$

where N is the maximum degree and order of the expansion, a_e is the reference distance (typically chosen as the average equatorial radius of the body, which may not be obvious for a small body), ϕ is the geocentric latitude of the spacecraft, and λ is the geocentric longitude of the spacecraft. P_l are Legendre polynomials [54] with degree l and argument $\sin\phi$, and P_{lm} are Legendre associated functions of degree l and order m, also with argument $\sin\phi$. The terms $C_{l,0}$, C_{lm}, and S_{lm} are the mass property coefficients that describe how the mass distribution of the body translates into the disturbance potential (and thus force).

Typically the normalized values for the Legendre polynomials P_l, Legendre associated functions P_{lm}, and the mass property coefficients C_{lm} and S_{lm} are used to avoid numerical issues. The values for the Legendre polynomials and associated functions grow and the mass property coefficients shrink for higher degree and order indices.

The force acting on the spacecraft is the gradient of this potential, multiplied by the spacecraft mass:

$$\boldsymbol{F}_{\text{GravPert}} = m\nabla U_{\text{grav}} \tag{1.9}$$

The total gravitational potential is a combination of the central body gravity potential and the above disturbing potential:

$$U(\boldsymbol{r}) = U_{CB}(\boldsymbol{r}) + U_{grav}(\boldsymbol{r}) \tag{1.10}$$

Because most small bodies have approximately uniform density (as compared to larger planetary bodies), the spherical harmonic coefficients that allow the computation of the gravity perturbations for a given spacecraft location and mass are primarily dictated by the shape and size of the small body. To obtain accurate estimates for these spherical harmonic coefficients, a spacecraft orbiting the body is needed. However, the coefficients are needed to understand the forces acting on the spacecraft in order to design satisfactory trajectories. As a result of this "chicken and egg" problem, a boot-strapping method of slowly approaching the small body in stages is used to estimate the spherical harmonics values, with the estimated values from one stage needed to design the trajectory for the following stage. Also required are extensive Monte Carlo analyses to determine the realistic limits of those coefficients prior to the spacecraft approach of the small body [83].

Spherical harmonics are only one way of representing the non-uniform gravitational field of a body however. A significant problem with the spherical harmonic representation is that if the perturbation field point is below the

Brillouin sphere radius, the series used to compute the perturbation diverge. The Brillouin sphere is defined as the sphere centered at the body center of mass with radius equal to the point on the body furthest from the center of mass (i.e. the smallest sphere that completely contains the body). As a result of this deficiency in the spherical harmonic approach, which is primarily an issue for spacecraft approaching the surface of non-spherical small bodies [72], the representation used most commonly when the spacecraft approaches and enters the Brillouin sphere is the polyhedron model [110, 134]. This method is a closed form solution that uses constant density polyhedrons to obtain the gravitational potential and acceleration on spacecraft via a surface integral of the plate model representing the small body surface. Other possible gravitational representations that also work below the Brillouin sphere include the interior gravity field, mass concentration methods, and various interpolation techniques [120, 105, 5, 37, 26].

However, the focus of the navigation analysis in this dissertation is for mission phases in which the spacecraft is outside the Brillouin sphere. The spacecraft is outside the Brillouin sphere the vast majority of recent and planned small body missions. Thus the spherical harmonic approach is sufficient for the current scope.

1.2.1.3 Solar Radiation Pressure (SRP)

The force due to pressure from the solar radiation striking the spacecraft is commonly computed for initial trajectory and navigation analysis using what

is known as the "cannonball model" [127]:

$$\boldsymbol{F_{SRP}} = -\frac{SF_{sc}}{c}\,\nu\,C_r\,A\,\hat{\boldsymbol{r}}_{\boldsymbol{sc2sun}} \tag{1.11}$$

where c is the speed of light, A is the cross-sectional area of the spacecraft exposed to sunlight, $\hat{r}_{sc2sun}$ is the unit vector from the spacecraft to the sun, ν is the eclipse factor, and C_r is the overall coefficient of reflectivity of the spacecraft area lit by the sun. C_r ranges from 0 (in which case the spacecraft would be perfectly transparent) to 2 (in which case the spacecraft would be a perfect mirror). However, the standard "cannonball model" typically restricts C_r between 1 and 2 [84, 107]. The eclipse factor ν ranges from 0 (in which case the spacecraft is in the umbra of the small body and receives no sunlight) to 1 (in which case the spacecraft is in full sunlight). SF_{sc} is the solar flux at the spacecraft's distance from the sun, as computed by

$$SF_{sc} = SF_{Earth} * \left(\frac{r_{SunEarth}}{r_{sc2sun}}\right)^2 \tag{1.12}$$

where SF_{Earth} is the solar flux at one Astronomical Unit away from the Sun, $r_{SunEarth}$ is the absolute distance from the Sun to the Earth, and r_{sc2sun} is the absolute distance from the spacecraft to the Sun.

More detailed models than the "cannonball model" exist, which take into account the spacecraft attitude and shape model. These higher fidelity models are used for analyses further along in the mission planning process [48]. Higher fidelity models can also include the solar radiation reflected off of the small body's surface that strikes the spacecraft. However, due to the very low albedo of most small bodies, this force is typically negligible.

For many types of missions to small bodies it is feasible to design trajectories around the small body that never eclipse, due to the low gravity of the small body. One example is the European Space Agency mission Rosetta that is visiting Comet 67P/Churyumov–Gerasimenko. Thus, the eclipse factor ν never deviates from one in these missions. For missions in which a solar eclipse is unavoidable, some analysis should be performed to determine the effect of the eclipse on the spacecraft trajectory [103].

1.2.1.4 Third Body Perturbations (TBP)

The perturbing force on the spacecraft due to celestial bodies other than the central small body is described via the equation

$$\boldsymbol{F_{TBP}} = m\, a_{SRP} = m\, G \sum_{\text{All TB}} M_{TB} \left(\frac{\boldsymbol{r_{sc2tb}}}{r^3_{sc2tb}} - \frac{\boldsymbol{r_{cb2tb}}}{r^3_{cb2tb}} \right) \tag{1.13}$$

where G is the universal gravitational constant, M_{TB} is the mass of the perturbing body, $\boldsymbol{r_{sc2tb}}$ is the inertial position vector from the spacecraft position to the perturbing body center of mass, $\boldsymbol{r_{cb2tb}}$ is the inertial position vector from the central body center of mass to the perturbing body center of mass, and r_{sc2tb} and r_{cb2tb} are the corresponding magnitudes of those vectors [127]. The first term in the parenthesis of equation 1.13 is named the "direct" term, as it is the direct gravitational acceleration on the spacecraft from the third body. The second term in parenthesis is labeled the "indirect" term, as it is the influence that the third body has on the spacecraft through the central body.

When considering the third body perturbation effects of the Sun or other large celestial bodies such as the planets, it makes sense to continue using a coordinate frame centered on the small body that the spacecraft is investigating. However, when looking at binary systems of small bodies, in which the secondary body is a substantial fraction of the primary small body, a coordinate frame based at the barycenter of the two small bodies may be the more appropriate choice for navigation analysis [122, 31].

1.2.1.5 Outgassing and Plumes

Comets present an additional challenge to spacecraft mission planners and operators: outgassing. The volatiles that exist on comets can explosively sublimate when the comet is close enough to the Sun, which can pose a significant hazard to spacecraft such as Rosetta that plan to investigate a comet as it passes through perihelion. The distribution of volatiles on the surface and below the surface is completely unknown to mission planners and operators, so this force is the least predictable of all disturbances that can affect the spacecraft.

Some general trends are known: comet outgassing becomes more active as it gets closer to the sun, and the portion of the comet surface in sunlight as it rotates is more active than the non-illuminated portion. A general model for the outgassing force [110, 24] is given by

$$\boldsymbol{F_{OG}} = Q_j V_{OG} A_{sc} h \left(\hat{e}_j \cdot \hat{r}_{sj}\right) \frac{\boldsymbol{r}}{r^3} \tag{1.14}$$

where Q_j is the ejecta mass flow rate at the spacecraft location, V_{OG} is the velocity of the outgassing particles at the small body surface, and A_{sc} is the surface area of the spacecraft exposed to these particles. $h\left(\hat{e}_j \cdot \hat{r}_{sj}\right)$ is a function that computes whether the spacecraft is in the cone of ejecta based on the inertial jet surface normal unit vector $\hat{e}_j$, the inertial unit vector from the jet location to the spacecraft location $\hat{r}_{sj}$, and the half angle of the outgassing jet cone δ_j, as described by the equation

$$h\left(\hat{e}_j \cdot \hat{r}_{sj}\right) = \begin{cases} 1 & \hat{e}_j \cdot \hat{r}_{sj} \geq \cos(\delta_j) \\ 0 & \hat{e}_j \cdot \hat{r}_{sj} < \cos(\delta_j) \end{cases} \tag{1.15}$$

The ejecta mass flow rate Q_j is computed using the equation

$$Q_j = Sf(\theta_s)g(d)Q_* \tag{1.16}$$

where S is the relative intensity of the comet surface at the jet site, $f(\theta_s)$ is the relative insolation of the jet site as a function of the angle between the jet surface normal and sun direction, $g(d)$ is the outgassing strength as a function of the distance from the sun to the comet, and Q_* is the mass ejection rate at the surface when the comet is at 1 AU. $f(\theta_s)$ is defined by the equation

$$f(\theta_s) = \max \begin{cases} 0 \\ 1 - \alpha(1 - \cos(\theta_s)) \end{cases} \tag{1.17}$$

where α is the controlling parameter for outgassing strength as a function of solar insolation, which varies from 0 to 1. $g(d)$ is the outgassing strength as a function of the distance from the sun to the comet d, as described by the emperically derived equation

$$g(d) = g_0 \left(\frac{d}{d_0}\right)^{-c_1} \left[1 + \left(\frac{d}{d_0}\right)^{c_2}\right]^{-c_3} \tag{1.18}$$

where $g_0 = 0.111262$, $d_0 = 2.808$, $c_1 = 2.15$, $c_2 = 5.093$, and $c_3 = 4.6142$. The units for the argument d are in AU.

Note that the outgassing force is treated as an inverse square law in equation 1.14, which is likely conservative because the force may drop off significantly faster. Also note that the model provided above is simplistic and not based on *in situ* measured comet models (which should change after the Rosetta team has had a chance to evaluate various models at Comet 67P/Churyumov–Gerasimenko). This model also assumes that the jets emanate radially outward from the surface and expand in a cone shape. Other assumptions are that the gas is traveling much faster than the spacecraft relative to the comet, the spacecraft is relatively close to the comet, and the location and unit vectors of the jets vary in time as the comet rotates.

Additional research was performed to advance the model of outgassing for Comet 67P/Churyumov–Gerasimenko in anticipation of Rosetta's arrival in the Fall of 2014 [87, 70, 126]. One interesting conclusion from that analysis is that in the maximum outgassing scenario, the pressure force exceeds the gravitational attraction of the nucleus on the spacecraft in the cometocentric direction of the Sun. Another interesting conclusion is that there may be significant non-radial pressure forces from the outgassing acing on the spacecraft. Thus, mission analysts were required to carefully study the outgassing effects before launching the lander to the surface.

1.2.1.6 Other Kinds of Forces

Other forces are known to exist at the surface of small bodies and may affect a spacecraft at the surface. Electromagnetic forces acting on dust particles, as well as the plume from the spacecraft thrusters during the landing, may cause dust particles to impact the spacecraft [75, 99, 50]. Also possible are impulsive forces propagated through the small body from the impact of other bodies striking the surface [123, 7]. The surface may also "shake" if the body is in non-uniform rotation, as the slopes and surface forces would be functions of time, and could lead to the surface relaxing as the small body finds it's way to a rotational equilibrium [110]. Finally, there may be an effect known as van der Waals cohesion between surface particles that affect the distribution and mechanics of those particles, which may affect the movement of the lander on the surface [111]. It is expected that these forces would likely be negligible compared to the other forces described above, with the exception perhaps of a celestial impact on the small body.

The non-gravitational force known as the Yarkovsky effect can alter the small body's orbit, but at time scales orders of magnitude longer than the timelines of spacecraft missions [110]. Similarly, the Yarkovsky-O'Keefe-Radzievskii-Paddack (YORP) effect modifies the small body's spin state over time scales much longer than of interest to spacecraft operators [110].

Another important force that can affect the motion of a spacecraft, and thus navigation analysis, is onboard propulsion. Spacecraft maneuvers are not considered part of the dynamical environment, but are critical to model: ma-

neuvers are typically a large source of execution and knowledge error that can significantly affect navigation capabilities. A wide range of execution and knowledge errors can occur with different propulsive methods, from conventional chemical engines that can modeled as impulsive changes in velocity to low thrust ion engines [100] with much higher specific impulse (ISP). Readers interested in the errors associated with maneuvers that can affect spacecraft navigation are referred to Olson [90] and Gates [45].

1.2.2 Relative Magnitudes of Forces on Spacecraft

The individual forces described thus far can vary greatly in absolute and relative magnitude for different spacecraft locations relative to the small body, small body locations in the solar system, and small body sizes and masses. Understanding the relative magnitudes of these forces is critical for navigation and trajectory design analysis and planning. To better understand the relative magnitudes of these forces, the system attributes that affect the strength of the forces are systematically varied. The effects of each primary perturbation for a range of different spacecraft and small body situations are shown. The spacecraft mass is assumed to be 1422 kg, the surface area (for both SRP and outgassing jet perturbations) is 6 square meters, and the SRP coefficient of reflectivity is 1.1.

The asteroid Eros is used in most variation scenarios, as all information needed for understanding the dynamical environment around Eros is publicly available [66, 85, 113]. This information includes a detailed shape model, gravity spherical harmonic coefficients, and the location within the solar system

via a .bsp file that provides the ephemeris.[1] The 4 by 4 gravity field coefficients are used to compute the gravity perturbation forces. The NEAR Shoemaker mission that visited Eros also serves as an ideal example of the challenges of visiting small bodies with spacecraft, as the very low gravity of Eros meant that the spacecraft could easily escape or crash into the surface of Eros with small changes in velocity [136]. Thus, it is critical to understand the forces that can affect the spacecraft motion. There are demanding navigation requirements on small body missions, as knowledge of the mass, gravity distribution, and spin state must be obtained and refined as the spacecraft approaches the body. Other missions that are excellent examples include the Hayabusa mission to Itokawa [106, 142], the Dawn mission to Vesta and then Ceres [6, 125, 64], and the Rosetta mission to Comet 67P/Churyumov–Gerasimenko [109].

There have also been investigations of the interactions between these forces, and how they affect the general solution for the averaged motion of spacecraft orbiting small bodies [109, 29]. In particular, the relationship between SRP and gravity field perturbations, as well as how they affect the orbit together, is presented in Scheeres [108].

1.2.2.1 Variations in Spacecraft Distance to Small Body

For a given small body size, shape, and location within the solar system, the spacecraft's location relative to the small body can heavily dictate which forces dominate the motion of the spacecraft. In Figure 1.2, the magnitudes of

[1] `http://naif.jpl.nasa.gov/pub/naif/pds/data/near-a-spice-6-v1.0/nearsp_1000/data/spk/eros80.bsp`

the SRP, TBP, central body gravitation, and gravity perturbation forces are plotted as a function of the spacecraft radial position from Eros. Of course the gravity perturbations will also vary heavily with different spacecraft longitudes and latitudes, but the plot gives an approximation of the relative magnitudes of the forces.

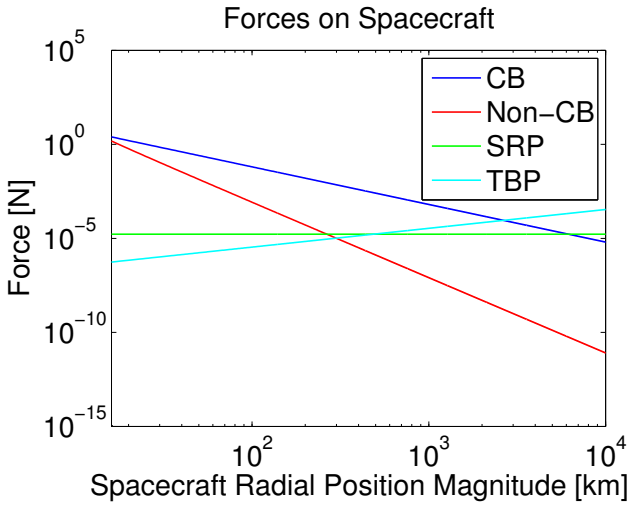

Figure 1.2: Forces on Spacecraft as Function of Spacecraft Radial Position Magnitude

For the Eros example, the central body and non-central body gravitational forces dominate the motion of the spacecraft when the spacecraft is close to the surface (assuming that the small body is not abnormally close to the sun or to another large celestial body). For reference, the dimensions of Eros are 34.4 by 11.2 by 11.2 km, and Eros is approximately 1.5 AU from the Sun (roughly the distance of Mars from the Sun). As the spacecraft moves away from the body, the non-central body gravitational forces drop off much faster than the central body term, as expected, and the SRP and TBP forces

overtake the non-central body gravity when the spacecraft is over 300 kilometers away from the body. At a radius of 300 kilometers, the non-central body, SRP, and TBP forces are all roughly the same order of magnitude. As a result, it is important to model all of these perturbations in orbits that spend significant time at 300 kilometers. If the spacecraft is consistently much closer to the small body, it may be acceptable to neglect SRP and TBP. The same is true of the gravity perturbations for orbital regimes significantly above 300 kilometers.

Note also that the TBP force starts much smaller than SRP, but grows to much larger values than SRP with increasing spacecraft distance from the small body. The increasing TBP magnitude is a consequence of the two vector terms in equation 1.13 growing apart. When the spacecraft is close to the small body the direct spacecraft-to-third-body and indirect small-body-to-third-body terms are very close in magnitude and direction. But as the spacecraft moves away from the small body the two vectors are increasingly different, and thus the overall perturbation grows. Additionally, the closer the spacecraft and small body are to the third body (e.g. planets like Jupiter), the more the TBP term will dominate.

As the radial position magnitude increases to thousands of times greater than the small body radii of Eros, eventually even the central body gravitational force is smaller than the TBP and SRP. For smaller bodies than Eros, the SRP becomes dominant at smaller radius values away from the small body, as is shown in the "Variations in Small Body Size and Mass" section.

Note that the bodies included in the computation of the TBP are Venus, Earth, Mars, Jupiter, Saturn, and the Sun (which is by far the largest perturbation). Venus is the largest perturbing force besides the sun at this example epoch due to it's proximity, and the perturbation due to Jupiter is only slightly smaller in magnitude than the Venus perturbation.

Russell [104] shows for a number of comet and asteroid bodies, the relative importance of the SRP and TBP at two different locations: the body radius and Hill radius. The Hill radius is one measure of the body's sphere of influence, and is analogous to the L_1 and L_2 libration point distance in the restricted third body problem [135]. The overall conclusion is that SRP is of much greater importance for small bodies orbiting the sun, and TBP are more important for small bodies orbiting planets, which matches the conclusions drawn from the plot shown above and the plot shown below in the section titled "Variations in Small Body Distance to Jupiter". Though most stable orbits about small bodies are generally no further than a third to a half the Hill radius [102], the perturbations are computed well outside of the Hill radius in this analysis in order to assess the their importance during the initial approach (and possibly subsequent departure) of the small body.

For small body flyby and impact/intercept missions, these same perturbations affect the spacecraft dynamics, but the time frame over which they act is much shorter. Thus, for most of these kinds of missions, only the central body gravity term of the small body is relevant (beyond the propulsive forces used to steer the spacecraft) [52].

1.2.2.2 Variations in Small Body Distance to Sun

For small bodies closer to the sun, the SRP and TBP from the sun increases significantly. As seen in equations 1.11 and 1.12, the force from the SRP increases as $(1/r^2)$ as the small body and spacecraft approach the sun. As seen in equation 1.13, the force from TBP increases even faster than $(1/r^2)$. To illustrate this concept, Figure 1.3 shows the forces on the spacecraft as the small body distance from the sun is varied from the Mercury orbit of 0.3 AU to 50 AU. The spacecraft is kept at a constant position relative to the small body, and thus the central body and non-central body gravity forces are constant.

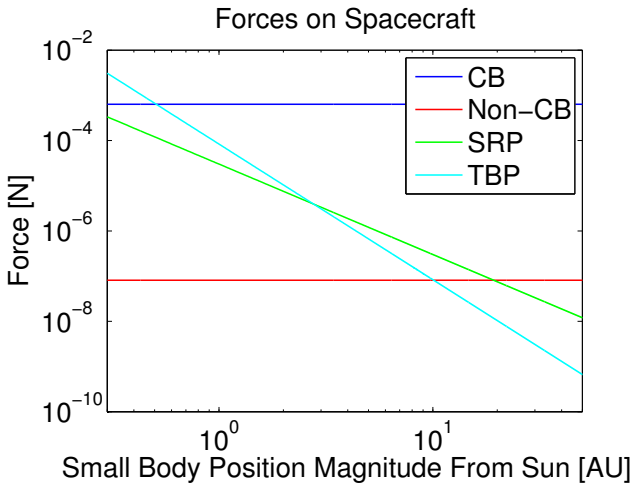

Figure 1.3: Forces on Spacecraft as Function of Small Body Distance to Sun

The magnitude of the spacecraft position relative to the small body is approximately 1000 kilometers. This very large distance is chosen so as to demonstrate a scenario for the Eros small body where the TBP can become larger than the central body force (in effect formation flying with the small body). When the spacecraft is closer to the small body, the central body terms

always dominates (at least for asteroid locations as close as 0.3 AU from the sun).

From Figure 1.3, it is clear that both SRP and TBP increase rapidly as the small body moves closer to the sun, and the TBP force increases faster than then SRP. Correspondingly the TBP also deceases faster than SRP with increasing distance from the Sun, and thus SRP is the dominant perturbation in this example from 2.5 to 20 AU.

1.2.2.3 Variations in Small Body Distance to Jupiter

For small bodies closer to one of the planets in the solar system, such as the minor moons of Jupiter, the third body perturbation from the planet can dominate the other forces acting on the spacecraft. Figure 1.4 illustrates this effect, with the distance from the Jupiter center of mass to the small body center of mass varied from 1.2 Jupiter Radii to 2000 Jupiter Radii. The spacecraft is kept at a constant position 100 km away from the small body.

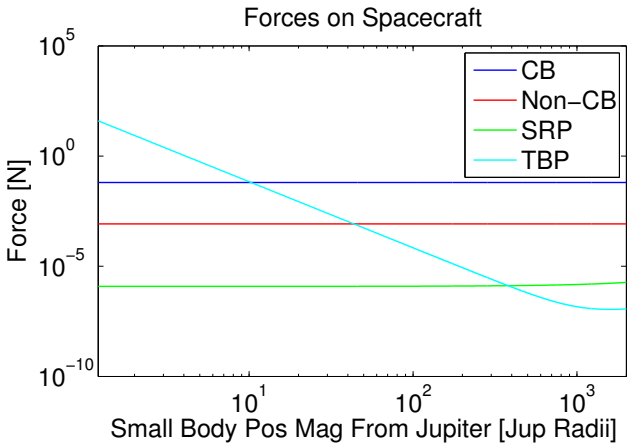

Figure 1.4: Forces on Spacecraft as Function of Small Body Distance to Jupiter

By far the most variable force in this example is the TBP. When the small body is less than 10 Jupiter Radii from the center of mass of Jupiter, the TBP force is larger than the central body force acting on the spacecraft from the small body. To put this distance into perspective, the moon Europa has a semi-major axis of 9.6 Jupiter Radii. Fortunately the vast majority of Jupiter moons that are considered "small bodies" are between 100 and 450 Jupiter Radii from Jupiter, but the TBP continues to be an important force to model even at these altitudes. At 1000 Jupiter Radii, the TBP plot levels out and starts to increase once again, as the perturbation from the Sun starts to become relevant. The SRP force increases very slightly with increasing distance from Jupiter only because the small body is moving in the direction of the sun with increasing distance from Jupiter in this example.

1.2.2.4 Variations in Small Body Size and Mass

The size and mass of the small body heavily influence the central body and gravitational perturbation forces on the spacecraft. For approximately constant density small bodies, the mass and size of the body are directly proportional, with larger and more massive bodies exerting stronger gravitational forces on a spacecraft than smaller and less massive bodies. The gravitational forces associated with a small body with the same proportions of Eros are computed as the average radius of the small body is varied from 100 meters to 300 kilometers, with the same density for all radius values (which is used to compute the mass of the body). The value of 300 kilometers is used as the upper bound to emulate Vesta, with radius values of 286.3 by 278.6 by 223.2

kilometers. The spacecraft is placed at a position 1.5 times the body radius for each value of the body radius shown in Figure 1.5.

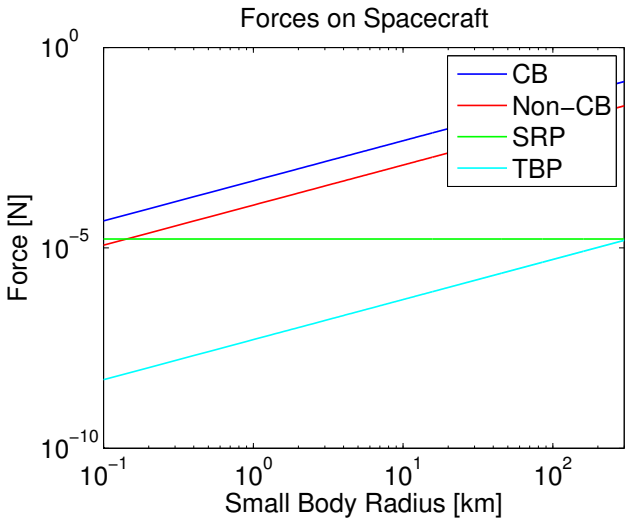

Figure 1.5: Forces on Spacecraft as Function of Small Body Radius

The central body, non-central body, and TBP forces increase exponentially with increasing radius. The SRP is relatively constant at these scales, and can be the dominate perturbation force when the small body has a radius below 200 meters. The SRP can also become smaller than the TBP as the body grows to sizes larger than 300 kilometers in radius, a consequence of the fact that the spacecraft is kept at 1.5 body radii away from the small body center of mass (a much larger distance for larger small bodies).

1.2.2.5 Relative Effect of Outgassing on Comets

For missions to comets, an additional perturbation must be considered: outgassing. Using the model defined above, the perturbation force of an outgassing jet placed at the largest radius of the small body is computed for a

range of spacecraft altitudes above the jet, as shown in Figure 1.6. The spacecraft's position is varied from the jet's exact location to approximately 1000 kilometers above the jet. The minimum and maximum expected surface ejecta speeds of 0.35 kilometers per second and 0.95 kilometers per second are used to compute the minimum and maximum force from the jet for the different spacecraft altitudes.

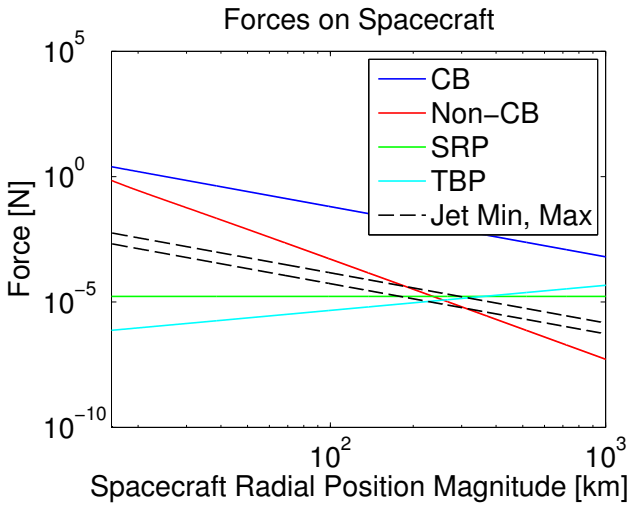

Figure 1.6: Forces on Spacecraft as Function of Spacecraft Distance Above Jet

The central body force remains the largest force for this example at all altitudes. Closer to the jet location on the surface, the non-central gravitational forces remain larger than the jet force, but other forces such as SRP and TBP are significantly smaller than the jet force.

A number of assumed parameters were used for these computed jet perturbations, from the jet speed at the surface (0.35 to 0.95 km/s) to the relative intensity value of the comet at the jet site α used in equation 1.17 (set to 0.5 for this example). Thus, the jet perturbation could be much smaller

or larger, but this example shows how it varies with spacecraft distance from the jet. This example also shows how it is possible to have orbit regimes with all four primary perturbation forces at the same order of magnitude. Between 200 and 300 km the four different perturbation forces are roughly equivalent in magnitude.

1.2.3 Small Body Dynamical Environment Conclusions

A variety of forces of very different natures can affect the motion and thus navigation of spacecraft in the region of small bodies. These forces depend on a number of factors, including the spacecraft's distance to the small body, the small body's distance to the sun or planetary body, the small body's size and mass, as well as the spacecraft's proximity to outgassing jets on comets. Because of the number of variables involved, it is wise to investigate all potential relevant perturbations that can affect the spacecraft for all orbital regimes a spacecraft mission can assume. This investigation must be done before any forces are neglected for computational savings in trajectory design or navigation analysis. In general however, forces such as solar radiation pressure play a much larger role in missions to small bodies than in missions orbiting larger celestial bodies such as planets, dwarf planets, and large moons.

1.3 Dissertation Outline and Contributions

Several advances in the field of small body navigation are described in this dissertation. Each of the main research topics is listed here and addressed fully in the following chapters. Appendix B lists the accepted and submitted

journal papers (in addition to conference papers) that are associated with each of these analyses.

Chapter 2 provides an investigation of the effectiveness of modern orbit estimation techniques for small body optical navigation. Two sequential estimation methods, the Extended Kalman Filter (EKF) and the Additive Divided-Difference sigma point Filter (ADF) are implemented and compared in a small body optical navigation scenario. Significant contributions from this work include:

- An analysis that reveals the initial spacecraft state error and time between measurements are the key drivers that distinguish the performance of the EKF versus the ADF. A trade study over different initial spacecraft state error levels and measurement time intervals shows where the ADF provides superior performance to the EKF, as well as the level of improvement in navigation robustness and error reduction obtained.

- An analysis showing that the measurement update step of the ADF provides almost all improvement in the ADF filter over the EKF, as well as an investigation of how long the interval between measurements must be before the ADF propagation method provides superior results over the traditional numerical integration of the state and covariance.

Chapter 3 introduces a novel method using well-established consider filters such as the Schmidt-Kalman filter to compute a process noise profile that can be uploaded and used in an onboard spacecraft navigation filter. The

process noise profile corresponds to a particular reference trajectory, and can be used by an onboard navigation algorithm such as an EKF. It is expected that the process noise profiles generated using the consider covariance analysis will prove particularly useful for missions in which autonomous operations must occur over short time intervals and in regions where perturbing forces change significantly over those intervals. One example is a descent trajectory to the surface of a small body that is far from Earth. Additional contributions from this research include:

- A method to compute process noise that requires no manual tuning, or greatly reduces the tuning needed (in cases where small amounts of traditional process noise must also be added)
- A demonstration of how appropriate levels of process noise are computed for all portions of reference trajectory (accounting for time- and state-dependent perturbations), providing navigation error and covariance consistency performance on par with the more computationally expensive consider filter. Linear and non-linear examples are used for this demonstration, with the non-linear descent scenario of NASA's OSIRIS-Rex mission used to show the superiority of the new process method over the traditional tuned process noise model.

The process of estimating a small body spin state and the landmark surface locations is one of the most challenging aspects of optical navigation around small bodies, and currently requires extensive mapping campaigns in order to get closer to and land on the body via a lengthy iterative process.

This "boot-strapping" process of first mapping, and then using those maps to navigate closer and make more detailed maps, has proven critical from previous missions to small bodies Eros, Itokawa, Vesta, Ceres, and Comet 67P/Churyumov-Gerasimenko. The upcoming NASA mission OSIRIS-REx will spend over 8 months mapping the surface before landing on the body [16].

Chapters 4 and 5 explore the use of Simultaneous Localization and Mapping (SLAM) techniques [49, 124, 131] for the initial spin state estimation of previously unvisited small bodies when first arriving at the small body, particularly for scenarios in which the small body is tumbling (i.e in significantly non-principal axes rotation). Initializing the spin state estimate of a tumbling small body is significantly more challenging, and most navigation tools are not designed to handle such a scenario. In addition to better handling the spin state estimation of a tumbling body, SLAM may enable spacecraft to approach the small body surface much faster, which can reduce risk in scenarios where poorly understood and unpredictable forces such as comet outgassing can occur (e.g. the Rosetta mission at Comet 67P/Churyumov-Gerasimenko [59]). SLAM may also allow significantly less ground operations and processing.

In Chapter 4, the SLAM tools are implemented and the Rosetta comet characterization phase is simulated to perform various trade studies and explore the limits of the SLAM algorithm capabilities. Contributions from Chapter 4 include:

- A analysis of the SLAM algorithm performance for different levels of body tumbling (and in particular the range of tumbling expected in

small bodies throughout the solar system), revealing that the SLAM algorithm can still converge on the correct spin state with large levels of initial angular velocity error (i.e. effectively no prior knowledge of the angular velocity). Similar analysis is performed showing the effective estimation of the spin state parameters and the landmark positions well beyond the largest expected initial landmark position errors, as well as for larger optical landmark measurement errors.

- Extensive observability analyses, with the Stripped Observability Matrix and the Singular Value Decomposition used to determine the states associated with each eigenvalue (providing a measure of the relative observability of the different states). Additional observability analysis considers how a shift in the landmark positions on the surface can be separated from an equal and opposite shift in the rotation of the body, with the conclusion that some level of non-sphericity and tumbling is necessary to fully separate these errors.

In Chapter 5, the developed SLAM tools are employed to estimate the spin state of an independently simulated small body created by ESA. High fidelity imagery of the tumbling small body is provided, from which landmarks are identified and the spin state is successfully estimated. Additional contributions from Chapter 5 include:

- A new method for obtaining initial small body landmark locations, using the first observations of those landmarks and a triaxial ellipsoid approx-

imately aligned with the minimum, medium, and maximum radii of the body

- A filtering and smoothing iteration scheme that provides smoothed state estimates of the spacecraft position and velocity; small body orientation and angular velocity (i.e. it's spin state); small body inertia tensor; landmark body-fixed surface positions; and via an indirect method the impulsive maneuver delta-v vectors

Chapter 6 provides a summary of the research objectives and accomplishments, as well as potentially valuable future research ideas. Applications of the research to future missions to small bodies, as well other types of spacecraft missions and other fields that involve navigation, are emphasized.

Appendix A explains how to represent an attitude using Modified Rodrigues Parameters (MRP), and provides the dynamical model for this representation. The shadow set switching method for easily avoiding singularities is also provided, as well as the advantages of using MRP to represent the small body orientation in a small body spin state estimation scenario.

Chapter 2

Small Body Optical Navigation Using The Additive Divided Difference Sigma Point Filter

In this chapter[1], sequential estimation methods are evaluated for small body autonomous navigation using optical landmark measurements. Sequential techniques are employed due to the inherently sequential nature of real-time navigation and the limited computational resources of onboard processors. All spacecraft state parameters (position, velocity, and attitude) are directly estimated from the optical landmark measurements to minimize measurement information loss. The standard Extended Kalman Filter (EKF) and the Additive Divided-difference sigma point Filter (ADF) are compared using Monte Carlo analyses in various mission scenarios. The ADF performs favorably versus the EKF, especially for greater initial state errors and longer intervals between measurements. Planners and operators for current and future missions that plan to use landmark optical navigation about small bodies

[1]The work in this chapter has been published as a journal paper:

- Olson, C., Russell, R., Carpenter, J.R., "Small Body Optical Navigation Using The Additive Divided Difference Sigma Point Filter," AIAA Journal of Guidance, Control and Dynamics, Vol. 39, No. 4, April 2016, pp. 922-928.

The analysis was performed primarily by the first author, with general development guidance and management provided by the co-authors.

could benefit from the sequential single-filter architecture and the tuning parameters used in this analysis.

2.1 Introduction

In previous studies performed by Bhaskaran, et al. [19] and the author [90], a two-level nested Batch Least Squares (BLS) approach was used to evaluate the feasibility of autonomous optical navigation about small bodies. However, this nesting approach can result in measurement information loss, and the limited computational resources of onboard processors lend better to sequential methods. Therein lies the main motivation and objectives of this chapter: Extend the results of previous studies to evaluate sequential estimation techniques in a single filter architecture, and compare the EKF to the higher order Additive Divided difference sigma point Filter (ADF) [74].

Other researchers have investigated sigma point filters such as the Unscented Kalman Filter (UKF) for planetary Entry, Descent and Landing, [42], but not for optical navigation around small bodies. The Rao-Blackwellized Particle Filter has been considered for small body landings with optical navigation [35, 36], but sigma point filters are more likely to be feasible with onboard computation constraints.

Both the EKF and ADF are employed to estimate the inertial position, velocity, and attitude of the spacecraft directly from the surface landmark optical measurements, using the attitude from an independent attitude determination system consisting of gyroscopes, star cameras, and an attitude deter-

mination filter as the a priori state. Modified Rodrigues Parameters (MRP) [38] are used to represent the spacecraft's attitude (see Appendix A). Monte Carlo analyses are employed to statistically evaluate each filter's performance, assess covariance realism, and compare the different techniques.

The ADF is chosen for evaluation over other modern sigma point filters such as the Unscented Kalman Filter (UKF) because it requires only one additional tuning parameter, versus three for the standard UKF formulation. The ADF is also in a square root form by default, enhancing numerical stability and ensuring the positive definiteness of the covariance matrix [74] (though the UKF can also be implemented in square root form [128]).

2.2 Optical Navigation Using Landmarks

2.2.1 Landmark Measurements

The navigation algorithms detailed in this chapter use optical landmark measurements, with an observation model as described in section 1.1. The simulated camera is comparable to the Charge-Coupled Device (CCD) cameras used for navigation in previous small body missions. Specifically, the Rosetta mission navigation camera parameters are used, with a focal length of 140 mm, a sensor array of 1024 by 1024 pixels, and a total field-of-view (FOV) of approximately 5 degrees [67]. The results of this chapter are generally applicable to any CCD with a similar focal length, pixel array size, and FOV (which includes all recent small body missions).

The landmark measurement error used in the simulations is based on measurement errors expected from the surface maplet stereophotoclinometry method, as described in Gaskell [44], which have numerous advantages over the use of natural surface features such as craters. It is assumed that the small body orientation, rotational velocity, shape model, gravity field, and a set of surface landmarks has been previously determined. The estimation of these items, along with landmark identification, are challenging topics of their own [114, 33, 95], and are considered in Chapters 4 and 5. A triaxial ellipsoid is used instead of a polyhedron shape model, which is sufficient for the evaluation of the navigation algorithms. Night shading has been implemented in the analysis, which greatly reduces the number of visible landmarks when the spacecraft is on the far side of the small body from the sun. Camera distortion effects on the images that are typically calibrated in flight are not included in the simulations.

2.2.2 Estimation Filter Architecture

It is well known that estimation processes benefit from using measurements in their most raw state possible (e.g. smoothing of measurements can lead to information loss). Thus, if possible, the raw landmark measurements are preferred, as in a tightly coupled inertial navigation system that uses GPS pseudorange measurements rather than GPS position fixes [132]. In this chapter, the spacecraft position, velocity, and attitude corrections are simultaneously estimated directly from the landmark observations, with an initially estimated attitude and covariance provided by an independent onboard attitude

determination system used as the apriori attitude state and covariance. It is assumed that the spacecraft is commanded to point the navigation camera at the center of mass of the small body using onboard position and attitude knowledge at every picture time using control moment gyroscopes (CMG), reaction wheels, or thrusters. Assuming that the attitude control error is low enough that a sufficient number of landmarks are in the camera field of view, the more important aspect for navigation analysis is the attitude knowledge error. The initial attitude knowledge error is simulated using expected attitude knowledge accuracy from modern onboard attitude determination systems [71, 76, 1].

While some filter nesting still occurs by using the independently estimated attitude from an onboard attitude determination system, the overall structure now consists of two filters rather than three. And by using the estimated attitude from the onboard attitude determination system in the form of an expected error on the truth attitude, given historical performance from previous missions, there is no need to dynamically propagate the spacecraft attitude between picture times. This approach also obviates the need to directly compute and incorporate attitude maneuvers, which significantly simplifies the simulation and is based on previous published work [19]. High accuracy attitude determination system estimates are very likely to be available on any future missions to small bodies, and thus the errors associated with these estimates are representative of what can be expected in future missions to small bodies.

A standard discrete additive Extended Kalman Filter, as described by Tapley, et. al. [121], is employed. Representing the spacecraft attitude as an

MRP vector is ideal for combined spacecraft position, velocity, and attitude estimation, as described in Appendix A.

2.2.2.1 Additive Divided difference sigma point Filter (ADF)

The ADF is a sigma point filter that uses second-order numerical differencing equations to approximate nonlinear dynamical and measurement models [88, 89]. The formulation used in this chapter is a hybrid of the forms presented by Lee and Alfriend [74] and Carpenter et. al. [25], in discrete form.

The Divided Difference Sigma Point Transformation (DDT) is the heart of the ADF, and is what makes the ADF unique from other sigma point filters. A brief description of the ADF starts with the DDT, used for both the nonlinear state propagation and measurement functions. In linearized filters it is common to approximate a nonlinear function $f(x)$ with a Taylor series truncation, such as

$$f(x) \approx f(\hat{x}) + f'(x)(x - \hat{x}) \tag{2.1}$$

where $f'(x)$ is an exact gradient. By contrast, the divided difference transformation uses a second-order truncation along with numerical differencing formulas for the derivatives:

$$f(x) \approx f(\hat{x}) + \tilde{D}^{(1)}_{\Delta x} f(\hat{x}) + \tilde{D}^{(2)}_{\Delta x} f(\hat{x}) \tag{2.2}$$

where the divided difference operators $\tilde{D}^{(i)}_{\Delta x} f(\hat{x})$ approximate the coefficients of the multidimensional Taylor series expansion using Stirling interpolations

[89, 88]. These interpolators difference perturbations of $f(\hat{x})$ across an interval, h, over a spanning basis set of sigma points, which are formed (i.e. spawned) from the columns of the Cholesky decomposition of the covariance of the domain vector, x. The sigma points are computed using the mean $\hat{x}$ and its corresponding covariance, P_x, as

$$\begin{aligned}\mathcal{X} = [\hat{x},\ \hat{x} + h\sqrt[c]{P}_x(:,1),\ \hat{x} + h\sqrt[c]{P}_x(:,2), ..., \\ \hat{x} - h\sqrt[c]{P}_x(:,1), \hat{x} - h\sqrt[c]{P}_x(:,2), ...\Big]\end{aligned} \tag{2.3}$$

where the subscript $(:,i)$ denotes column i of the corresponding array, and $P = \sqrt[c]{P}\sqrt[c]{P}^T$ denotes a Cholesky factorization. Let sigma points in the range of the function be given by

$$\mathcal{Y} = f(\mathcal{X}) \tag{2.4}$$

These range sigma points may be merged to form the mean of the range of the function using

$$\hat{y} = \mu_h(\mathcal{Y}) = \frac{h^2 - n}{h^2}\mathcal{Y}_{(:,1)} + \frac{1}{2h^2}\sum_{i=2}^{2n+1}\mathcal{Y}_{(:,i)} \tag{2.5}$$

To form an associated covariance, the following divided-differences are next computed:

$$\begin{aligned}\tilde{D}^{(1)}_{\Delta x} f(\hat{x})_{(:,i)} &= \frac{1}{2h}\Big[\mathcal{Y}_{(:,i+1)} - \mathcal{Y}_{(:,i+1+n)}\Big] \\ \tilde{D}^{(2)}_{\Delta x} f(\hat{x})_{(:,i)} &= \frac{\sqrt{h^2-1}}{2h^2}\Big[\mathcal{Y}_{(:,i+1)} + \mathcal{Y}_{(:,i+1+n)} - 2\mathcal{Y}_{(:,1)}\Big]\end{aligned} \tag{2.6}$$

The covariance is then computed from

$$P_y = \Big[\tilde{D}^{(1)}_{\Delta x} f(\hat{x}),\ \tilde{D}^{(2)}_{\Delta x} f(\hat{x})\Big]\Big[\tilde{D}^{(1)}_{\Delta x} f(\hat{x}),\ \tilde{D}^{(2)}_{\Delta x} f(\hat{x})\Big]^T \tag{2.7}$$

The DDT is applied to the nonlinear dynamics function to compute the propagated mean state and covariance, as well as to the nonlinear measurement function to compute the expected measurement and associated innovation covariance matrix. We employ the standard approach of using augmented state and covariance matrices for these transformations to incorporate traditional process and measurement noise [93, 74]. For the state and covariance propagation, the spawned sigma points are

$$\begin{aligned}
\mathcal{X}_{1,k}^{xw} &= \boldsymbol{X}_k^{xw} = \begin{bmatrix} \boldsymbol{X}_k^+ \\ \bar{\boldsymbol{w}}_k \end{bmatrix} = \begin{bmatrix} \boldsymbol{X}_k^+ \\ 0_{n_w \times 1} \end{bmatrix}_{n_{xw} \times 1} \\
\mathcal{X}_{i,k}^{xw} &= \boldsymbol{X}_k^{xw} + h \begin{bmatrix} \sqrt[C]{P_k^+} & 0 \\ 0 & \sqrt[C]{Q_k} \end{bmatrix}_{(:,i-1)}, \quad i = 2, ..., n_{xw} + 1 \\
\mathcal{X}_{i,k}^{xw} &= \boldsymbol{X}_k^{xw} - h \begin{bmatrix} \sqrt[C]{P_k^+} & 0 \\ 0 & \sqrt[C]{Q_k} \end{bmatrix}_{(:,i-1-n_{xw})}, \quad i = n_{xw} + 2, ..., 2n_{xw} + 1
\end{aligned} \tag{2.8}$$

where $\boldsymbol{X}_k^+$ is the post-fit state estimate at the previous time t_k, $\bar{\boldsymbol{w}}_k$ is the mean process noise, $\sqrt[C]{P_k^+}$ is the Cholesky decomposition of the post-fit state covariance at the previous time, $\sqrt[C]{Q_k}$ is the Cholesky decomposition of the process noise matrix, n_{xw} is the length of the augmented state vector for the state and covariance propagation, and h is the ADF tuning parameter. These sigma points are propagated using the state propagation function, with the process noise added:

$$\mathcal{X}_{i,k+1|k}^{x} = \boldsymbol{f}(\mathcal{X}_{i,k}(1 : n_x)) + \mathcal{X}_{i,k}(n_x + 1 : n_{xw}) \tag{2.9}$$

where n_x is the length of the non-augmented state vector, and the predicted state vector is computed using these propagated sigma points:

$$\boldsymbol{X}_{k+1}^- = \frac{h^2 - n_{xw}}{h^2} \mathcal{X}_{1,k+1|k}^x + \frac{1}{2h^2} \sum_{i=2}^{2n_{xw}+1} \mathcal{X}_{i,k+1|k}^x \tag{2.10}$$

The forward and central numerical difference terms are computed as

$$\begin{aligned}
\mathcal{S}^{(1)}_{x,k+1_{(:,i-1)}} &= \frac{1}{2h}\left[\mathcal{X}^{x}_{i,k+1|k} - \mathcal{X}^{x}_{i+n_{xw},k+1|k}\right], \quad i = 2, ..., n_{xw}+1 \\
\mathcal{S}^{(2)}_{x,k+1_{(:,i-1)}} &= \frac{\sqrt{h^2-1}}{2h^2}\left[\mathcal{X}^{x}_{i,k+1|k} + \mathcal{X}^{x}_{i+n_{xw},k+1|k} - 2\mathcal{X}^{x}_{1,k+1|k}\right], \quad i = 2, ..., n_{xw}+1
\end{aligned} \tag{2.11}$$

and the resulting mapped state covariance is

$$P^{-}_{k+1} = \begin{bmatrix}\mathcal{S}^{(1)}_{x,k+1} & \mathcal{S}^{(2)}_{x,k+1}\end{bmatrix}\begin{bmatrix}\mathcal{S}^{(1)}_{x,k+1} & \mathcal{S}^{(2)}_{x,k+1}\end{bmatrix}^{T} \tag{2.12}$$

The DDT is similarly applied to the nonlinear measurement function to produce the expected measurement $\bar{\boldsymbol{Y}}_{k+1}$ and the associated innovation covariance matrix P^{vv}_{k+1}, using the measurement uncertainty matrix R_{k+1} and assuming that the measurement noise is directly added to the output of the measurement function to obtain the output sigma points $\mathcal{Z}_{i,k+1}$. As part of this transformation, the forward and central difference terms are defined as

$$\begin{aligned}
\mathcal{S}^{(1)}_{v,k+1_{(:,i-1)}} &= \frac{1}{2h}\left[\mathcal{Z}_{i,k+1} - \mathcal{Z}_{i+n_{xv},k+1}\right], \qquad i = 2, ..., n_{xv}+1 \\
\mathcal{S}^{(2)}_{v,k+1_{(:,i-1)}} &= \frac{\sqrt{h^2-1}}{2h^2}\left[\mathcal{Z}_{i,k+1} + \mathcal{Z}_{i+n_{xv},k+1} - 2\mathcal{Z}_{1,k+1}\right], \qquad i = 2, ..., n_{xv}+1
\end{aligned} \tag{2.13}$$

where n_{xv} is the length of the augmented state vector for the measurement function transformation (i.e. the number of states plus the number of measurement values). Note that the tuning parameter h, typically set to the value of $\sqrt{3}$, can be different in the measurement function DDT than in the propagation function DDT.

The cross-correlation matrix is computed using the Cholesky decomposition of the mapped state covariance and the forward difference term from

the measurement function DDT:

$$P_{k+1}^{xy} = \sqrt[C]{P_{k+1}^{-}} \left[\mathcal{S}^{(1)}_{v,k+1_{(:,1:n_x)}} \right]^T \tag{2.14}$$

The filter gain matrix is generated using the same quantities as in the EKF (also provided in equation 3.16),

$$K_{k+1} = P_{k+1}^{xy} \left[P_{k+1}^{vv} \right]^{-1} \tag{2.15}$$

and the state vector estimate is computed using the residuals vector ν_{k+1} as in the EKF:

$$\boldsymbol{X}_{k+1}^{+} = \boldsymbol{X}_{k+1}^{-} + K_{k+1}\nu_{k+1} \tag{2.16}$$

The updated covariance can be computed via either the traditional formulation

$$P_{k+1}^{+} = P_{k+1}^{-} - K_{k+1}P_{k+1}^{vv}K_{k+1}^{T}, \tag{2.17}$$

or through the direct use of the difference values as

$$\begin{aligned} P_{k+1}^{+} = &\left[\sqrt[C]{P_{k+1}^{-}} - K_{k+1}\mathcal{S}_{k+1,x}^{vv} \quad K_{k+1}\mathcal{S}_{k+1,xv}^{vv} \right] \cdot \\ &\left[\sqrt[C]{P_{k+1}^{-}} - K_{k+1}\mathcal{S}_{k+1,x}^{vv} \quad K_{k+1}\mathcal{S}_{k+1,xv}^{vv} \right]^T \end{aligned} \tag{2.18}$$

where

$$\begin{aligned} \mathcal{S}_{k+1,x}^{vv} &= \mathcal{S}^{(1)}_{v,k+1_{(:,1:n_x)}} \\ \mathcal{S}_{k+1,xv}^{vv} &= \left[\mathcal{S}^{(1)}_{v,k+1_{(:,n_x+1)}}, ..., \mathcal{S}^{(1)}_{v,k+1_{(:,n_{xv})}}, \mathcal{S}^{(2)}_{v,k+1_{(:,1:n_{xv})}} \right] \end{aligned} \tag{2.19}$$

2.2.3 Dynamical Trajectory Model

The spacecraft position and velocity are propagated via numerical integration between picture times using variable step RK7(8) propagation, with

relative and absolute error tolerances set to 10^{-13}. The covariance is propagated to the same times, also using variable step propagation, by the standard method of integrating the state transition matrix via numerical integration. The simulation includes central body acceleration and perturbations from a spherical harmonic gravity field, for both the truth and filter dynamics. Standard perturbation accelerations from third body perturbations (TBP) and solar radiation pressure (SRP) are included for completeness in both the truth and filter dynamics, but these perturbations do not significantly affect the results and conclusions of the analysis (for the class of small bodies and orbits considered).

A 16 by 16 degree and order Eros spherical harmonic gravity model is used for the truth model, which is the highest degree and order field publicly available for Eros. The terms associated with the lower order 4 by 4 field are perturbed for each Monte Carlo trial using the uncertainties provided as part of the published Eros gravity field coefficients, and these values are used in the nominal model.

2.3 Simulation Scenario

Simulations are performed to assess the performance of the EKF and ADF filters. Various timing parameters of the simulations are listed in Table 2.1.

The mission scenario is a 50 kilometer radius orbit about a small body similar to the asteroid Eros, which is modeled as a triaxial ellipsoid with the

Table 2.1: Simulation Timing

Simulation Parameter	**Nominal Values**
Epoch Time	24-Nov-2017 09:55:00.00
End Time	28-Nov-2017 23:55:00.00
Minimum Time After Epoch Before First Update	1 hour
Minimum Time Before End Time For Last Update	0 hours
Time Between Measurements	3 hours

same major, intermediate, and minor axes dimensions as Eros. The initial position and velocity correspond to a circular orbit, which rapidly becomes non-circular due to gravity perturbations. See Tables 2.2 and 2.3 for the detailed parameters for Eros and the spacecraft, respectively.

There are 2000 predetermined and randomly located landmarks available for navigation, which are presumed to be a result of previous mapping campaigns. This number of landmarks is chosen in order to ensure that the spacecraft can observe a reasonable number of landmarks during the simulation, with a narrow field of view (5 degrees) limiting the amount of small body surface visible to the spacecraft. In past missions there have been on the order of thousands of landmarks available by this the time the spacecraft is orbiting this close to the small body [80]. Thus 2000 landmarks is a reasonable minimum number of available landmarks.

A non-terminator orbit is chosen to examine how the filters handle significant variation in the number of visible landmarks, and the orbit is low enough to possess significant non-linear motion due to the gravity terms of the body. The orbit is also chosen such that it remains outside the Brillouin

Table 2.2: Small Body Properties

Simulation Parameter	**Nominal Values**
Initial Pole Right Ascension, Declination	30, 40 deg
Pole Right Ascension, Declination Rates	2, 3 deg/Julian century
Longitude of the Prime Meridian at Epoch	50 deg
Rotation Rate	1639.389232 deg/day
GM	4.4627547×10^{-4} km^3/s^2
Radius Values	$17.2 \times 5.6 \times 5.6$ km
Number of Landmarks on surface	2000
Truth Gravity Harmonics	16 x 16 (Eros)
Nominal Gravity Harmonics	4 x 4 (Eros, Perturbed)

Table 2.3: Spacecraft Properties

Simulation Parameter	**Nominal Values**
Spacecraft Initial Position	[50, 0, 0] km
Spacecraft Initial Velocity	[0, 2.987559×10^{-3}, 0] km/s
Mass	1422 kg
Area	6 m^2

sphere of the body, so that spherical harmonics can be used for gravity perturbations. Figure 2.1 shows the truth inertial and body-fixed trajectories for this particular scenario.

2.3.1 Filter Parameters

The two filters use the same initial state uncertainty, but the value of the filter process noise is selected for each filter such that the resulting 3-sigma formal covariance is consistent with the error distribution of a Monte Carlo analysis for the nominal scenario described above. By choosing the process noise values differently for each filter based on this criteria, the optimum performance of each filter is compared. These parameters are listed in Table 2.4.

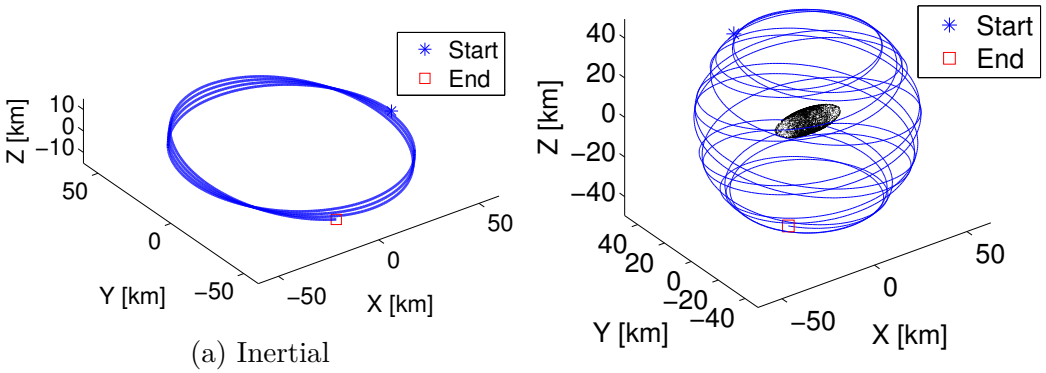

(a) Inertial

(b) Body-Fixed

Figure 2.1: Truth Trajectory

Note that the measurement noise covariance sigmas are higher in this nominal scenario than one might expect given the measurement error of 9 arc seconds (approximately equal to 0.5 pixel for the simulated camera) (1-sigma) shown in the next section. Setting these sigma values higher than the expected measurement error is known as measurement underweighting, which often produces the lowest navigation errors [145, 12]. Because the nominal attitude is obtained from a separate onboard attitude determination process at each photo time, and not dynamically propagated as explained previously, the a priori attitude covariance is the same for every photo. Thus no process noise is necessary for the attitude estimate. Note that nominally the spacecraft attitude is not estimated by setting the a priori attitude covariance to zero.

2.3.2 Monte Carlo Error Parameters

Monte Carlo simulations are used to obtain a realistic assessment of the filter predicted covariance. The 1-σ simulation error parameters sampled in the

Table 2.4: Filter Parameters

Simulation Parameter	**Nominal Values**
Initial Filter Position Covariance (1-σ)	[0.064, 0.048, 0.016] km
Initial Filter Velocity Covariance (1-σ)	[8x10^{-5}, 8x10^{-5}, 8x10^{-5}] km/s
Initial Filter Attitude Covariance (1-σ)	[0.0, 0.0, 0.0] deg
Measurement Noise Covariance (1-σ)	[44, 44] arcsec ([2.5, 2.5] pixels)
Process Noise q for Position and Velocity, EKF	1x10^{-13} km^2/s^3
Process Noise q for Position and Velocity, ADF	5x10^{-15} km^2/s^3
ADF Tuning Parameter, Propagation h^2	1.5
ADF Tuning Parameter, Update h^2	1.5

Monte Carlo simulations are listed in Table 2.5. Note that only the spacecraft parameters and the small body gravity field 4x4 coefficients are perturbed, with the small body parameters such as the pole direction and rotation rate kept fixed. The process noise included in the filters is used to account for these error sources and the growth in error during periods of no measurement that result from the error introduced previously. Modern image processing capabilities can generate landmark center values at sub-pixel precision, and thus 0.5 pixel errors (equivalent to 9 arc seconds angular error for this camera) are used in this simulation. The expected state errors from optical navigation in earlier mission phases are used for the initial state errors [1].

Because the intent of this chapter is to assess the relative performance of the EKF versus the ADF, the initial state errors are used to distribute the initial nominal states about the truth. Similarly, the nominal attitude at each picture time is computed by "adding" (in the rotational sense) the

Table 2.5: 1-σ Monte Carlo Error Parameters

Simulation Parameter	**1-σ Values**
Spacecraft Initial Position	[0.064, 0.048, 0.016] km
Spacecraft Initial Velocity	[8x10^{-5},8x10^{-5},8x10^{-5}] km/s
Attitude	[0.04, 0.04, 0.04] deg
Observation	[9, 9] arcsec ([0.5, 0.5] pixels)
Spacecraft Mass	20 kg
Spacecraft Area	1 m^2
Small Body 4x4 Gravity Coefficients	Published Eros Coefficient Uncertainties

computed attitude error to the truth pointing vector. As a result, there is a single truth trajectory and set of observations for all Monte Carlo trials. In an actual mission, only the estimated nominal state is known, and thus the initial state deviations based on the state uncertainty are used to distribute many different potential truth trajectories about the nominal reference trajectory. This approach is more appropriate when assessing the general performance of the filter, versus comparing the performance of the filters.

2.4 Simulation Results

In the nominal scenario, Monte Carlo analysis using 1000 trials is employed. The number of Monte Carlo trials was increased by an order of magnitude until the ensemble error statistics converged. Figure 2.2 shows the number of landmarks visible at each picture time for all Monte Carlo trials. The number of visible landmarks strongly correlates to the level of error observed in the simulations, as seen in Figure 2.3, which shows the error and covariance using the EKF and ADF. The attitude correction from the optical landmark

observations is very small, and does not significantly affect the performance of the filters. Attitude errors at least an order of magnitude larger than the conservative expected 0.04 degree (1-σ) error are necessary before the attitude correction significantly affects the estimation performance, which might occur if the independent attitude system estimates are degraded. Diverged runs, defined as those runs exceeding 0.5 kilometers of position error at the final simulation time, are not included in the plots. This divergence criteria is chosen based on the observed set of trial results of this particular problem. A more general divergence criteria is one that declares a trial diverged when the small body is no longer present in any subsequent images. The employment of this alternative divergence criteria is saved for future work. The RMS and Max statistics in the captions correspond to the shared non-diverged runs for both the EKF and ADF.

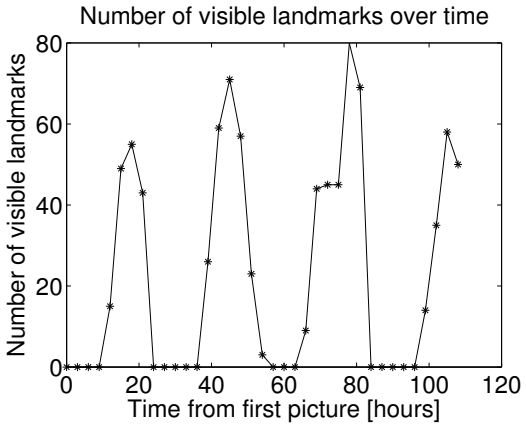

Figure 2.2: Landmark Visibility, 1000 Runs for the EKF, Nominal Scenario

While the EKF has 58 diverged trials over 1000 Monte Carlo runs, the ADF has zero, a significant improvement. These divergent runs are a

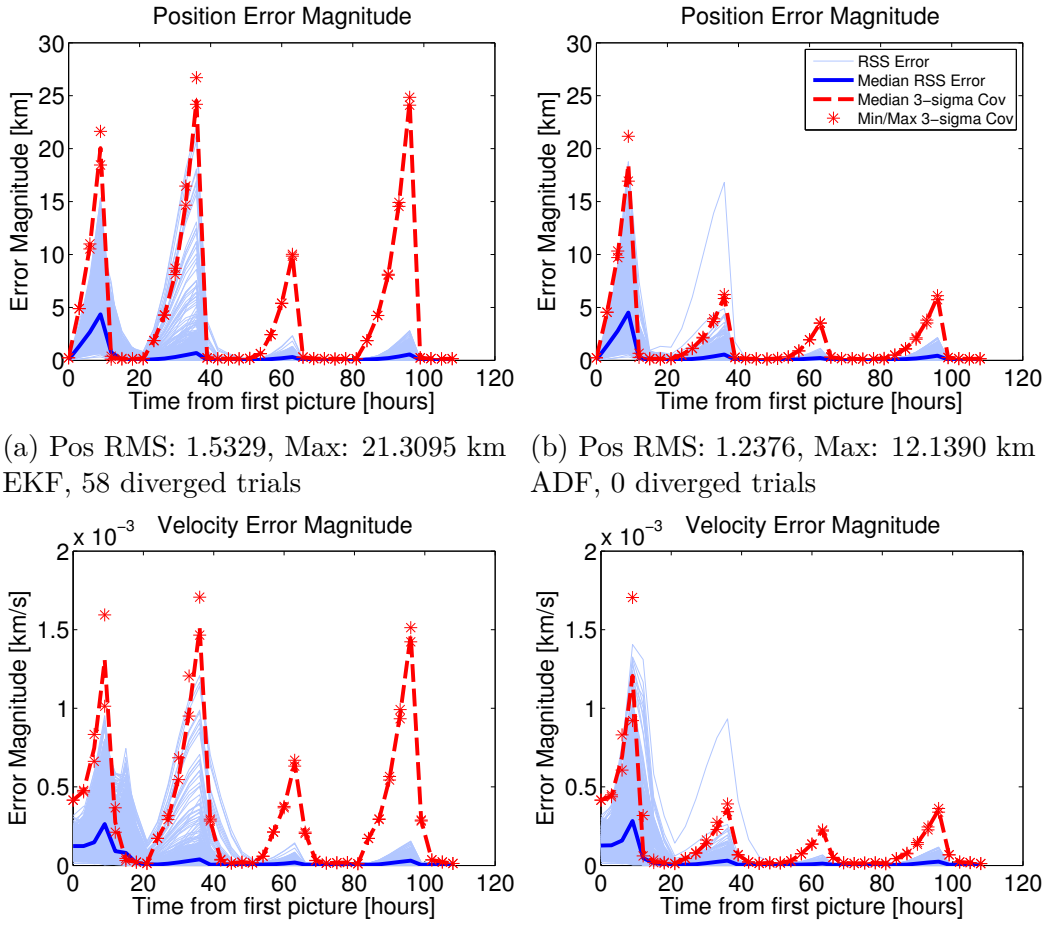

(a) Pos RMS: 1.5329, Max: 21.3095 km
EKF, 58 diverged trials

(b) Pos RMS: 1.2376, Max: 12.1390 km
ADF, 0 diverged trials

(c) Vel RMS: 1.137E-4, Max: 1.165E-3 km/s
EKF, 58 diverged trials

(d) Vel RMS: 8.874E-5, Max: 8.030E-4 km/s
ADF, 0 diverged trials

Figure 2.3: 1000 Monte Carlo Sim, RSS Error, 3x Root-Variance, Nominal Scenario

result of the EKF breaking down when landmark measurements are received following a time interval with no measurements (i.e. when the spacecraft is on the dark side of the body). Comparing the performance of the shared non-diverged trials in the ADF to the EKF, it is seen that the ADF better estimates the spacecraft position and velocity than the EKF, with error RMS

values approximately 19% (position) and 22% (velocity) lower than the EKF. The cyclic behavior of the performance is due to the periodic nature in the number of visible landmarks (see Figure 2.2), which in turn is a result of the lighting conditions on the small body. While the process noise values for the ADF and EKF are chosen to best represent the error distribution in the formal 3-sigma uncertainty, the ADF still outperforms the EKF when the process noise is set to the same value (for either process noise value).

The two parameters which most strongly affect the relative performance of the EKF versus the ADF are the initial state error and the time between observations. Thus, these two quantities are deterministically varied as described in Table 2.6 for the initial state error, and from 30 minutes to 5 hours (2% to 17% of the orbit period) for the observation interval, for a total of 100 nodes that are evaluated using Monte Carlo analysis of 100 nominal trials each. The number of trials is reduced from 1000 to 100, due to the large number of nodes evaluated. The results for each of the 100 resulting nodes are shown in Figure 2.4 below, where the EKF error RMS and number of diverged runs are subtracted from the ADF values (thus negative values show the ADF improvement).

The ADF has the same or fewer diverged trials than the EKF at every node, providing significant improvement in robustness over the EKF. A total of 224 fewer diverged trials take place over all 100 nodes. Among those shared non-diverged trials for each node, the position and velocity RMS values are consistently lower for the ADF than the EKF. Note that the performance difference between the ADF and EKF becomes greater with higher initial

Table 2.6: Trade Study Parameters

Simulation Parameter	**Values**
Initial Position Error (x)	[0.008 : 0.008 : 0.08] km 1-σ
Initial Position Error (y)	[0.006 : 0.006 : 0.06] km 1-σ
Initial Position Error (z)	[0.002 : 0.002 : 0.02] km 1-σ
Initial Velocity Error (all)	[1x10^{-5}:1x10^{-5}:1x10^{-4}] km/s 1-σ
Observation Interval	[0.5 : 0.5 : 5] hours

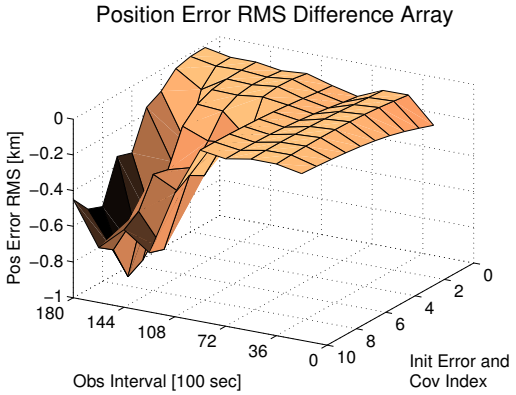

(a) Position Error RMS Differences

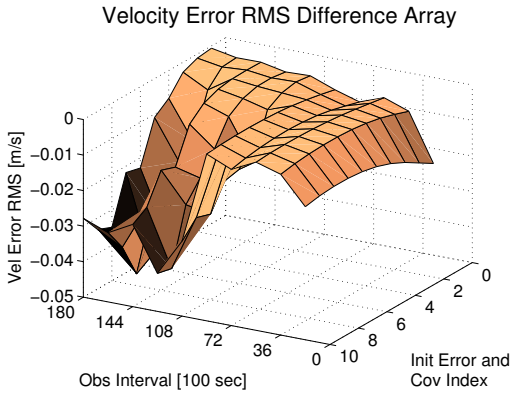

(b) Velocity Error RMS Differences

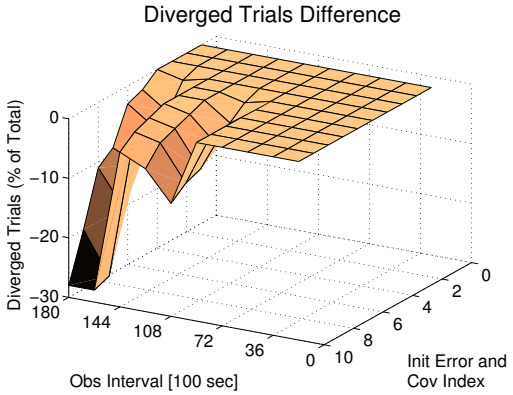

(c) Differences in Number of Diverged Trials

Figure 2.4: 100 Node Trade Study, 100 Nominal Monte Carlo Trials Each

state error and longer time intervals between photos. The nominal scenario with results given in Figure 2.3 corresponds to the Initial Error index 8 and observation interval of 10800 seconds node.

The improvements in performance seen in the scenarios when using the ADF are provided almost entirely by the measurement update portion of the filter. In other words, using the DDT for propagation of the spacecraft estimated state and covariance (versus the standard method of numerically propagating the previous post-fit state estimate) does not significantly affect the ADF filter performance for even the largest observation interval times considered above. To see significant enhancement in the results using the DDT for propagation of the state and covariance, the maximum initial error of the trade above is used and the observation interval is increased to ten hours (double the highest previous value, now at 34% of the orbit period). The ADF with and without the DDT for propagation are employed in 1000 trial Monte Carlo simulations, and the results are shown in Figure 2.5 below. The number of diverged trials is significantly lower with the full ADF employed: 53 instead of 110 out of 1000 trials, a 52% reduction. The RMS and max error statistics provided in the captions are for the shared non-diverged trials.

It is not the intent of this chapter to provide detailed timing comparisons between the methods, but some approximate timing values can give the reader a sense of the relative performance of each filter. All code is written in Fortran, using the latest 1995 and 2003 standards, and compiled using standard release mode settings in 2011 Intel Visual Fortran. All simulations are run on a single processor of a quad-core Intel Xeon CPU running at 3.60

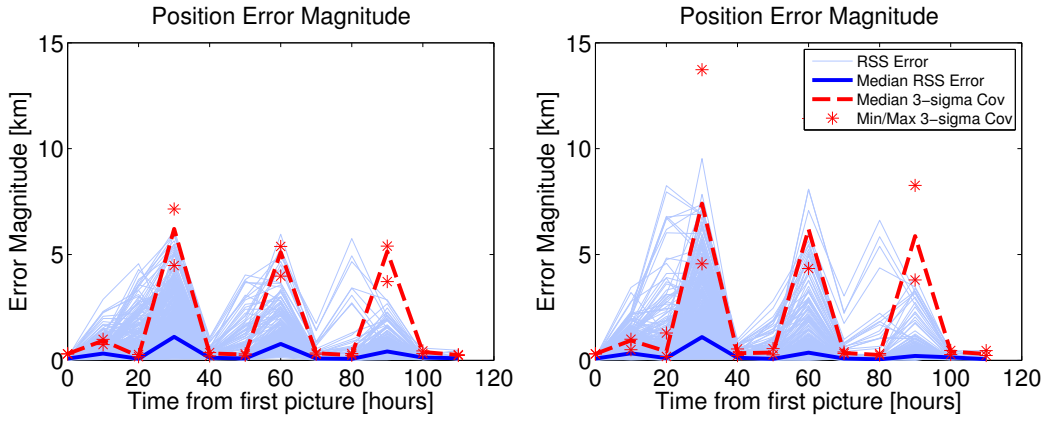

(a) Pos RMS: 0.8144, Max: 5.6474 km
ADF, Standard Prop, 110 diverged trials

(b) Pos RMS: 0.5931, Max: 7.8426 km
Full ADF, 53 diverged trials

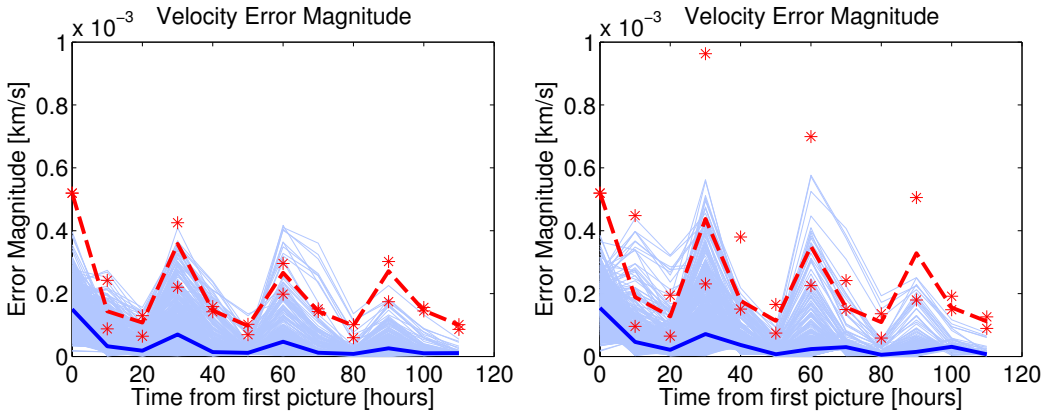

(c) Vel RMS: 7.583E-5, Max: 4.014E-4 km/s
ADF, Standard Prop, 110 diverged trials

(d) Vel RMS: 6.767E-5, Max: 5.577E-4 km/s
Full ADF, 53 diverged trials

Figure 2.5: 1000 Monte Carlo Sim, RSS Error, 3x Root-Variance, Longer Observation Intervals

GHz. For the full trade study with 100 nodes of 100 nominal Monte Carlo trials each, the EKF takes approximately 61 minutes to run. The ADF with standard propagation (only the measurement update uses the DDT) takes approximately 84 minutes, and the full ADF takes approximately 114 minutes. The ADF with standard propagation requires only 38% greater computational

effort than the EKF, while providing significant navigation improvement. The full ADF requires approximately 36% computational effort than the ADF with standard propagation, but improvements in performance are only seen for the largest observation intervals. Computational effort for all the filter options remains reasonable for onboard navigation.

From additional analysis, it is observed that EKF and ADF degrade at approximately the same rate when the measurement noise is increased, the measurement filter noise is reduced, the attitude error is increased, and unmodeled accelerations (i.e. truth process noise) are added. Both filters handle biases in the measurements remarkably well, until the biases are so large that landmarks no longer remain in the field of view.

2.5 Conclusions

In this chapter, the work previously done for small body autonomous optical navigation is extended by evaluating sequential methods of state estimation with optical landmark measurements. The standard EKF and the ADF are used to estimate the inertial spacecraft position, velocity, and attitude corrections directly from the pixel and line optical measurements, with Monte Carlo analyses to compare the different techniques.

The ADF performs consistently better than the EKF in the simulations performed, with increasing improvement for higher levels of initial state error and longer intervals between photos of the surface. The computational costs are slightly higher for the ADF versus the EKF, but still well within

computational limitations of onboard systems, especially if only the measurement update portion of the ADF is employed (which also provides most of the performance enhancement). Realistic heritage values from previous missions to small bodies are used wherever possible in the simulations, so the estimation architecture and tuning parameters provided may prove useful to future mission planners and operators.

It is expected that a higher order filter such as the ADF will perform better than the EKF, based on the stronger incorporation within the filter of the known nonlinearities in the dynamics and measurement models. However, the goal of this work is show how much improvement can be obtained, and the conditions that lead to those improvements. This work also indicates that the measurement update portion of the ADF provides most of the improvement in this small body optical navigation scenario, which provides a method to improved performance with lower additional computational cost than employing the full ADF. In other scenarios, and in particular those with larger accelerations in the dynamics, this ratio of performance provided by the measurement update versus the propagation step of the ADF may change.

Chapter 3

Precomputing Process Noise for Onboard Sequential Filters

Process noise is often used in estimation filters to account for unmodeled and mismodeled accelerations in the dynamics. The process noise acts to inflate the covariance over propagation intervals, increasing the uncertainty in the state. In scenarios where the acceleration errors change significantly over time, the standard process noise approach can fail to provide effective representation of the state and its uncertainty. Consider covariance analysis techniques provide a method to precompute a process noise profile along a reference trajectory, using known model parameter uncertainties. The process noise profile allows significantly improved state estimation and uncertainty representation. The new formulation also eliminates the trial-and-error tuning currently required of navigation analysts. As a result, estimation performance on par with the consider filter is achieved without the additional computational cost of the consider filter. A linear estimation problem as described in several previous consider covariance analysis publications is used to demonstrate the effectiveness of the precomputed process noise, as well as a nonlinear descent scenario at the asteroid Bennu with optical navigation.

3.1 Introduction

In almost all statistical estimation problems that involve dynamical systems, there are mismodeled or unmodeled forces that act to cause errors in the expected state of the system. Thus measurements are needed to correct the state, and a formal covariance is also computed to provide a measure of the uncertainty of that estimate. Between measurements, both the estimated state and the covariance are propagated, and the covariance is also inflated to account for the increase in uncertainty introduced by the mismodeled and unmodeled forces. This inflation is commonly labeled as "process noise" (though the term is also used to describe the errors added to the truth trajectory propagation for simulation analysis).

The standard approach for determining the appropriate amount of process noise is often a lengthy trial-and-error procedure that attempts to match the formal covariance to the distribution of errors generated by a Monte Carlo simulation. This process noise is typically modeled as an uncorrelated sequence of Brownian increments, which may enter the deterministic plant directly, or via shaping filters that impose a correlation structure. In other words, the stochastic differential equation can become correlated from the homogeneous portion, but the forcing function is uncorrelated in time and thus the process as a whole is Markov (i.e. the future evolution depends only on the current state). However, there are many scenarios where the magnitude of known unmodeled or mismodeled perturbations can change significantly over the course of a reference trajectory, which can make tuning the standard process noise

challenging. If the perturbation magnitude increase is significant enough, the standard process noise model may lead to a divergent filter.

An example where significant state-dependent perturbation magnitudes occur is a spacecraft descent scenario to the surface of a newly explored celestial small body such as an asteroid or comet. Onboard spacecraft navigation systems often use truncated spherical harmonic gravity models of the bodies they orbit in order to reduce computational requirements for propagation of the spacecraft position and velocity state about the body. Additionally, higher order gravity terms may not be observable in the higher orbits before a descent maneuver. These higher order gravity terms, along with errors in the estimated lower order gravity terms, can introduce significant errors in the trajectory as the spacecraft descends to the surface. These errors can lead to degraded filter performance and strongly affect the spacecraft's ability to land accurately and locate landmarks for optical navigation. More generally, Wright [141] has shown that the errors resulting from using imperfect spherical harmonic gravity coefficients and a truncated gravity model are correlated in time. For these autocorrelated noise processes, the standard process noise approach can fail to provide effective representation of the state uncertainty as well as effective estimation of the state. Thus a better method for computing process noise is needed.

The method derived in this chapter computes the process noise for each interval between measurements of a reference trajectory by mapping model uncertainty into state uncertainty, as is done in Consider Covariance Analysis (CCA) and consider filters such as the Schmidt-Kalman Filter (SKF) [115].

CCA is covered extensively by Tapley [121] for the linearized method, and Lisano [77] using sigma point transforms. However, in CCA the consider covariance is computed independently and does not affect the performance of the underlying filter.

In the SKF, first introduced by Schmidt in 1966 [115, 140], the uncertainties in the model parameters do affect the estimation of the state variables, and can provide significant improvement to the state estimation without separate process noise added. As a result, process noise tuning is only necessary for unmodeled perturbations that are not related to the consider parameters, and any state-dependent perturbations are properly included. However, with the additional considered parameters the SKF becomes more computationally demanding than the standard Kalman Filter (KF), and may prove computationally intractable for onboard systems. The additional computational burden can be partially mitigated by avoiding unnecessary calculations associated with consider states that are structurally uncorrelated from the vehicle dynamics, such as measurement biases. However, such an approach does not apply when the consider covariance terms directly relate to the vehicle dynamics, such as the gravity spherical harmonic coefficients. The difference between the SKF and KF becomes more pronounced as the number of considered parameters increases, particularly when considering many model parameters (e.g. a gravity field with thousands of terms). Thus when considering highly limited computational systems such as those onboard a spacecraft, the question arises: is it possible to obtain most or all of the benefits of the SKF without the higher computational costs?

The answer to this question is in fact yes, though some trade-offs must occur: the process noise must be precomputed along a reference trajectory, which must be available and reasonably approximate the true trajectory, and the precomputed process noise must be stored onboard in the form of a table or interpolation coefficients. The precomputation of the process noise profile along the reference trajectory can be performed using linearized techniques involving the Extended Kalman Filter (EKF) and Extended Schmidt-Kalman Filter (ESKF), as described in the "Method of Solution" section. The process noise precomputation can also be accomplished using sigma point transformations. The most common sigma point transformation is the Unscented Kalman Filter (UKF), the unscaled form of which is applied by Stauch and Jah to the SKF to derive the Unscented Schmidt-Kalman Filter (USKF) [119]. "Unscaled" indicates that no central sigma point value is computed and thus no tuning parameters are necessary. Stauch obtains the same final form as in Zanetti and DeMars [146], but through a different derivation. Note that, like the ESKF, the USKF does not resolve the issue of onboard computational limits. However, the USKF is a key element of the process noise precomputation algorithm, as explained in more detail in the "Method of Solution" section.

DeMars and Bishop [40] use the linearized approach to map model uncertainties to estimation state uncertainties for the purposes of precomputing process noise for onboard navigation. They also analyze interpolation methods for precomputed process noise between measurement updates. The current work takes these efforts a step further by incorporating the precomputed process noise into the onboard state and covariance estimation. In addition, we

show how a covariance analysis involving covariance corrections is necessary to provide the appropriate cross-covariance contributions to the precomputed process noise profile. Without updates, these cross-covariance contributions grow without bound; without them, the precomputed process noise profile is incomplete following an expected measurement update.

While there are many advantages to precomputing the process noise, the technique assumes the truth trajectory will not deviate too far from a reference trajectory. Another assumption is that the error in the dynamics model parameters is roughly equivalent to the parameter uncertainties used in the precomputation of the process noise. If the error in the dynamics model parameters is significantly different than the assumed uncertainty, or there are totally unmodeled perturbations, then the precomputed process noise might be significantly different than the level of truth perturbations. In this scenario, adding a blindly tuned standard process noise (on top of the precomputed process noise described in this chapter) might be necessary to account for the mismodeled and unmodeled perturbations. A limited analysis is performed to investigate differences in the model error versus the assumed model uncertainties. Also note that this chapter does not address another important tuning parameter in an onboard filter: the measurement noise uncertainty. Application of the new method using measurement model parameters as consider states in order to compute appropriate measurement noise is saved for future analysis.

3.2 Process Noise

Before the process noise precomputation algorithm is derived, the relevant process noise terms must be defined. Consider a random dynamical process obeying the linear differential equation

$$\Delta\dot{x}(t) = F(t)\Delta x(t) + G(t)u(t) \tag{3.1}$$

with *a priori* value Δx_0 at time $t = 0$. $\Delta x(t)$ is the deviation from the reference state, $u(t)$ is the system model error, $F(t)$ describing the system dynamics, and $G(t)$ maps the model error to the state error. If linearizing a non-linear system, $F(t)$ and $G(t)$ are partial derivative matrices evaluated at the nominal state. "Formally" integrating Eq. 3.1 from $t = 0$ to $t = t_k$ gives

$$\Delta x(t_k) = \Phi(t_k, t_0)\Delta x_0 + \int_0^{t_k} \Phi(t_k, t')G(t')u(t')dt' \tag{3.2}$$

where $\Phi(t_k, t_0)$ is the state transition matrix. Define the state error covariance at time t_k as

$$P_k \equiv E\left[\Delta x(t_k)\Delta x^T(t_k)\right] \tag{3.3}$$

and the process noise autocovariance as

$$Q(t, t') \equiv E\left[u(t)u^T(t')\right]. \tag{3.4}$$

There is no assumption that the process noise is uncorrelated at separate times. The covariance at time t_k is

$$P_k = \Phi(t_k, t_0)P_0\Phi^T(t_k, t_0) + \int_0^{t_k}\int_0^{t_k} \Phi(t_k, t')G(t')Q(t', t'')G^T(t'')\Phi^T(t_k, t'')dt'dt'' \tag{3.5}$$

assuming that $u(t)$ is not correlated with the *a priori* value Δx_0; but *not* assuming that $u(t)$ will be uncorrelated with $\Delta x(t)$ at other times [121].

Assuming that $Q(t,t') = Q(t)\delta(t-t')$ (i.e. the process noise increments are uncorrelated), one of the integrals in Eq. 3.5 is annihilated. More fundamentally, since future noise increments depend in no way on the system's past history, the present moments of $\Delta x(t_k)$ give the only information useful for predicting future values. This characteristic is known as the Markov property. As a result of this assumption, the process noise for a spacecraft position and velocity can be expressed as

$$Q_k = q \begin{bmatrix} \frac{1}{3} I_3 \Delta t_k^3 & \frac{1}{2} I_3 \Delta t_k^2 \\ \frac{1}{2} I_3 \Delta t_k^2 & I_3 \Delta t_k \end{bmatrix} \tag{3.6}$$

where I_3 is the 3x3 identity matrix, Δt_k is the propagation time from the previous measurement time to the current measurement time, and q is the single tuning parameter [121]. Equation 3.6 is a common process noise form, which we shall hereafter refer to as the traditional form.

By contrast, Wright [141] observes that errors in the gravity model used for orbit determination induce a noise process that is correlated in time. In other words, Wright shows that when Eq. 3.1 describes errors in predicting the evolution of a satellite orbit due to gravity model errors, there is a correlation structure among future and past noise increments that makes Eq. 3.1 a non-Markov process, which $Q(t,t') = Q(t)\delta(t-t')$ fails to capture. He provides an alternative, autocorrelated, but approximately Markov, model suitable for circular or near-circular orbits, based on projection of the gravity model error covariance onto a sphere. However, there are many scenarios that do not

meet the criteria required for Wright's model, such as a descent trajectory to the surface of a small body. Thus an alternative method is needed that can determine process noise for any mission scenario.

3.3 Method of Solution

Denote the double-integral process noise covariance term of Eq. 3.5 as

$$Q_d(t_k, t_0) = \int_0^{t_k} \int_0^{t_k} \Phi(t_k, t')G(t')Q(t', t'')G^T(t'')\Phi^T(t_k, t'')dt'dt'' \tag{3.7}$$

This chapter investigates $Q_d(t_k, t_0)$ for arbitrary force model errors, with the aim to develop approximations suitable for use in onboard robotic navigation. In other words, the process noise used to inflate the state uncertainty across propagation intervals in order to appropriately reflect dynamical model perturbations is precomputed along a reference trajectory. To understand how this can be done, it helpful to first describe the components of the covariance propagation.

Let $x(t)$ denote the Cartesian state of a satellite, which evolves according to the propagation function ϕ:

$$x(t) = \phi(t, x_0, c) \tag{3.8}$$

where c is a vector of uncertain model parameters. Let $\hat{x}(t)$ and $\hat{c}$ respectively be the estimate of $x(t)$ and c maintained by a navigation filter, which assumes the model

$$\hat{x}(t) = \hat{\phi}(t, \hat{x}_0, \hat{c}) \tag{3.9}$$

Then the state error can be written as

$$\Delta x(t) = \phi(t, x_0, c) - \hat{\phi}(t, \hat{x}_0, \hat{c}) \tag{3.10}$$

Adding and subtracting $\phi(t, \hat{x}_0, c)$ yields

$$\Delta x(t) = [\phi(t, x_0, c) - \phi(t, \hat{x}_0, c)] + [\phi(t, \hat{x}_0, c) - \hat{\phi}(t, \hat{x}_0, \hat{c})] \tag{3.11}$$

The first bracketed expression is the error due solely to the initial state error, and the second bracketed expression is the error due solely to force model errors. Rewriting these expressions as

$$\Delta x(t) = e_{x0}(t) + e_c(t) \tag{3.12}$$

the covariance of the final error can be written as

$$\begin{aligned} P(t) &= E\left[e_{x0}e_{x0}^T + e_c e_c^T + e_c e_{x0}^T + e_{x0}e_c^T\right] \\ &= P_{x0}(t) + P_{cc}(t) + P_{cx0}(t) + P_{cx0}^T(t) \end{aligned} \tag{3.13}$$

Note that there are three contributions to the final mapped covariance: $P_{x0}(t)$ (contribution from the initial state uncertainty), $P_{cc}(t)$ (directly mapped contribution from the model uncertainty), and $P_{cx0}(t) + P_{cx0}^T(t)$ (cross-correlation contribution between the state uncertainty and the model uncertainty). The $P_{x0}(t)$ term is typically computed in the onboard filter, using the limited dynamical models and assumed model values. The onboard filter also adds process noise to the mapped covariance, under the assumption that the dynamics are not modeled perfectly. Thus it is ideal to use the sum of the $P_{cc}(t)$ and $P_{cx0}(t) + P_{cx0}^T(t)$ terms as this process noise. Comparing equation 3.13 to equation 3.5 and 3.7, the expression for $Q_d(t_k, t_0)$ becomes

$$\begin{aligned} Q_d(t_k, t_0) &= P_{cc}(t_k, t_0) + P_{cx0}(t_k, t_0) + P_{cx0}^T(t_k, t_0) \\ &= P(t) - P_{x0}(t) \end{aligned} \tag{3.14}$$

However, due to onboard computational limits, these values are precomputed, which requires that they be computed along a known reference trajectory. To precompute $Q_d(t_k, t_0)$ for each interval of a reference trajectory, the new approach makes use of consider covariance and filtering methods such as the ESKF [140], USKF [119], and the newly developed Additive Divided Difference Schmidt Kalman Filter (ADSF) described in the next section. The resulting precomputed process noise can be used in computationally efficient filters such as the EKF. Note that the result of the subtraction in equation 3.14 has the potential to be come negative definite if the reference trajectory used differs greatly from the truth trajectory; for this reason, a small additional standard process noise quantity may become necessary.

These covariance contributions can be mapped via linearized integration or by sigma point transformations. The linearized covariance propagation equations that are numerically integrated are obtained from the SKF, as described by Woodbury [140] and DeMars [40]:

$$\begin{aligned} \dot{\hat{x}}(t) &= F(t)\hat{x}(t) + G(t)c \\ \dot{P}_{xx}(t) &= F(t)P_{xx}(t) + P_{xx}(t)F^T(t) + P_{xc}(t)G^T(t) + G(t)P_{xc}^T(t) \\ \dot{P}_{xc}(t) &= F(t)P_{xc}(t) + G(t)P_{cc} \end{aligned} \tag{3.15}$$

where c is the nominal vector of considered model parameters (which are in general not equal to the truth model parameters). Note that the integration of $P_{xx}(t)$ is dependent on $P_{xc}(t)$. Thus the final two terms of the $\dot{P}_{xx}(t)$ equation cannot be integrated independently due to this coupling, though doing so can provide a reasonable approximation for some systems. Additionally, the

dependence on the $P_{xc}(t)$ terms requires that the measurement updates of the $P_{xc}(t)$ be included, as described in the equations:

$$\begin{aligned}
\bar{y} &= H_x \bar{x} + H_c \hat{c} \\
P_{xy} &= P_{xx}^- H_x^T + P_{xc}^- H_c^T \\
P_{yy} &= H_x P_{xx}^- H_x^T + H_x P_{xc}^- H_c^T + H_c P_{cx}^- H_x^T + H_c P_{cc}^- H_c^T + R \\
K &= P_{xy} P_{yy}^{-1} \\
P_{xx}^+ &= (I - K H_x) P_{xx}^- - K H_c P_{xc}^T \\
P_{xc}^+ &= (I - K H_x) P_{xc}^- - K H_c P_{cc}^T
\end{aligned} \tag{3.16}$$

where H_x and H_c are the measurement partials with respect to the state and consider parameters, R is the measurement covariance, and K is the Kalman gain. Note that when performing these updates as part of the precomputation of the process noise, the state is not updated (as there are no measurements) and the reference trajectory is used to determined expected measurements at each time (as is done in standard covariance analysis). The covariance update expressions in equation 3.16 can also be formulated using the Joseph form [121], which is more computationally tractable and holds true when the Kalman gain K is not optimal (though the non-Joseph form is still often used for onboard filters, despite the suboptimal gain).

The final process noise profile is obtained by taking the difference in the prefit P_{xx}^- terms between the standard KF and the SKF at each measurement time (as described in equation 3.14), which are computed by performing covariance propagation and updates along a reference trajectory. This difference provides the full process noise contribution of both the $P_{cc}(t_k, t_0)$ and

$P_{cx0}(t_k, t_0) + P_{cx0}^T(t_k, t_0)$ terms. Note that the KF and SKF covariance analyses are performed simultaneously, and the computed process noise after each propagation is added to the KF propagated covariance before performing the KF covariance update (keeping the KF covariance and state portion of SKF covariance equal before performing the covariance updates).

As a result, the filter performance is approximately equal (and exactly equal for linear systems) to the SKF, without the need to compute onboard the effect of the consider parameter uncertainty on the state uncertainty. The overall algorithm is depicted in Figure 3.1. Note how the precomputed process noise is dependent not only on the model parameter uncertainty, but also the initial state uncertainty (due to the measurement updates of the cross-covariance terms), the measurement model and nominal expected measurements along the reference trajectory, and the time between measurements.

3.3.1 The Additive Divided Difference Sigma Point Schmidt-Kalman Filter

While the process noise profile can be precomputed with a linearized approach using the EKF and ESKF, as shown in equations 3.15 and 3.16, it is also possible to accomplish this precomputation using sigma point transformations. One sigma point formulation that can be employed is the Additive Divided Difference Sigma Point Filter (ADF) described in section 2.2.2.1.

To reformulate the ADF as the ADSF consider filter, the consider parameters are added to the state and the state and covariance propagation steps are performed in the same way. For the state and covariance update steps,

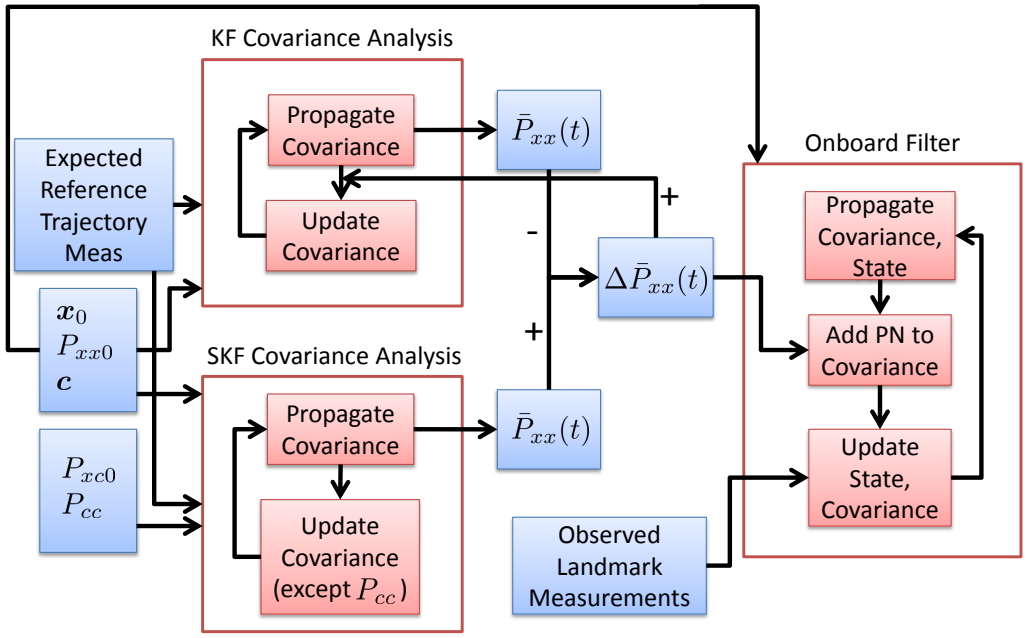

Figure 3.1: Process Noise Algorithm

the state update to the consider parameters is set to zero, and the portion of covariance directly corresponding to the consider parameters is also not updated (though the state and cross-covariance terms are corrected), as shown by

$$P_{zz}^{+} = \begin{bmatrix} P_{xx}^{-} & P_{xc}^{-} \\ P_{cx}^{-} & P_{cc} \end{bmatrix} - \begin{bmatrix} K_x P_{yy} K_x^T & K_x P_{yy} K_c^T \\ K_c P_{yy} K_x^T & 0 \end{bmatrix} \tag{3.17}$$

where $K = \begin{bmatrix} K_x \\ K_c \end{bmatrix}$, or using the difference method as described in equation 2.18 and setting the P_{cc} update to zero by reseting it to the original value. The difference in state covariance matrices for the ADF and ADSF are computed to generate the process noise profile that is used in the onboard filter.

3.4 Linear Problem: Falling Object Scenario

A simple, linear estimation problem is used throughout the literature for demonstration of consider covariance analysis and filtering techniques, and proves effective in showing the utility of the new process noise computation method. Additionally it is used to verify correct implementation of the algorithms. The problem is a one dimensional falling object scenario, with an uncertain gravity model value. This problem is employed in Stauch [119], Tapley [121], Lisano [77], and Woodbury [140]. The point mass in freefall is shown in Figure 3.2. The state consists of the position x and velocity $\dot{x}$, while the gravitational parameter g is a consider parameter. The position range y is directly measured.

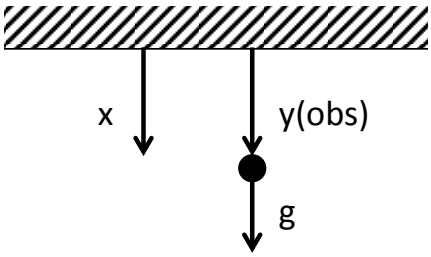

Figure 3.2: Free Falling Point Mass

3.4.1 Simulation Scenario

The nominal initial conditions are

$$x_{nom}(t_0) = 1\ m, \quad \dot{x}_{nom}(t_0) = 0\ m/s, \quad g_{nom} = 10\ m/s^2 \tag{3.18}$$

while the truth initial conditions are

$$x_{tru}(t_0) = 0.8\ m, \quad \dot{x}_{tru}(t_0) = 0.3\ m/s, \quad g_{tru} = 9.8\ m/s^2 \tag{3.19}$$

The initial state covariance, state-consider cross-covariance, consider parameter g uncertainty, and measurement uncertainty are

$$P_{xx0} = \begin{bmatrix} 1 & 0 \\ 0 & 1 \end{bmatrix}, \quad P_{xc0} = \begin{bmatrix} 0 \\ 0 \end{bmatrix}, \quad P_{cc} = [1], \quad R = [1] \tag{3.20}$$

Note that the initial error for this single simulation is well within the initial state and consider parameter uncertainty distributions.

The position range y is directly measured every second from 0 to 10 seconds, and the measurement error is set to zero for this simple linear problem (though importantly the measurement uncertainty is non-zero for each measurement). The process noise for this linear problem is computed as described in the "Method of Solution" section, taking the difference between the prefit KF state covariance and prefit SKF state covariance at each measurement time. The precomputed process noise is added to the state covariance at the end of each propagation interval between measurements.

3.4.2 Results

First the linear scenario is run with both the KF and SKF, with no process noise added to the KF after each propagation of the state uncertainty. The resulting position and velocity errors and 1-σ covariance values are shown in Figure 3.3. These results are identical to those shown in Stauch [119]. The KF without process noise added does not account at all for the uncertainty in the gravity value, and as a result the estimated covariance artificially converges while the state error diverges.

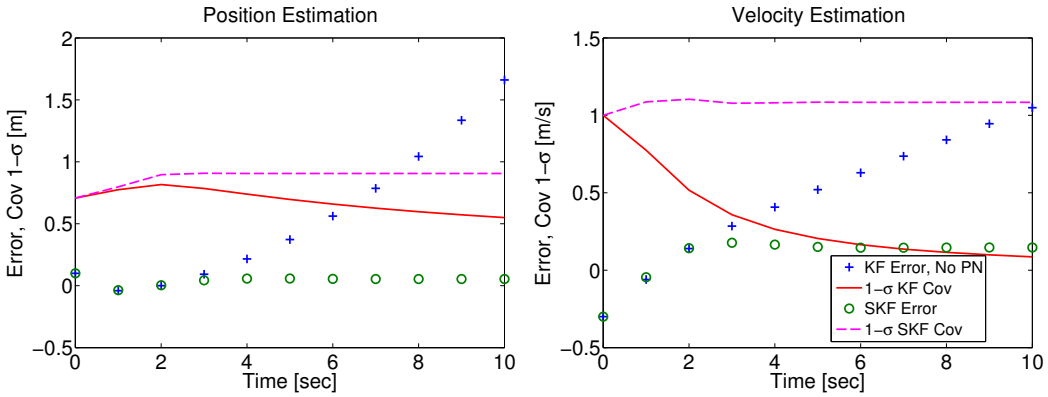

(a) Position (b) Velocity

Figure 3.3: SKF versus KF without Process Noise

To account for the uncertainty in the gravity term, process noise must be added. To start, the consider state (gravity) uncertainty is mapped into the state space over each propagation interval, which provides the $P_{cc}(t)$ term as shown in equation 3.13. Using only this term as the process noise, the KF performance significantly improves, as shown in Figure 3.4. Most of the

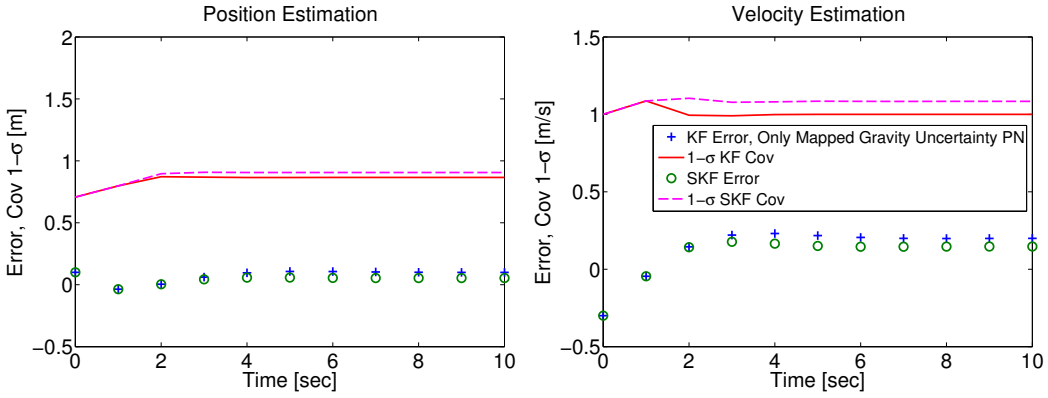

(a) Position (b) Velocity

Figure 3.4: SKF versus KF with Only Mapped Gravity Uncertainty Process Noise

performance gain of the SKF over the KF is achieved by adding this $P_{cc}(t)$ process noise term. However, the KF performance does not fully match the performance of the SKF, with slightly lower uncertainty values and slightly higher error values. In an attempt to achieve better performance with the KF, the process noise values $P_{cc}(t)$ derived from the gravity uncertainty mapping are multiplied by a factor of three. This simple multiplication of the covariance is equivalent to how standard filter tuning operates (except standard process noise doesn't have the $P_{cc}(t)$ starting point). The result is shown in Figure 3.5. A factor of three was chosen (by trial and error) to obtain KF errors on

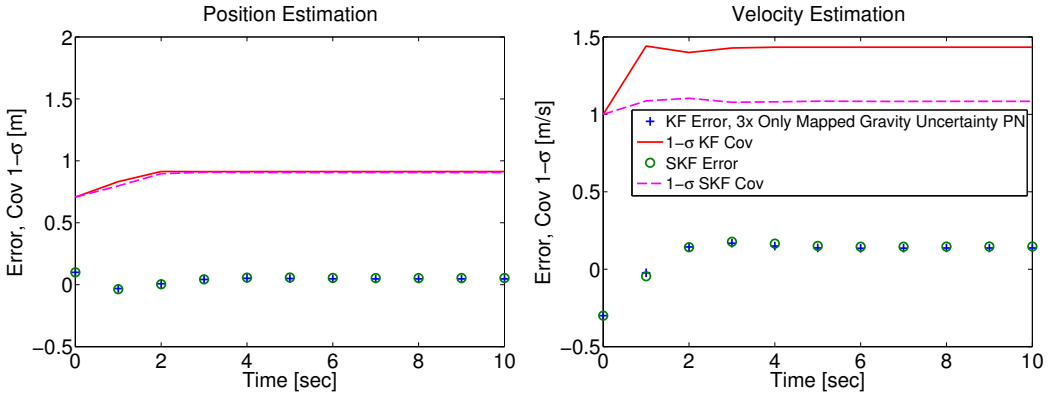

(a) Position (b) Velocity

Figure 3.5: SKF versus KF with 3x Only Mapped Gravity Uncertainty Process Noise

par with the SKF, but as a result the velocity uncertainty is greatly inflated.

To understand why the KF doesn't match the SKF, and why no amount of modifying the $P_{cc}(t)$ term will produce matching results, is it helpful to plot the magnitude of the $P_{cc}(t)$ variance values versus the $2P_{cx0}(t)$ term variance values and the full process noise $P(t)$ variance values as described in equation

3.13. This plot is shown in Figure 3.6. Because of the linear nature of the

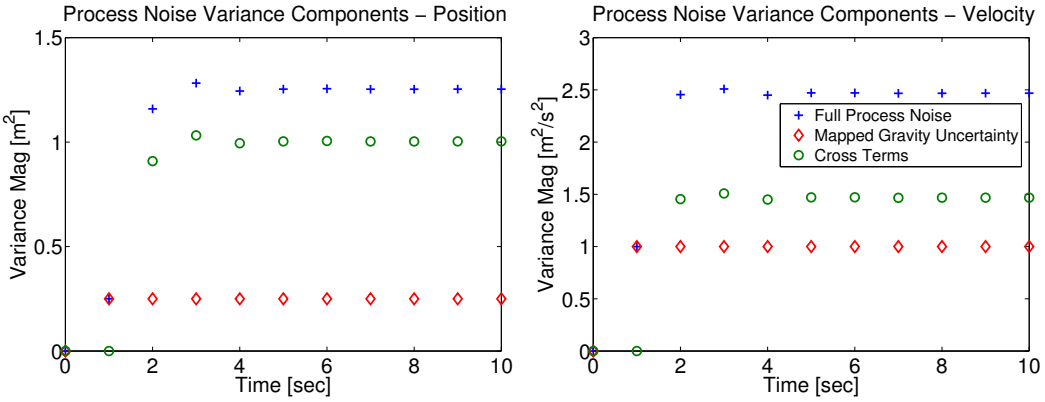

(a) Position (b) Velocity

Figure 3.6: Process Noise Component Variance Magnitudes (1-σ)^2

problem, the $P_{cc}(t)$ contribution is identical for each segment, but the $2P_{cx0}(t)$ cross contributions change significantly and are greater in magnitude than the $P_{cc}(t)$ contribution starting at two seconds past the start time. Note that the variance values are plotted instead of the 1-σ standard deviation values to show how the $P_{cc}(t)$ and $2P_{cx0}(t)$ cross contribution values added together produce the full process noise variance values. If the full process noise is used in the KF, the resulting performance matches exactly the SKF, while using the computationally much less expensive KF, as shown in Figure 3.7.

Note that identical precomputed process noise values and overall simulation results are achieved using three different filter forms: the EKF and ESKF, the UKF and USKF, and the ADF and ADSF. Achieving identical results for these different non-linear filters in a linear problem provides a strong sanity check for the algorithm implementation.

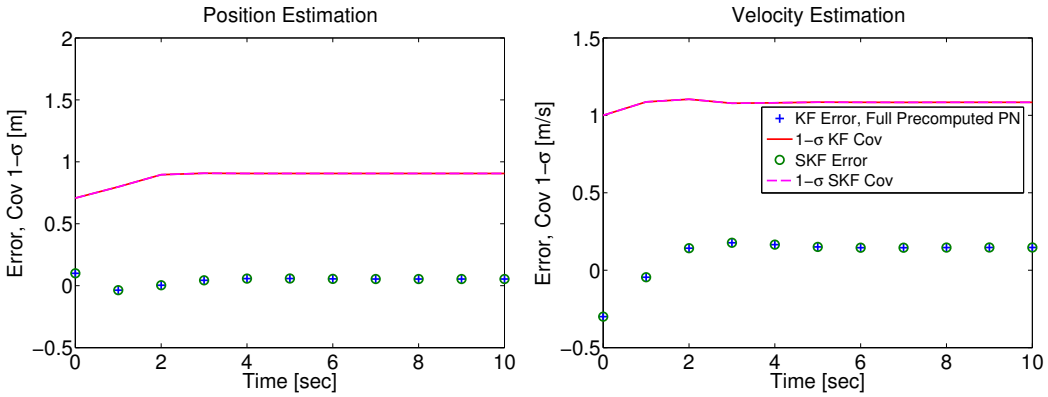

(a) Position (b) Velocity

Figure 3.7: SKF versus KF with Full Precomputed Process Noise

3.5 Nonlinear Problem: Asteroid Descent Scenario

Precomputed process noise is next generated for a nonlinear estimation problem: a spacecraft descent scenario to a checkpoint above the surface of an asteroid, using surface landmarks for optical navigation. The descent scenario simulated matches the currently planned descent trajectory of NASA's OSIRIS-REx asteroid sample return mission during the sample collection phase of the mission, ending at a predetermined checkpoint above the surface. The simulated camera also matches the specifications of the NavCam camera intended for optical navigation during the descent. There are several challenges in this scenario which make use of the new process noise precomputation method:

- Onboard computational limits
- Prior to the descent trajectory, only limited gravity field estimates are available

- The magnitude of the central body and gravity harmonics perturbations increase significantly during the descent trajectory, which exacerbate dynamical errors resulting from lower order gravity term errors and truncation of higher order gravity terms

3.5.1 Simulation Scenario

The reference descent trajectory employed in this simulation is shown in the inertial and body-fixed frames in Figure 3.8. Note that the object plotted in the Figure 3.8a is the Brillouin Sphere (i.e. a sphere with radius equal to the largest radius of the asteroid), while the object in Figure 3.8b is a triaxial ellipsoid with minimum, median, and maximum radii corresponding to the current best estimated dimensions of the asteroid Bennu (the intended target of the OSIRIS-REx mission). Figure 3.8b also shows a portion of the 300 predetermined and randomly located surface landmarks assumed known for this simulation. Remaining above the Brillouin Sphere also allows spherical harmonics to be used for the entire trajectory.

The simulation setup, including timing and initial spacecraft states, is described in Table 3.1. Note that for the onboard optical navigation, photos are taken every two minutes during the descent trajectory. The descent trajectory is also chosen such that lit landmarks will visible for the entirety of the trajectory.

The properties of the small body used for the simulations are given in Table 3.2. Note that the triaxial ellipsoid from Figure 3.8b is used as the shape model in the simulations. While a higher fidelity polyhedron shape model is

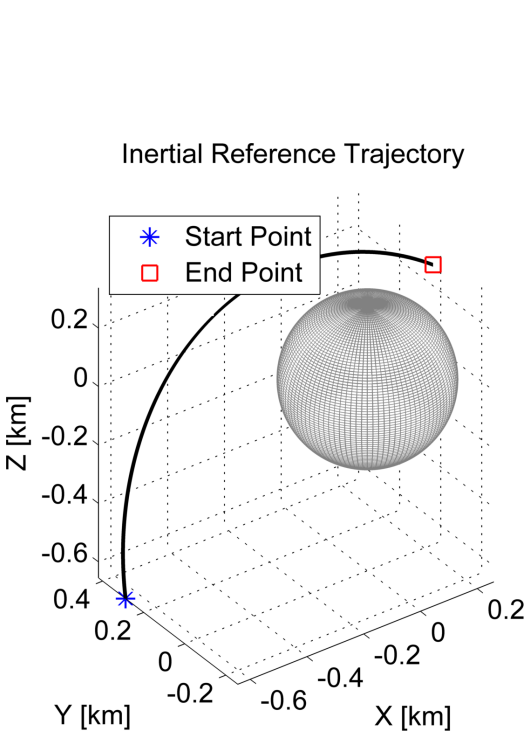

(a) Inertial Frame

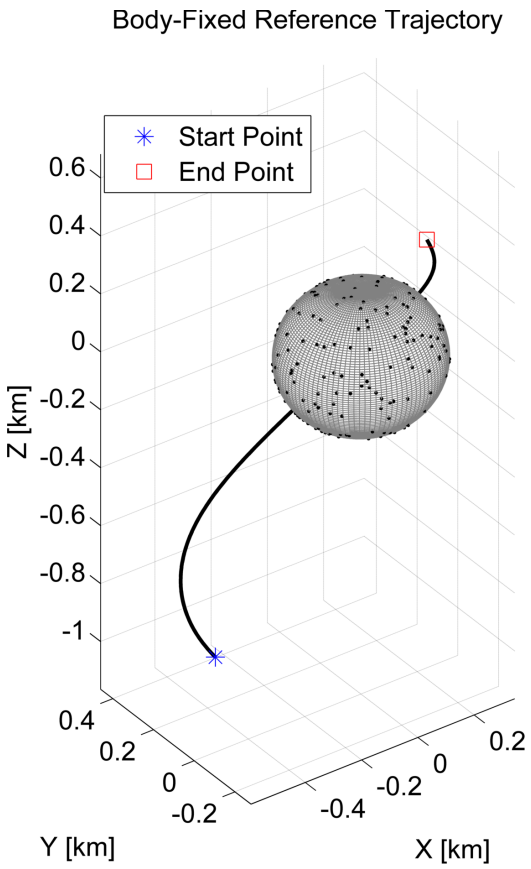

(b) Body-Fixed Frame

Figure 3.8: Descent Trajectory

Table 3.1: Simulation Setup

Simulation Parameter	**Values**
Epoch Time	11-Oct-2019 12:17:04.953
End Time	11-Oct-2019 16:17:04.953
Minimum Time Before First Update	1 minute after epoch
Time Between Photos	2 minutes
Spacecraft Initial Position	[-0.644, 0.288, -0.655] km
Spacecraft Initial Velocity	[1.182x10^{-5}, 3.009x10^{-5}, 6.368x10^{-5}] km/s

available, it is not necessary to evaluate the new process noise algorithm. The

Table 3.2: Asteroid Properties

Simulation Parameter	**Nominal Values**
Initial Pole Right Ascension, Declination	0, 10 deg
Pole Right Ascension, Declination Rates	2, 3 deg/Julian century
Longitude of the Prime Meridian at Epoch	0 deg
Rotation Rate	2010.489449 deg/day
GM	$5.2\text{x}10^{-9}$ km^3/s^2
GM Uncertainty (1- σ)	$5.2\text{x}10^{-11}$ km^3/s^2 (1%)
Radius Values	$0.259 \times 0.250 \times 0.230$ km
Number of Landmarks on surface	300
Nominal Gravity Harmonics	4 x 4 (Bennu Estimate) [83]
Truth Gravity Harmonics	12 x 12 (Bennu, Perturbed)
Gravity Harmonic Uncertainties	Modified Kaula Rule [83]

asteroid GM and nominal spherical harmonic coefficients for Bennu are provided in McMahon [83]. McMahon also provides a Modified Kaula Rule that has been derived for Bennu, which provides realistic maximum uncertainties for the gravity spherical harmonic coefficients. The upper bound expressions of both the zonal coefficients ($0.183/n^2$) and non-zonal coefficients ($0.043/n^2$) are used as the uncertainties in the harmonic coefficients up to degree and order 12. Note that the uncertainties for the GM and lower order terms are likely to be significantly lower from estimation of the terms in the mapping orbits of the preceding mission phases, but a more strenuous scenario is sought to evaluate the new precomputed process noise method.

3.5.2 Dynamical Model

The spacecraft position and velocity are propagated via numerical integration between picture times using fixed step RK8 propagation. The covariance is numerically integrated to the same times, also using fixed step RK8 propagation. The simulation includes central body acceleration and perturbations from a spherical harmonic gravity field, for both the truth and filter dynamics. Standard perturbations such as third body perturbations (TBP) and solar radiation pressure (SRP) are not included for simplicity, as the focus of this analysis is to evaluate the new process noise algorithm in the context of gravity field uncertainty. These SRP and TBP terms also do not change significantly in magnitude over the descent trajectory, unlike the direct gravity forces and perturbations.

A 4x4 degree and order spherical harmonic gravity model of the Bennu asteroid that is employed for mission design analysis of the OSIRIS-REx mission is used for the nominal onboard dynamics model. To obtain a higher order 12x12 gravity field for each of the truth trajectories, first the uncertainties for the 12x12 field are sampled to generate errors for each of the 12x12 field coefficients. For the lower order 4x4 field values, these errors are added to the non-zero nominal 4x4 field values (which are expected to be estimated in the prior mapping orbit) to obtain the truth 4x4 coefficients. For the higher order terms up to 12x12, these errors are added to the zero value (i.e. truncated) nominal coefficients: the error values become the coefficient values. As described in the Simulation Scenario section above, these coefficient uncertainties are obtained from the Modified Kaula Rule [83], which provides maximum

deviations from zero of the spherical harmonic coefficients. Thus using these uncertainties for the higher order terms allows us to account for the "errors of omission" introduced by the truncation of the gravity field.

3.5.3 Measurement Model

The navigation simulation uses optical landmark measurements, as defined in section 1.1. The assumed landmark measurement errors are in line with those expected from using the maplet stereophotoclinometry method for the landmarks [44]. It is assumed that the spacecraft is commanded to point its camera at the center of mass of Bennu using onboard position and attitude knowledge at every picture time using reaction wheels or thrusters. A similar simulation can be performed using a predetermined inertial attitude profile.

The navigation camera parameters are described in Table 3.3. These parameters match the NavCam camera planned for navigation use in the OSIRIS-REx mission. Camera distortion effects that are typically calibrated in flight are not included in these simulations, nor are the remaining errors after calibration at the FOV edges that are more likely for a wide FOV lens.

Table 3.3: Navigation Camera Properties

Simulation Parameter	**Nominal Values**
Focal Length	7.68 mm
Sensor Array	2592 × 1944 pixels
Pixel Density	454.54 pixels/mm
Field of View (FOV)	40.74° × 31.12°

3.5.4 Estimation Filter Architecture

A sequential EKF is employed to evaluate the effectiveness of the new process noise model. The estimated states are the spacecraft position and velocity. It is assumed that the small body orientation, rotational velocity, shape model, gravity field, and set of surface landmarks listed in Table 2.2 have been previously estimated. These quantities are held as constants in the "onboard" filter. A summary of onboard filter parameters is shown in Table 3.4 [15, 16].

Table 3.4: Onboard Filter Parameters

Simulation Parameter	**Nominal Values**
Initial Filter Position Covariance (Radial, In-Track, Cross-Track) (1-σ)	[0.012, 0.053, 0.004] km
Initial Filter Velocity Covariance (Radial, In-Track, Cross-Track) (1-σ)	[3.92x10^{-6}, 5.06x10^{-7}, 3.10x10^{-8}] km/s
Measurement Noise Covariance (1-σ)	[29.5, 29.5] arcsec ([0.5, 0.5] pixels)
Traditional Process Noise q for Position and Velocity	1x10^{-15} km^2/s^3

The spacecraft attitude is not estimated, nor are knowledge attitude errors added for each photo, because it is assumed that a highly accurate separate attitude determination system (ADS) consisting of gyroscopes, star cameras, and an attitude determination filter will provide attitude estimates at each photo time. Should ADS knowledge attitude errors prove significant (as is predicted for the actual OSIRIS-REx mission due to expected thermal variations in the spacecraft structure), it is possible to further correct the

attitude using landmark observations [93]. It is also not the focus of this analysis to investigate spacecraft attitude estimation performance, but rather how the new process noise algorithm affects spacecraft position and velocity estimation performance.

3.5.5 Monte Carlo Simulation Design

Monte Carlo analyses are employed to compare the standard and pre-computed process noise techniques. A single estimated state and covariance is assumed known at the start of the descent trajectory. Also assumed known are the nominal estimated coefficients for a 4x4 gravity field, as well as a covariance matrix that includes uncertainties up to degree and order 12.

The errors for the initial state, GM, and gravity field coefficients are sampled assuming a Gaussian distribution with the 1-σ values provided in Table 3.5. The error in the GM and gravity spherical harmonics is re-sampled at each photo time to obtain perturbations that are more like process noise, but comparable results are achieved if the error in the GM and gravity spherical harmonics is sampled only once at the beginning of each simulation trial. Note that modern image processing capabilities can generate landmark center values at sub-pixel precision [19, 65] (depending on the relative resolution of the landmark maplet data and the image pixel scale). Thus 0.5 pixel errors, equivalent to 9 arc seconds angular error for this camera, are used in this simulation. In higher fidelity simulations a resolution-dependent term is used for filter measurement noise value, which is neglected in this example for simplicity.

Table 3.5: 1-σ Monte Carlo Error Parameters

Simulation Parameter	**1-σ Values**
Spacecraft Initial Position (Radial, In-Track, Cross-Track)	[0.012, 0.053, 0.004] km
Spacecraft Initial Velocity (Radial, In-Track, Cross-Track)	[3.92x10^{-6}, 5.06x10^{-7}, 3.10x10^{-8}] km/s
Observation	[29.5, 29.5] arcsec ([0.5, 0.5] pixels)
GM	5.2x10^{-11} km^3/s^2 (1%)
Asteroid Gravity Coefficients	Modified Kaula Rule [83]

The initial state errors are used to distribute the initial truth states about the nominal. As a result, a different truth trajectory and set of observations exists for each Monte Carlo trial. A small body mission will have a single estimated nominal state at the beginning of the descent trajectory, which will be used as the reference trajectory for precomputing the process noise. The truth state will not be known, but the Monte Carlo analysis will reveal the performance of the filter with the precomputed process noise method for many different possible truth trajectories. The same logic extends to the asteroid gravity coefficients: only estimates will be known, about which the precomputation of the process noise will occur. As a result, the landmark measurements are at least slightly different for each Monte Carlo trial. The variation in the landmarks detected and used is valuable as an evaluation of the filter performance using precomputed process noise.

3.5.6 Application of Precomputed Process Noise Method

For this scenario, the model parameters of interest that are used to generate precomputed process noise are the gravitational spherical harmonic

coefficients. Using the uncertainties in the GM and spherical harmonics gravity coefficients through degree and order 8 (which is higher order than the 4x4 gravity field used in the "nominal" propagation function $\hat{\phi}$, but lower order than the 12x12 gravity field used in the "truth" propagation function ϕ), the Orbit Error Autocovariance Approximation (i.e. the precomputed process noise profile to use in the onboard filter) is computed via either the linearized or sigma point approaches described in the "Method of Solution" section. These different approaches deliver approximately the same process noise profile in this problem. When using the DDT, the h tuning parameters described in equations 2.3, 2.5, and 2.6 are set equal to standard value of $\sqrt{3}$ [93].

The resulting precomputed 6x6 process noise covariance matrices for each picture time are stored as a 6x6x121 three dimensional array (the 6x6 covariance matrix at 121 time steps), totaling 4356 double precision numbers (34 kB). A table containing these values is possible to use directly onboard if fixed step integration and set measurement times are used. If greater amounts of process noise data are needed, variable step integration is employed, or photos don't occur at predicable times, the process noise covariance sigma and correlation coefficient values can be fit to polynomials. See DeMars [40] for a detailed study of interpolation methods for precomputed process noise between measurements (which would likely need only minimal adjustment to account for measurement updates).

The spacecraft position and velocity covariance is propagated using both the precomputed process noise model and standard process noise model.

The resulting filter performance and spacecraft state uncertainty representation is evaluated for both approaches.

3.5.7 Results

The precomputed process noise position and velocity magnitudes for each two minute interval between measurements for this scenario is plotted in Figure 3.9. Note how the process noise changes significantly in magnitude over the simulation timeline, a feature that is not possible with the traditional process noise model. The cross-covariance terms $2P_{cx0}$ are found to be many orders of magnitude smaller than the $P_{cc}(t)$ terms in this scenario (unlike for the linear estimation problem). In such cases, the required computation can be reduced by calculating only the $P_{cc}(t)$ process noise component for each interval. However, in this analysis, all terms of the process noise are precomputed and utilized.

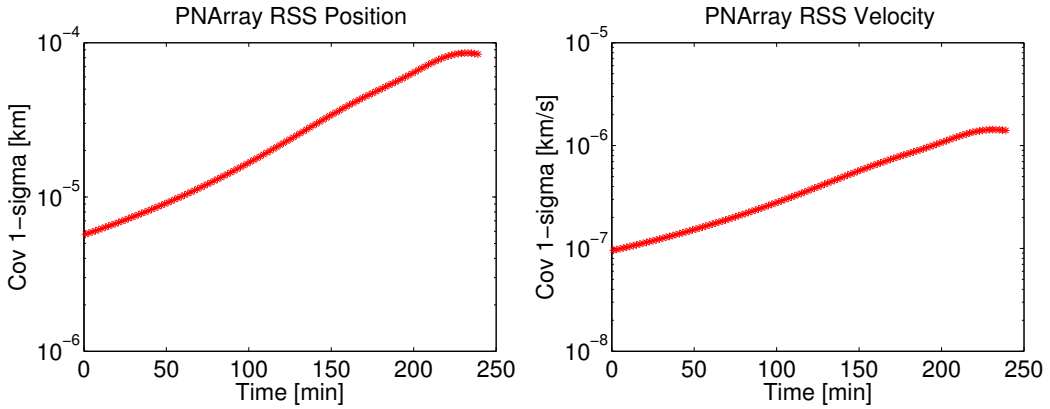

(a) Position (b) Velocity

Figure 3.9: Precomputed Process Noise

To determine the improvement from using the precomputed process noise shown in Figure 3.9, a 100 trial Monte Carlo simulation is run using standard process noise as defined in equation 3.6 and using the q value from Table 3.4. The resulting errors and state uncertainty are shown for position and velocity in Figure 3.10. Note that the Max and RMS statistics provided are for the post-initial-convergence period, starting at the sixth picture time. Next the same Monte Carlo simulation is run using the precomputed process noise profile, with results shown in Figure 3.11.

The precomputed process noise profile results in a 9% reduction of the position error RMS and 17% reduction of the velocity error RMS. Additionally the uncertainty now much better matches the error distribution, particular for the portion of the simulation between hour 3 and hour 4. The "velocity smugness" (i.e. overconfidence in the accuracy of the velocity errors evident from lower formal covariance values) has special significance for the OSIRIS-REx mission due to an abort trigger based on "time of touch" that is sensitive to velocity errors. Note that the position errors and uncertainty are less affected by the process noise chosen than the velocity errors due to the strong position information obtained from low optical measurement errors and uncertainty.

For the standard process noise method, a q value of $1\text{x}10^{-15}$ km^2/s^3 is chosen as the best balance of performance between the start and end of the simulation, an unsatisfactory compromise no longer necessary with the new process noise method. Also unnecessary is the extensive time that it takes to find such a compromise.

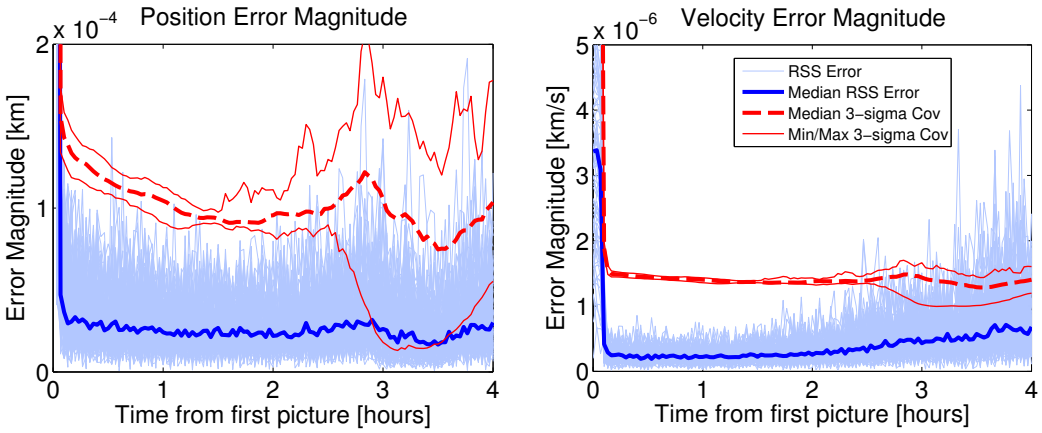

(a) Position, Max **1.9E-4**, RMS **3.5E-5** km (b) Velocity, Max **4.4E-6**, RMS **5.2E-7** km/s

Figure 3.10: Descent Scenario with Traditional Process Noise

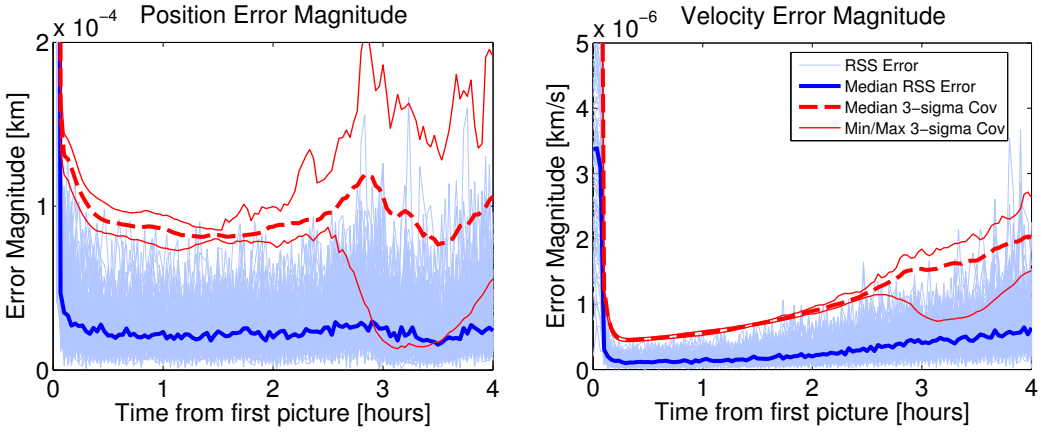

(a) Position, Max **1.7E-4**, RMS **3.2E-5** km (b) Velocity, Max **3.6E-6**, RMS **4.3E-7** km/s

Figure 3.11: Descent Scenario with Precomputed Process Noise

The performance difference between the standard process noise model and the newly developed precomputed process noise becomes more pronounced as the uncertainties in the consider parameters increase. The 1-σ uncertainty values in the GM and gravity coefficient values used to precompute the process

noise and to sample the truth coefficients are increased by one order of magnitude, and the resulting performance with the standard process noise versus the precomputed process noise are shown in Figures 3.12 and 3.13. Note that the process noise q parameter used for the original process noise method is increased from 1x10^{-15} km^2/s^3 to 1x10^{-14} km^2/s^3. The precomputed process noise profile results in a 16% reduction of the position error RMS and 44% reduction of the velocity error RMS.

To determine how the performance of the precomputed process noise changes when the gravity coefficient errors do not match the uncertainty values used to generate the precomputed process noise, the gravity coefficient error 1-σ values are deterministically varied from -50% to +50% of the 1-σ values used for the process noise precomputation. A 100 trial Monte Carlo simulation is performed for each each 10% interval, and the position and velocity error RMS for each interval are plotted in Figure 3.14. Note that lower errors are obtained when the uncertainty values for the precomputed process noise are higher than the error 1-σ values, at the expense of slightly lower formal covariance accuracy. This result suggests that using conservative higher-than-expected gravity uncertainty values in the process noise precomputation may provide lower state errors in an actual mission (though with slightly less realistic uncertainties). A more complete sensitivity analysis of mismatching distributions of the model parameter error versus uncertainty used in the process noise precomputation is saved for future work.

Figure 3.15 shows the number of landmarks visible at each picture time for a single Monte Carlo trial. The plotted number of landmarks is

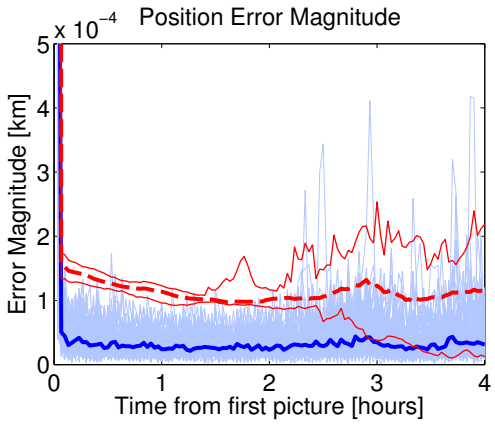

(a) Position, Max **4.2E-4**, RMS **4.5E-5** km

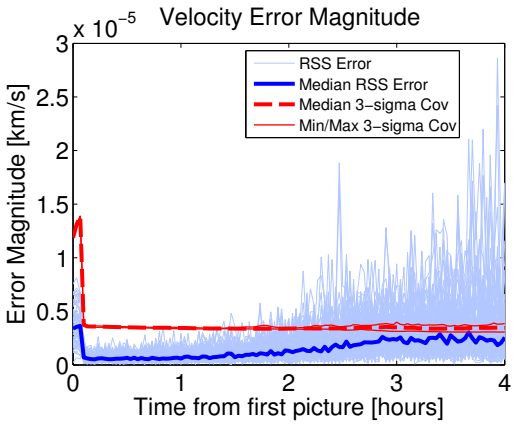

(b) Velocity, Max **2.9E-5**, RMS **2.7E-6** km/s

Figure 3.12: Descent Scenario with Traditional Process Noise, 10x Gravity Uncertainty And Error

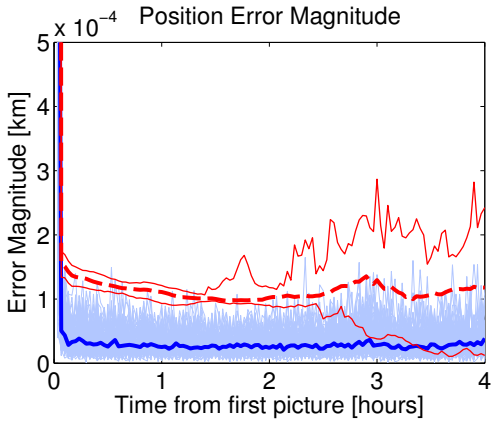

(a) Position, Max **1.6E-4**, RMS **3.8E-5** km

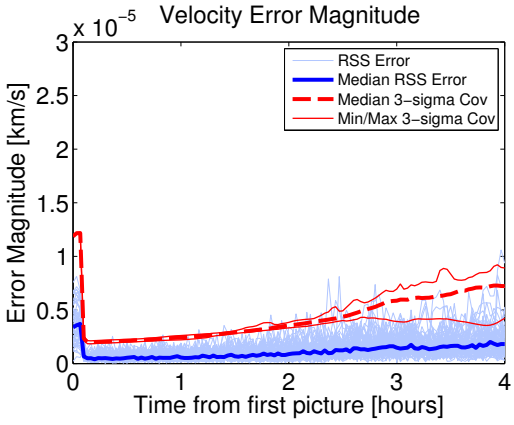

(b) Velocity, Max **1.1E-5**, RMS **1.5E-6** km/s

Figure 3.13: Descent Scenario with Mapped Model Uncertainty as Process Noise, 10x Gravity Uncertainty And Error

representative of the number of visible landmarks in other trials, and the visible landmarks for each trial are identical in the simulations using standard process noise versus the new precomputed process noise.

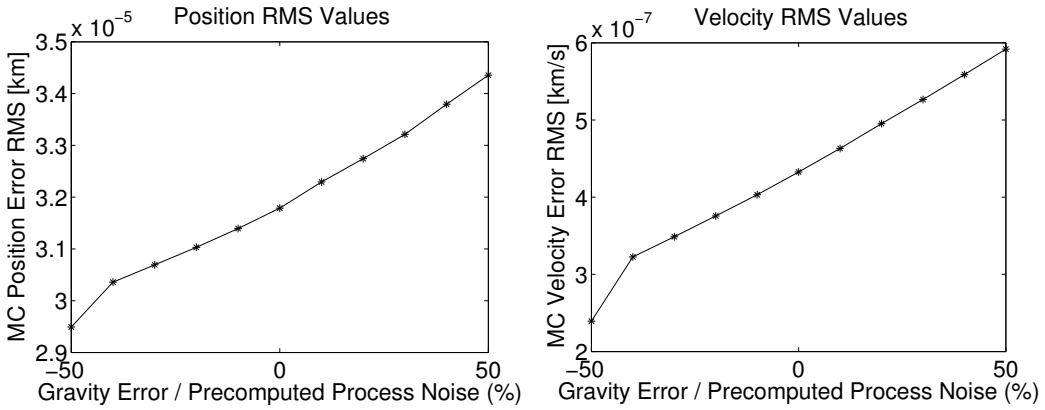

(a) Position (b) Velocity

Figure 3.14: Error RMS values for Gravity Error 1-σ deterministic variations

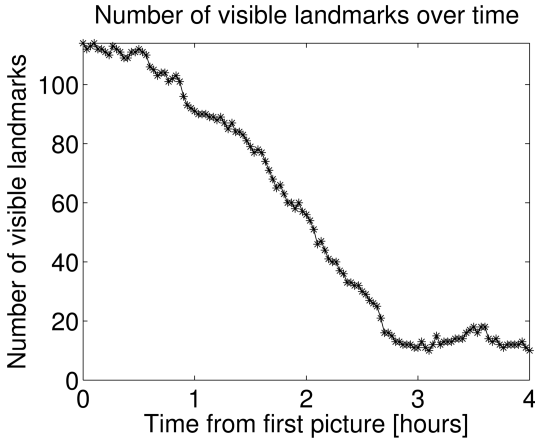

Figure 3.15: Number of Visible Landmarks For Descent Trajectory

In an effort to determine how well the process noise precomputed for a particular reference trajectory works with larger variations of the truth trajectory away from the reference trajectory, the initial spacecraft position and velocity errors and uncertainties from Tables 3.4 and 3.5 are increased from zero to ten times the original values. For each level of initial state error and uncertainty, 100 Monte Carlo trials are performed. The resulting percentage

of diverged trials for each level of initial state error and uncertainty are shown in Figure 3.16. A diverged trial is defined as having position error greater than 0.2 meters after the initialization period, which is chosen based on the magnitude of the formal uncertainties after the initialization period. It is seen that most runs diverge when the initial state errors and uncertainties are increased by a factor of 6 or higher.

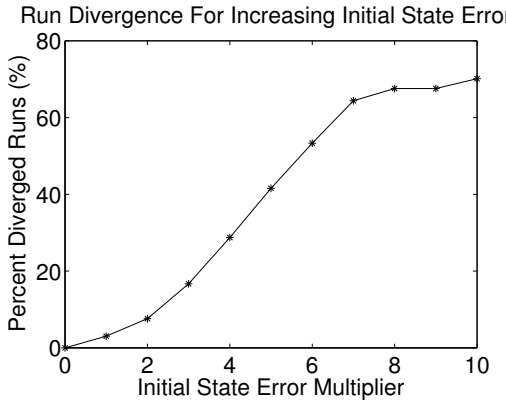

Figure 3.16: Percentage of Diverged Trials For Each Level of Initial State Error and Uncertainty

It is not the intent of this chapter to provide detailed timing comparisons, but some approximate timing values can give the reader a sense of the computational savings achieved by precomputing the process noise before using it in a computationally efficient KF. All code is written in Fortran, using the latest 1995 and 2003 standards, and compiled using standard release mode settings in 2011 Intel Visual Fortran. All simulations are run on a single processor of a quad-core Intel Xeon CPU running at 3.60 GHz. The precomputation of the process noise using the DDT takes approximately 371 seconds (6.2 minutes), while a single trial of the Monte Carlo simulation takes 13

seconds to perform the onboard estimation steps (approximately 3.5% of the process noise precomputation time). To achieve a comparable level of estimation accuracy and covariance realism without precomputing the process noise, a full SKF would be necessary to run onboard the spacecraft, which would take approximately 200 seconds instead of 13 seconds (increasing the required onboard computation by 15x). Note that for higher order gravitational fields, or if other force model parameters are considered, the onboard computational savings increase approximately with $O(N^2)$, where N is the number of state and consider parameters [34].

Note that the filter type used for the process noise precomputation and the onboard filter are interchangeable: it is entirely possible to use other filters such as the UKF or ADF onboard the spacecraft, with no requirement for the type of filter used in the process noise precomputation. The only stipulation is that the onboard filter must be able to use an additive process noise in the propagation of the covariance matrix.

3.5.8 Future Work

Future analysis involving the new precomputed process noise method includes application to other estimation problems that possess mismodeled or unmodeled perturbations, particularly for large, state-dependent perturbations. For the specific problem of spacecraft estimation, the spacecraft mass, area, and reflectivity coefficient could be included as consider parameters when precomputing the process noise, which would better account for SRP and TBP

errors. Another possibility would be to apply this process noise technique to other perturbations that change with time, such as atmospheric drag.

Another possibility for future research is the generation of functions that provide averaged process noise as a function only of the spacecraft radius magnitude, or other temporal/spatial variations. Such functions could prove useful for mission design and analysis of trajectories about small bodies, eliminating the need to recompute the process noise for each reference trajectory.

It is also possible to add multiple traditional process noise components to better tune the filter: for example, different levels of traditional process noise can be added in the along-track and cross-track directions. Alternatively, different levels of traditional process noise can be added based on an exponential model of the radius of the spacecraft position (derived manually instead of the averaged process noise approach from the precomputed process noise proposed above). Both of these approaches involve adding more manual tuning parameters to the process noise method. As a result, obtaining initial tuning parameters can be even more challenging. Thus, a future analysis comparing the multi-parameter traditional process noise model to the precomputed process noise approach is likely valuable, as is a study of how the use of the precomputed process noise approach might assist in initially tuning the multi-parameter traditional process noise model.

Other items for future analysis include: a simplified nonlinear problem that bridges the gap between the linear example provided here and the more realistic nonlinear scenarios; a more thorough investigation of the error

required for the precomputed process noise approach to consistently fail, from more significant deviations in the reference trajectory away from the truth trajectory to timing errors in the pictures (or the complete loss of particular pictures); as well as an analysis of the effectiveness of a bank of different process profiles used for different trajectories (which would include a study of the additional computational resources required).

3.6 Conclusions

The primary contribution of this chapter is an approach that applies known consider covariance analysis tools and filters to precompute a process noise profile along a reference trajectory, and then employ that process noise in an onboard estimation filter. As a result, the need for traditional extensive manual tuning of process noise is greatly reduced, and robotic systems that experience significant state-dependent perturbations can employ appropriate levels of process noise in onboard navigation filters.

In addition to providing better estimation performance, the new process noise method also allows the onboard navigation filter to better represent the uncertainty in the system state. The example considered here is a better representation of the position and velocity uncertainty of a spacecraft during a descent trajectory that contains gravity perturbations that vary dramatically in magnitude across the reference trajectory.

A secondary contribution of this chapter is the translation of the ADF to a consider filter form. The derivation is almost identical to the USKF,

where the considered parameters are added to the "state" and then simply not updated in the measurement update portion of the filter (for both the state and covariance updates).

There are limitations of the new precomputed state-dependent process noise method. A reference trajectory must exist, and the vehicle must not deviate too far from the reference path for the precomputed process noise to be effective. The errors in the considered model parameters must also approximately match the model parameter uncertainties used for the process noise precomputation. However, it is noted through a limited analysis that conservative uncertainties in the process noise precomputation may prove more effective than less conservative uncertainties (particularly if there is risk of underestimating the truth gravity errors). While the new precomputed process noise method is shown to be effective for the two examples described in this chapter, the method may prove less reliable and effective for scenarios that do not meet these conditions.

Chapter 4

Spin State Estimation of Tumbling Small Bodies

It is expected that a non-trivial percentage of small bodies that future missions may visit are in non-principal axis rotation (i.e. "tumbling"). The primary contribution of this chapter[1] is the application of the Extended Kalman Filter (EKF) Simultaneous Localization and Mapping (SLAM) method to estimate the small body spin state, mass, and moments of inertia; the spacecraft position and velocity; and the surface landmark locations. The method uses optical landmark measurements, and an example scenario based on the Rosetta mission is used. The SLAM method proves effective, with order of magnitude decreases in the spacecraft and small body spin state errors after less than a quarter of the comet characterization phase. The SLAM method converges nicely for initial small body angular velocity errors several times larger than the true rates (effectively having no a priori knowledge of the angular velocity). Significant errors in the initial body-fixed landmark positions are effectively es-

[1]The work in this chapter has been published as a journal paper:

- Olson, C., Russell, R., Bhaskaran, S., "Spin State Estimation of Tumbling Small Bodies," The Journal of the Astronautical Sciences, Vol. 63, No. 2, June 2016, pp. 124-157.

The analysis was performed primarily by the first author, with general development guidance and management provided by the co-authors.

timated, but surface landmark generation and identification are not addressed in this chapter (see Chapter 5). The algorithm remains effective for a range of different truth spin states, masses, and center of mass offsets that correspond to expected tumbling small bodies throughout the solar system.

4.1 Introduction

Determining a small body's spin state is one of the primary challenges during the early arrival mission stages. As the Rosetta spacecraft approached Comet 67P/Churyumov–Gerasimenko in the summer of 2014, mission navigators could not be certain the comet was in principal axis rotation, despite estimates provided by Hubble observation campaigns in 2003 [18, 70]. The potential for non-principal axis rotation, also known as "tumbling" or "complex rotation," is based on the current estimate that a significant fraction of small bodies in the solar system are tumbling [97]. Most tumbling bodies are smaller (less than 10 kilometers in diameter) and slow rotators (with rotational period greater than two days), but small fast rotators that are also tumbling have been detected as well [112]. Note that tumbling is not truly chaotic motion, as torque free motion is fully predictable using elliptic integrals [110]. However, torques from forces such as outgassing can alter the motion.

In general it is not possible to know with strong certainty the degree to which a small body is tumbling before arriving at the body, especially for bodies that have not previously had a close approach with the Earth. Fortunately Comet 67P/Churyumov–Gerasimenko was found to be primarily in principal axis rotation (over the time scales needed), and thus the established

tools were sufficient for the navigation task [18]. However, ESA has revealed that the spin rate of Comet 67P/Churyumov–Gerasimenko is slowing down by approximately one second per day due to gas jet activity.[2] Thus, the spin rate must be continually re-calibrated, resulting in increased work for mission operators. The initial uncertainty in the small body spin state and the changing nature of the spin state over time are strong motivators for a navigation framework that can directly and continuously estimate the spin state from landmark observations.

An Extended Kalman Filter (EKF) Simultaneous Localization and Mapping (SLAM) method is employed for this purpose. SLAM is traditionally associated with terrestrial robotics, and most applications of SLAM in the literature use optical and range measurements to estimate the vehicle state and the surrounding static environment [9]. The method proposed in this chapter differs from traditional terrestrial SLAM scenarios by estimating the spin state of a small body using optical landmark observations, and uses an initial spacecraft attitude estimate provided by a separate attitude determination using star trackers and gyros. The method described below also differs from previous applications of SLAM in the field of small body navigation [35, 36] by estimating the spin state of the body simultaneously with the relevant inertial spacecraft states (instead of relative to a particular body-fixed frame on the surface of the body).

[2] `http://aerosociety.com/News/Society-News/2998/Lecture-Report-Rosetta-How-We-Landed-on-a-Comet`

The estimation process occurs during the small body characterization phase, when the spacecraft is many small body radii away from the body. A camera with a narrow field of view and long focal length is used, which makes significant numbers of landmarks identifiable. The optical navigation method using landmarks is well established in the literature [19, 90], and is described in section 1.1. The objective of this chapter is to assess the ability of the established EKF SLAM algorithm to effectively estimate the small body spin state (along with other state parameters), and determine the practical limits of how much initial small body spin state error the algorithm can handle. The spin state of a small body can also be estimated independently with standard batch methods, solving for the pole direction, nutation, precession, and spin as described in the IAU models for planetary body attitude representation [116]. However, these models aren't sufficient for long term motion of small bodies due to the potential for forces that impart torques on the spin of the body, such as out-gassing, solar radiation pressure, and gravity gradient affects if the small body has any planetary flybys.

The estimated states include the inertial spacecraft position and velocity; the small body orientation, angular velocity, mass (GM), and diagonal moments of inertia; and the body-fixed surface landmark positions. These quantities are estimated directly from pixel and line optical measurements of previously identified surface landmarks. An estimate of the spacecraft attitude is provided by an independent onboard attitude determination system (ADS) consisting of gyroscopes, star cameras, and an attitude determination filter. However, the spacecraft attitude can optionally be further corrected using the

optical landmark measurements. Further attitude correction is more important when ADS estimates are degraded (e.g. when no stars are available because the small body fills the field of view of the star cameras). Euler angles are used to represent the spacecraft attitude for ease of implementation (as well as use of heritage algorithms), and Modified Rodrigues Parameters (MRP) are used to represent the orientation of the small body in order to avoid singularities (through the shadow switching method described in Appendix A).

Estimation of a rigid body spin state and moment of inertia ratios using surface landmarks was first considered by Idle [55], as part of an effort to estimate these quantities for a target spacecraft in Earth orbit using images taken from a chaser spacecraft. However, he assumes the inertial locations of surface features are provided at each observation time, which he then processes in a batch least squares algorithm. The sequential SLAM algorithm presented in this chapter here provides a means to not only estimate the spin state and moments of inertia, but also estimate the locations of the landmarks on the surface directly from the pixel and line values of the landmarks within each image.

4.2 Optical Navigation Using Landmarks

The estimation algorithm proposed uses optical measurements, as described in section 1.1. The simulated camera is comparable to the Charge-Coupled Device (CCD) cameras used for navigation in previous small body missions, with a focal length of 140 mm and a sensor array of 1024 by 1024 pixels, for a field-of-view (FOV) of approximately 5 degrees. The results of

this chapter are generally applicable to any CCD with a similar focal length, pixel array size, and FOV; which includes navigation cameras for the Rosetta (focal length of 152 mm) [67], Dawn (focal length of 150 mm) [101], NEAR Shoemaker (focal length of 168 mm) [53], and Hayabusa (focal length of 120 mm) [56].

The simulated camera in this chapter is assumed to be hard-mounted to the spacecraft bus, and the camera frame is aligned with the spacecraft frame for simplicity. Therefore the rotation matrix $\boldsymbol{R_{i2cam}}$ is equal to the rotation matrix $\boldsymbol{R_{i2sc}}$, as defined by

$$\boldsymbol{R_{i2sc}} = \boldsymbol{R_3}(\phi_{sc})\boldsymbol{R_2}(\frac{\pi}{2} - \delta_{sc})\boldsymbol{R_3}(\alpha_{sc}) \tag{4.1}$$

where ϕ_{sc} is the spacecraft twist angle, δ_{sc} is the declination value, and α_{sc} is the right ascension (RA) angle. The declination is subtracted from $\pi/2$ to avoid singularities. $\boldsymbol{R_{i2sc}}$ is computed using the current estimated small body orientation parameters, and the camera boresight is along the spacecraft z-axis.

The simulated camera pixel density terms K_x and K_y from equation 1.5 are set to heritage values of 83.333 [90] and the off-diagonal terms are set to zero. Camera distortion effects on the images that are typically calibrated in flight are not included in the simulations. The observation model described in section 1.1 is used for both the truth and filter measurement models, and the measurement errors are described in the section titled "Monte Carlo Error Parameters".

It is assumed that initial estimates for the states and a (potentially coarse) shape model have been previously determined in the first approach phase using center of brightness observations, and an initial set of landmarks on the surface are identified a priori. The landmark generation and identification problem [8] is not treated in this chapter (see Chapter 5), but the positions of the landmarks contain some initial error that is estimated using the SLAM algorithm. While it is possible to have misidentified landmarks, in practice the misidentification of landmarks has not proven problematic for optical navigation team members at JPL due to the examination of the postfit measurement residuals and subsequent removal of outliers.[3] Should mis-identification of landmarks become an issue in future autonomous navigation systems, current research in the field of multi-target tracking could prove useful [57].

A triaxial ellipsoid is used for the small body shape: while not as representative as a full polyhedron shape model, it is sufficient for the evaluation of the navigation algorithms. Night shading is implemented in the current analysis, but the small body characterization trajectories stay primarily between the Sun and the small body, so landmarks remain visible throughout the simulation.

4.3 Estimation Filter Architecture

A standard discrete EKF, as described by Tapley, et. al. [121], is employed. The following parameters are estimated: the spacecraft position,

[3]Email Communication with Nickolaos Mastrodemos (JPL), July 24, 2015

velocity, and optionally the attitude (for further correction of onboard provided attitude estimates); the small body orientation, angular velocity, GM, and diagonal moments of inertia; and body-fixed locations of surface landmarks considered for navigation. The CM offset and off-diagonal moments of inertia of the small body are not estimated due to lack of observability, but errors are added for these values, as described in Table 4.7 below. Note that in this implementation, the size of the state vector is constant and does not change depending on how many landmarks are visible. These states are simultaneously estimated directly from the landmark observations, and all partial derivatives for the EKF formulation are computed using a standard numerical finite difference approach.

The spacecraft attitude at each picture time is provided independently from a "black-box" ADS consisting of star cameras, gyros, and an attitude estimation filter. It is assumed that the spacecraft is commanded to point its camera at the origin of the body-fixed frame of the small body using onboard position and attitude knowledge at every picture time using control moment gyroscopes (CMG), reaction wheels, or thrusters. Thus the spacecraft attitude is not dynamically propagated, nor are the attitude maneuvers directly simulated. This simplification has been used successfully in previous studies of optical navigation about small bodies [19].

Assuming that the attitude control error is low enough that a sufficient number of landmarks are in the camera FOV, the more important aspect for navigation analysis is the attitude knowledge error of the ADS. The attitude knowledge error is simulated using expected attitude commanding and

knowledge accuracy from modern onboard attitude determination and control systems [71, 76, 1]. It is assumed that stars are available to the star camera in the earlier portions of this mission phase (i.e. the small body does not fill or nearly fill the star camera FOV). Later in the characterization phase only landmarks and gyroscope measurements are available for attitude determination, but the attitude knowledge error remains low based on previous flight experience at small bodies [81].

When only landmarks are available, or if for some reason the independent ADS becomes degraded, the attitude of the spacecraft can be further corrected using the landmark measurements. With nominal performance of the ADS, this correction is typically not needed (and is not included in the nominal results shown below), but can provide a small improvement in the overall performance of the filter. Estimation updates of the spacecraft attitude are isolated to each photo time, and thus no process noise is employed for attitude, and the same a priori covariance is used at each photo time. While an isolated improvement to the spacecraft attitude at one photo time will not improve attitude estimates at other photo times, any improvements made to the other states will carry forward. More precisely it is the camera pointing that is further corrected from the initial ADS estimate, but in this analysis the navigation camera is assumed to be hard-mounted to the spacecraft bus (as has been the case for recent missions), and thus all references to spacecraft attitude estimates are equivalent to camera pointing estimates.

4.4 Monte Carlo Simulation Design

Monte Carlo simulations are used to obtain a statistical assessment of the filter accuracy. Two primary methods to distribute Monte Carlo initial state errors are: 1) adding initial state errors to the nominal state to obtain numerous different truth trajectories, or 2) adding initial state errors to the truth state to obtain different initial nominal states. The advantage of the first method is that it emulates what occurs in flight operations: the truth state is never known (and downstream truth trajectories are dependent on upstream filter estimates due to maneuver planning), so Monte Carlo truths must be distributed about the current best estimate of the state. The advantage of the second method is having a single truth trajectory and set of observations, which can simplify comparison studies. The single truth trajectory method can also eliminate the need to introduce initial state error with a more complex model than a standard Gaussian distribution (i.e. to avoid situations where the truth trajectory intersects the small body).

For this chapter, the second option is chosen: the nominal states are distributed about the truth using the sampled error values. This distribution method includes the spacecraft attitude: the nominal attitude at each picture time is computed by "adding" (in the rotational sense) the attitude knowledge error to the truth pointing vector. As a result, all truth landmark observations are identical between Monte Carlo trials, and all trials are subject to the same environment.

4.5 Maneuvers

Impulsive maneuvers are performed in the simulation as part of the small body characterization mission phase. In general, maneuver execution error (i.e. the difference between the planned maneuver and true executed maneuver) is critical to consider when maneuvering a spacecraft. However, when evaluating navigation and estimation algorithms (as is done in this chapter) the most important error to consider is the knowledge error: the difference between the actual maneuver and the estimated maneuver. As long as the execution error is not so great that the surface landmarks are no longer visible, it is assumed that execution error should not significantly affect the estimation results.

As a result, no execution error is computed, and the waypoints are not re-targeted for each nominal Monte Carlo trial. The truth trajectory remains constant for all Monte Carlo trials, and all truth delta-v's are precomputed for each truth scenario using a standard differential correction method to target the trajectory way-points. For each Monte Carlo trial, maneuver knowledge error is added to the truth delta-v to obtain the nominal delta-v (which is added to the propagated nominal state at the maneuver time), as shown in Figure 4.1. This approach is commonly known as the separation principle: the observer and controller can be designed and implemented separately [79, 30, 20]. While this separation principle is provably true only for linear systems, it has been successfully employed for nonlinear systems such as navigation and mission design analysis, including NASA's Magnetosphere Multiscale (MMS) mission [94].

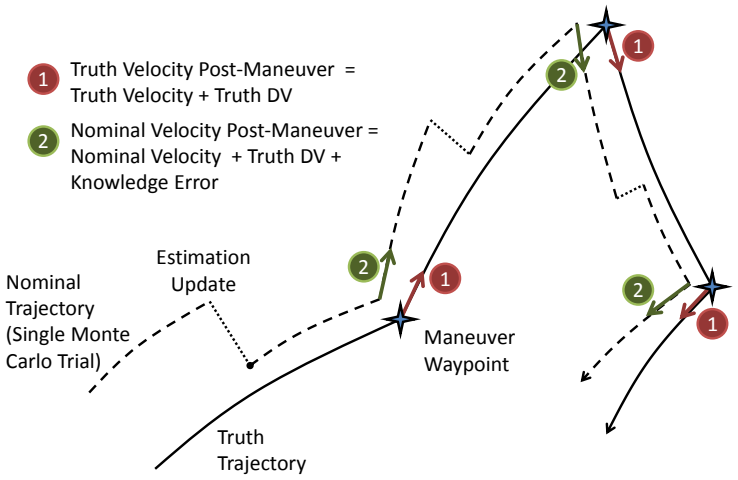

Figure 4.1: Maneuvers with Knowledge Error

The differences between the truth maneuver and the planned maneuvers that would result if each of the 1000 Monte Carlo trials re-targeted waypoint 2 (employing the same differential corrector used for the precomputed truth delta-v) are shown in Figure 4.2 as projected scatter plots. Note that the scatter plot dispersions are near Gaussian. Thus from a statistical point of view, one can make the (admittedly liberal) claim that these "re-target differences" are equivalent to sampled Gaussian execution errors. Therefore, not including execution error and not re-targeting for each Monte Carlo are justified if these two non-actions are performed as a pair. It is emphasized that this approach allows for fast Monte Carlo simulations, as each trial run avoids any maneuver re-targeting and recomputing truth trajectories.

The maneuver knowledge error is computed by sampling Gaussian random variables with conservative user-provided standard deviations, as shown in subsection "Monte Carlo Error Parameters". Typical maneuver execution

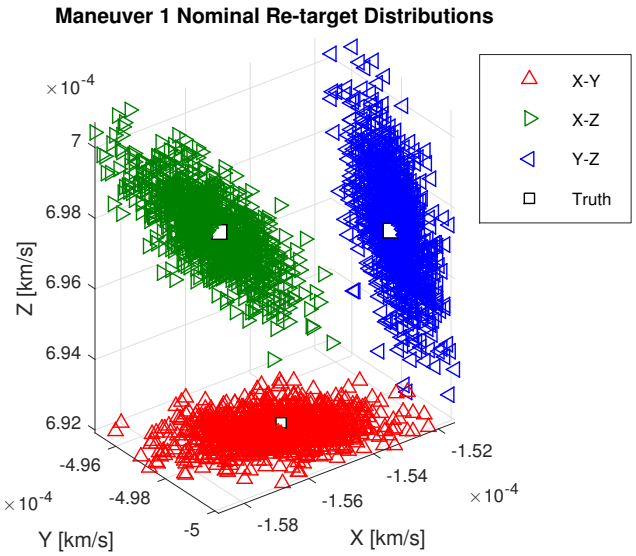

Figure 4.2: Truth Maneuver and Re-targeted Maneuvers from Nominal Monte Carlo Trials, 2D projections

error parameters are used for the knowledge error parameters, which adds another layer of conservatism: usually the post-fit maneuver knowledge error is far less than the maneuver execution error (unless the maneuver estimation process proves totally ineffective). To account for the increase in uncertainty of the velocity at the maneuver time in the estimation filter, the velocity covariance is inflated by the same standard deviation of the random variable used to compute the knowledge error. If the truth scenario is modified, the truth delta-v values are recomputed. As expected, the delta-v values have low sensitivity to changes in the truth small body spin state.

4.6 Dynamical Models

The truth spacecraft dynamical trajectory model includes central body acceleration, perturbations from a spherical harmonic gravity field, solar radiation pressure (SRP), and the third body perturbation (TBP) of the Sun. Accelerations from other bodies are negligible and not included. The nominal spacecraft dynamical trajectory model includes the same accelerations except for the spherical harmonic gravity perturbations, which are completely neglected: at this point in a small body mission, no reliable gravity harmonic coefficient values are available (nor are they observable). Some estimates (with high uncertainty) of the lower order coefficients may be available from shape models (which assume a constant density profile) [133, 134], but these are unnecessary for navigation at the high altitude characterization phase. The gravity field can be further refined once a spin state is established and lower orbits are achieved.

A fourth degree and order spherical harmonic gravity model from the asteroid Eros is used for the truth model, though the GM and reference radius are altered to the current best estimate of Comet 67P/Churyumov–Gerasimenko. The gravity coefficients of Eros are used to emulate the level of perturbations expected at a small body. Table 4.1 lists the magnitudes of the forces acting on the spacecraft when it is furthest and closest to the small body during the simulation. At the maximum position radius the gravity perturbation is weaker than the SRP and TBP forces. At the minimum radius the gravity perturbation is twice as strong as the TBP force, but still an or-

der of magnitude weaker than the SRP. Thus the SRP is the most important spacecraft perturbation force to model.

Table 4.1: Forces On Spacecraft [N]

	Max Radius (115 km)	**Min Radius (54 km)**
Central Body	7.176×10^{-5}	3.255×10^{-4}
Gravity Pert	1.022×10^{-8}	2.424×10^{-7}
SRP	2.325×10^{-6}	2.325×10^{-6}
TBP	2.186×10^{-7}	1.151×10^{-7}

Figure 4.3 illustrates the reference frames used and the other quantities of interest. Note that I and BF indicate the inertial and small-body-fixed reference frames, respectively. The spacecraft position r_{SC-I} is defined in the inertial frame, while the center of mass location r_{CM-BF} and the inertia values (I_{XX-BF}, I_{YY-BF}, and I_{ZZ-BF}) relative to that center of mass location are defined in the body-fixed frame. Note that all forces acting on the spacecraft are computed using the spacecraft location relative to the small body CM (for both the nominal and truth model, though the nominal value has some error which is not estimated or corrected). The CM-relative spacecraft position vector is determined using the CM offset value, rotated from the body-fixed frame to the inertial frame:

$$\boldsymbol{r_{SC-CM}} = \boldsymbol{r_{SC-I}} - \boldsymbol{R_{b2i}}\, \boldsymbol{r_{CM-BF}} \tag{4.2}$$

The small body rotation dynamical model is a numerical integration of Euler's equations for rigid body dynamics. While torque free motion has

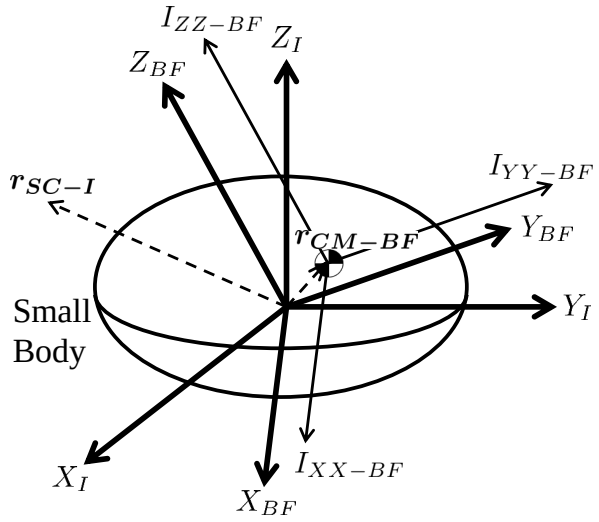

Figure 4.3: Reference Frame Diagram

closed form solutions (in terms of elliptic integrals) [110], numerical integration is performed in order to allow torques from YORP effects, out-gassing effects, and other celestial bodies. Because these torques are expected to be negligible over the time span between measurements [110], they are not included in these simulations. However they can be added as needed for longer propagation times. The small body angular velocity and moments of inertia are expressed within the simulation in the body-fixed frame so that the inertia tensor is constant over the integration time spans. The initial body-fixed angular velocity vector is converted from initial euler angle rates via the Euler angle rates matrix, as described by Diebel [41]. The moments of inertia, which are defined relative to the small body CM and in the small-body-fixed frame, are modified only at the measurement updates.

MRP are used to represent the orientation of the small body, and the time derivative of the MRP representation required for the dynamical model is provided in Appendix A. The user-provided initial 3-1-3 Euler angle values are converted to MRP at the start of the simulation, and the output MRP truth and error values are converted to Euler angles for a more intuitive representation.

The spacecraft and small body dynamics are propagated via numerical integration between picture times using the fixed-step fourth-order Runge-Kutta (RK4) method. RK4 is used to emulate expected onboard integration capabilities [78]. The covariance is propagated to the same times, also using fixed step propagation, by the standard method of integrating the state transition matrix via numerical integration. A step size of approximately one minute is used for the propagation intervals between the four photos taken five minutes apart (as described below in Table 4.2) and a step size of approximately thirty minutes is used for the four hour intervals between the sets of four photos.

4.7 Simulation Scenario

The scenario used to evaluate the SLAM algorithm is based on the comet characterization phase of the Rosetta mission [46, 71], when the spacecraft starts at approximately 115 kilometers from the body, and flies in pyramid-like trajectories between the comet and the Sun [138]. Only a small amount of delta-v is needed to shift between hyperbolic trajectories at these high altitudes, allowing improved viewing geometries for the small body characteri-

zation phase. Eight arcs of the pyramid trajectory are simulated, which are displayed in the three dimensional plot and the set of two dimensional projections in Figure 4.4. The arcs are shown in a Sun-Fixed frame only for visualization, whereas the dynamics are integrated in the inertial frame.

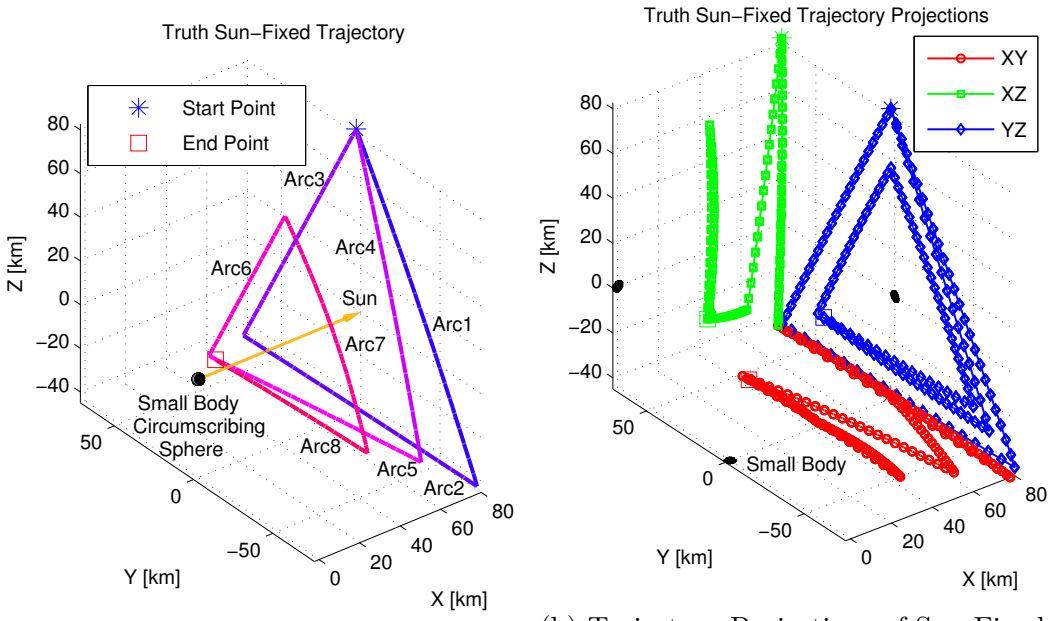

(a) Truth Sun-Fixed Trajectory

(b) Trajectory Projections of Sun-Fixed Trajectory

Figure 4.4: Truth Trajectory

Two primary truth small body tumbling scenarios are investigated in this chapter: minimal tumbling (i.e. primarily principal axis rotation with small amounts of precession and nutation), and nominal tumbling (i.e. the angular velocity is not closely aligned with the small body's maximum principal axis of rotation). The minimal tumbling scenario has initial Euler angle rates of 10 degrees per day for the Right Ascension (RA), 20 degrees per day for the declination (Dec), and 696 degrees per day for the Prime Meridian (PM), or

"twist", which are converted to body-fixed angular velocity at the beginning of the simulation. The nominal tumbling has initial Euler angle rates of 450, 450, and 350 degrees per day for the RA, Dec, and PM, respectively. The truth small body orientation and body-fixed angular velocity components for both scenarios are displayed in Figures 4.5 and 4.6.

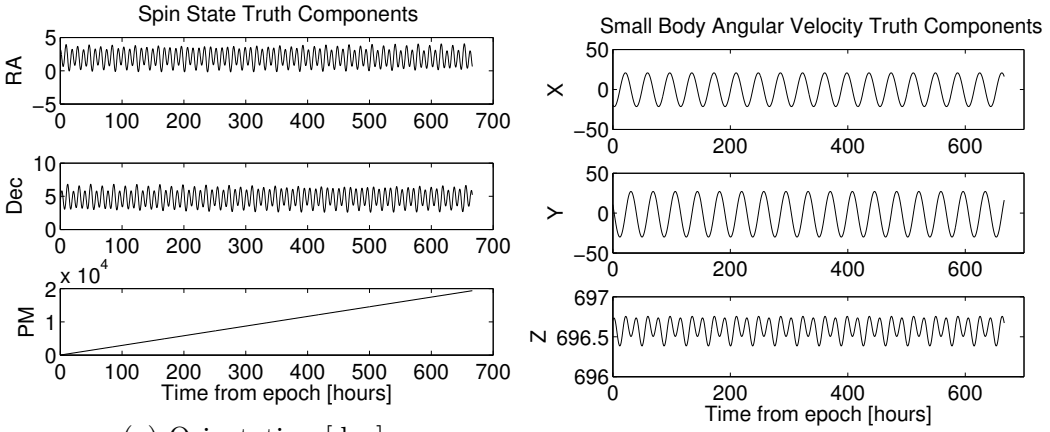

(a) Orientation [deg],
$\boldsymbol{R_{i2b}} = \boldsymbol{R_3}(\mathrm{PM})\boldsymbol{R_1}(\frac{\pi}{2} - \mathrm{Dec})\boldsymbol{R_3}(\mathrm{RA})$

(b) Angular Velocity [deg/day]

Figure 4.5: Minimal Tumbling Small Body Spin State Over Time

Thirty predetermined and randomly located landmarks are provided for navigation from the initial approach phase. This number of landmarks is consistent with the number that are expected at this mission stage if manual methods are used [27], with greater amounts likely if computer vision techniques are used. Including more than thirty landmarks in the simulation does not significantly enhance the estimation of the small body spin state in this scenario, and computation increases significantly with increasing state size.

Typically a coarse estimate of the spin state of the small body is needed before the process of computing stereophotoclinometry (SPC) landmarks can

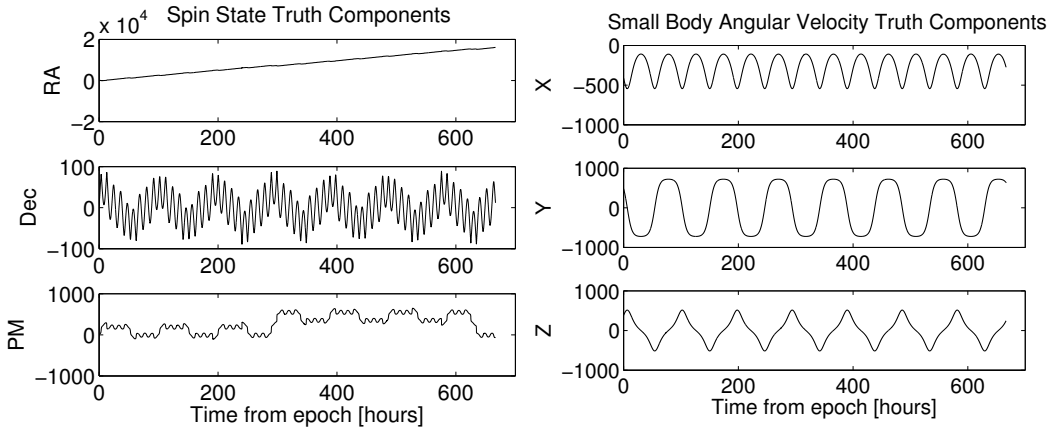

(a) Orientation [deg],
$\boldsymbol{R_{i2b}} = \boldsymbol{R_3}(\mathrm{PM})\boldsymbol{R_1}(\frac{\pi}{2} - \mathrm{Dec})\boldsymbol{R_3}(\mathrm{RA})$

(b) Angular Velocity [deg/day]

Figure 4.6: Nominal Tumbling Small Body Spin State Over Time

be started, which has not been a problem for bodies in principal axis rotation [18]. For a body that is strongly tumbling, mission navigators may need to manually determine and locate natural feature landmarks, or use standard computer vision techniques such as SIFT or SURF. As the small body spin state is better determined, SPC landmarks can be generated and these can be used instead of manual or other less accurate computer vision options [44]. Because manually selected natural feature landmarks have greater initial position error and possibly greater measurement error than the SPC method, the spin state estimation performance is evaluated for a range of initial landmark position errors and measurement errors, including errors well above expected worst-case values for manually-selected landmarks.

Various timing parameters of the simulation are listed in Table 4.2, including the maneuver times. The truth maneuvers, which range in magnitude

from 0.87 m/s to 0.58 m/s, are displayed in Table 4.3 below. See Tables 4.4 and 4.5 for small body and spacecraft parameters, respectively.

Table 4.2: Simulation Timing

Simulation Parameter	**Values**
Epoch Time	06-Aug-2014 12:00:00.00
End Time	03-Sep-2014 06:40:00.00
Maneuver #1	10-Aug-2014 11:33:20.00
Maneuver #2	13-Aug-2014 10:40:00.00
Maneuver #3	17-Aug-2014 10:13:20.00
Maneuver #4	20-Aug-2014 09:20:00.00
Maneuver #5	24-Aug-2014 08:53:20.00
Maneuver #6	27-Aug-2014 08:00:00.00
Maneuver #7	31-Aug-2014 07:33:20.00
Minimum Time Before First Update	1 minute after epoch
Measurement Timing	4 photos 5 minutes apart, every 4 hours

Table 4.3: Simulation Maneuvers

Maneuver Count	**Delta-V Vector [km/s]**
#1	$[-1.5511\times10^{-4}, -4.9783\times10^{-4}, 6.9638\times10^{-4}]$
#2	$[-4.8853\times10^{-4}, 1.6001\times10^{-4}, -6.9008\times10^{-4}]$
#3	$[7.1944\times10^{-4}, 3.8504\times10^{-4}, -1.63590\times10^{-5}]$
#4	$[-2.9441\times10^{-4}, -4.4434\times10^{-4}, 4.7151\times10^{-4}]$
#5	$[-3.4777\times10^{-4}, -2.7907\times10^{-6}, -4.6962\times10^{-4}]$
#6	$[5.2675\times10^{-4}, 1.7877\times10^{-4}, 4.8241\times10^{-6}]$
#7	$[-8.6991\times10^{-5}, -3.4001\times10^{-4}, 4.3964\times10^{-4}]$

4.7.1 Filter Parameters

The filter parameters used in the EKF are listed in Table 4.6. The measurement noise covariance 1-σ values are slightly higher than the measurement error 1-σ values of 0.5 pixels, as this measurement underweighting

Table 4.4: Small Body Properties

Simulation Parameter	**Truth Values**
Initial Pole Right Ascension	3 deg
Initial Pole Right Ascension Rate	450 deg/day
Initial Pole Declination	4 deg
Initial Pole Declination Rate	450 deg/day
Longitude of the Prime Meridian at Epoch	5 deg
Rotation Rate	350 deg/day
GM	6.6692×10^{-7} km^3/s^2
CM Offset X, Y, Z	[0.01, 0.02, 0.03] km
Reference Radius for Gravitational Harmonics	2.375 km
Max Radius	2.375 km
Intermediate Radius	1.885 km
Min Radius	1.470 km
Min Moment of Inertia (I_{xx})	1.38176×10^{13} km^2-kg
Intermediate Moment of Inertia (I_{yy})	1.88645×10^{13} km^2-kg
Max Moment of Inertia (I_{zz})	2.22309×10^{13} km^2-kg
Off-Diagonal Moments (I_{xy}, I_{xz}, I_{yz})	-9.99305×10^{8} km^2-kg
Number of Landmarks on surface	30
Degree and Order of Gravity Harmonics	4 (Eros Values Used)

Table 4.5: Spacecraft Properties

Simulation Parameter	**Truth Values**
Mass	1422 kg
Area	6 m^2
Reflectivity Coefficient	1.1
Initial Position (Inertial)	[-47.417, -98.777, -34.924] km
Initial Velocity (Inertial)	[2.8411×10^{-4}, 2.3799×10^{-4}, -2.0866×10^{-4}] km/s

consistently produces slightly better results. It has been shown in the literature that measurement underweighting often produces lower navigation errors [145, 12]. Higher measurement noise covariance values also compensate for the

spacecraft attitude errors applied at each photo time (described in Table 4.7), which are not estimated nominally.

To prevent the position uncertainty from locking down too quickly, which can cause issues with the estimation of other parameters, a small amount of additional process noise (100 square meters) is added to the prefit position uncertainty at the second picture time. This "damping" of the covariance reduction allows a smooth transition from the larger initial corrections of the state estimates to the steady state behavior. The "Velocity Covariance Inflation For Maneuvers" value listed in Table 4.6 is added directly to each of the spacecraft velocity covariance diagonal values after the covariance matrix is mapped from the previous estimation time to the maneuver time.

The process noise for the spacecraft position and velocity is computed using the standard time-difference approach described by equation 3.6 (and provided in Appendix F of Tapley [121]). The tuning parameter q for this process noise model is provided in Table 4.6. The process noise values for the small body orientation (which does not have units, because the MRP representation is unitless) and angular velocity are added directly to the mapped covariance diagonal terms at the end of the longer propagation intervals between the four photos grouped together. No process noise is used for the small body GM or moments of inertia.

4.7.2 Monte Carlo Error Parameters

The 1-σ simulation error parameters sampled in the Monte Carlo simulations are listed in Table 4.7. The errors for the spacecraft position and veloc-

Table 4.6: Filter Parameters

Simulation Parameter	**Values**
Initial Filter Position Covariance (1-σ)	[1, 1, 10] km
Initial Filter Velocity Covariance (1-σ)	[1x10^{-5}, 1x10^{-5}, 1x10^{-5}] km/s
Initial Filter Small Body Spin State Angles Covariance (1-σ)	[5, 5, 5] deg
Initial Filter Small Body Spin State Angular Velocity Covariance (1-σ)	[10, 10, 10] deg/day
Initial Filter Small Body GM Covariance (1-σ)	1.4x10^{-7} km^3/s^2
Initial Filter Small Body Diagonal Moments of Inertia Covariance (1-σ)	[3x10^{11}, 3x10^{11}, 3x10^{11}] km^2-kg
Initial Filter Small Body Landmark Position Covariance (1-σ)	[0.01, 0.01, 0.01] km
Measurement Noise Covariance (1-σ)	[2, 2] pixels
Process Noise q for Position and Velocity	1x10^{-16} km^2/s^3
Process Noise for Spin State Orientation (MRP)	1x10^{-6}
Process Noise for Spin State Angular Velocity	1x10^{-12} (deg/day)^2
Velocity Covariance Inflation For Maneuvers	4x10^{-10} (km/s)^2

ity are provided in the View 2 frame: the first axis is along the velocity vector, the second axis is perpendicular to the orbital plane, and the third axis is perpendicular to the first and second, in general pointing approximately zenith. This frame is chosen based on how missions have historically broken down the expected navigation performance errors. The initial filter covariance values for the position and velocity are given in the same reference frame. The initial

spacecraft state errors are approximately equal to those expected from optical navigation using center of brightness measurements in the approach phase (which occurs immediately prior to the small body characterization phase) [18, 81]. Center of brightness measurements are not significantly dependent on the small body spin state or landmarks (which have not yet been obtained).

The initial small body orientation and spin rate errors are provided in Euler angles and Euler angle rates, which are converted to Modified Rodrigues Parameters errors and body-fixed angular velocity errors using first order partial derivative matrices. The same conversion process is performed for the initial filter covariance values. Modern image processing capabilities can generate landmark center values at sub-pixel precision, and thus 0.5 pixels is used for the measurement error covariance.

The 1-σ maneuver knowledge error parameters are defined in terms of magnitude and direction. The truth maneuver is converted from Cartesian coordinates to spherical coordinates: magnitude, RA and Dec. The magnitude 1-σ error value is 1% of the truth maneuver magnitude. No fixed magnitude error is assumed. The direction error values are one degree (1-σ) for both the RA and Dec. After knowledge errors are added to the truth spherical coordinates, the values are converted to Cartesian coordinates to compute the nominal "estimated" maneuver. The declination value for each maneuver is checked to ensure it is not close to the singularity. These knowledge error values are considered strongly conservative even for execution error, which is likely to be far greater than knowledge error. A less conservative model would involve using knowledge errors previously determined for the mission,

Table 4.7: 1-σ Monte Carlo Error Parameters

Simulation Parameter	**1-σ Error Values**
Spacecraft Mass	20 kg
Spacecraft Area	1 m^2
Spacecraft Initial Position	[1, 1, 10] km
Spacecraft Initial Velocity	[1x10^{-5},1x10^{-5},1x10^{-5}] km/s
Spacecraft Attitude (at each photo)	[0.005, 0.005, 0.005] deg
Small Body Initial Orientation	[5, 5, 5] deg
Small Body Initial Angular Velocity	[10, 10, 10] deg/day
Small Body Initial GM	1.4x10^{-7} km^3/s^2
Small Body Initial CM offset	[0.01, 0.01, 0.01] km
Small Body Initial Diagonal Moments of Inertia	[3x10^{11}, 3x10^{11}, 3x10^{11}] km^2-kg
Small Body Initial Off-Diagonal Moments of Inertia	[1x10^9, 1x10^9, 1x10^9] km^2-kg
Small Body Initial Landmark Locations	[0.01, 0.01, 0.01] km
Observation	[0.5, 0.5] pixel
Maneuver Magnitude	1%
Maneuver Direction	1° Right Ascension, 1° Declination

and would likely use a more complete Gates maneuver error model, which involves direct and proportional terms for the magnitude and direction errors [45].

4.8 Results

A Monte Carlo analysis using one thousand trials is employed to verify the performance of the SLAM estimation algorithm for both truth tumbling scenarios. The number of Monte Carlo trials was increased until the ensemble error statistics converged, which are shown in the captions of the figures below.

The minimal tumbling simulation takes approximately 2.27 CPU hours, with an average of approximately 8.2 CPU seconds per trial. The nominal tumbling simulation takes approximately 5.48 CPU hours, for an average of 19.7 CPU seconds per trial. The nominal scenario is clearly more computationally intensive, due to the propagation required for the complex rotation of the body and the more challenging estimation of the body. These are the CPU run times of sequentially run simulations on a quad-core 3.60 GHz Intel Xeon CPU, with all code written in 1995 and 2003 Fortran and compiled using standard release mode settings in 2011 Intel Visual Fortran.

Figures 4.7 through 4.9 display the post-fit state errors and covariance of the nominal tumbling Monte Carlo simulation. The position and velocity initial errors rapidly converge to near steady state levels within two to three picture times, with order of magnitude reductions in the error within one to two arcs of the comet characterization trajectory. The error introduced to the velocity at each maneuver time is quickly reduced by more than an order of magnitude after the maneuver, and the added error does not significantly disrupt the estimation of the other states. The small body orientation and angular velocity error also rapidly converge, with order of magnitude error reductions within a single arc of the eight hyperbolic arc trajectory. The GM takes longer to converge, but does prove observable. When either the small body CM offset or off-diagonal moments of inertia are included in the estimation state, there is no significant change in error or covariance of any of the states, confirming these quantities are not significantly observable.

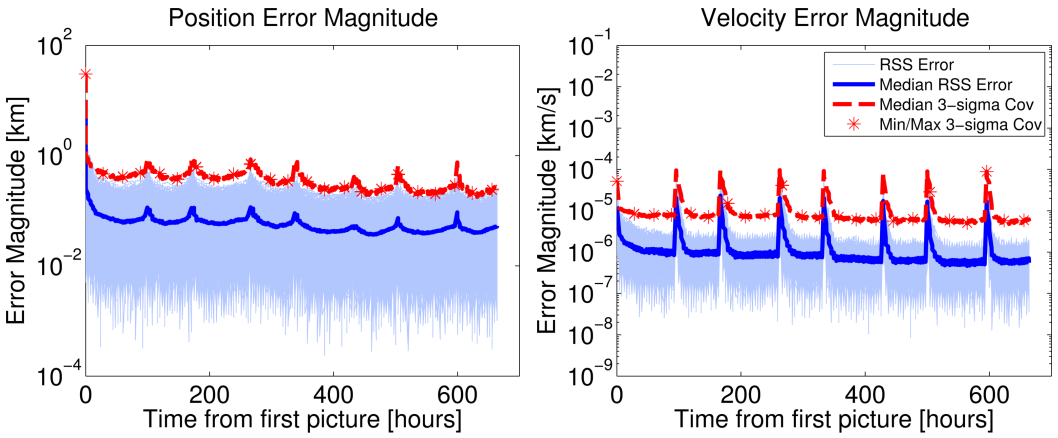

(a) Position
RMS: 0.4034, Max: 28.6948,
Steady State: 0.0815 km

(b) Velocity
RMS: 4.5098E-6, Max: 6.2867E-5,
Steady State: 4.9809E-7 km/s

Figure 4.7: Spacecraft Position and Velocity Postfit Error, Nominal Scenario

The post-fit state error plots are very similar for the minimal tumbling scenario. One exception are the diagonal moments of inertia, which are displayed in Figure 4.9. The scenario with greater amounts of tumbling has greater observability of the primary moments of inertia, and thus faster initial error reduction. There is not significant observability of the off-diagonal moments of inertia for either scenario.

The number of visible landmarks at each photo time shown in Figure 4.10 for the nominal tumbling scenario is identical for all trials (as described in section "Monte Carlo Simulation Design" above). The landmark body-fixed position errors for a single trial are representative of the performance observed in the other trials, and converge rapidly.

Overall, the results for both scenarios show strong convergence and observability of all estimated states except for the diagonal moments of iner-

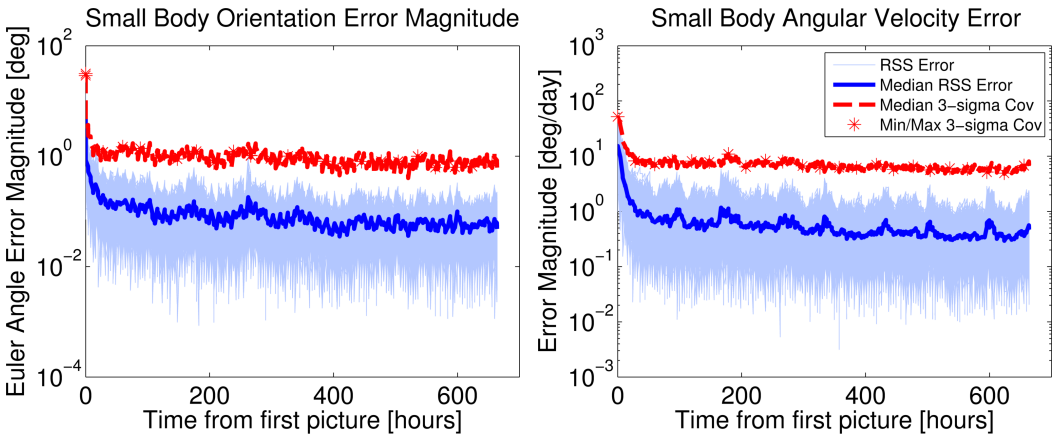

(a) Spin State Attitude
RMS: 0.3810, Max: 21.1866,
Steady State: 0.0870 deg

(b) Spin State Angular Velocity
RMS: 1.8713, Max: 42.2692,
Steady State: 0.6625 deg/day

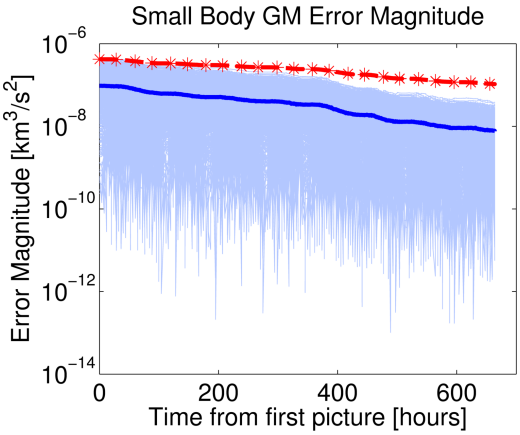

(c) Small Body GM
RMS: 6.6139E-8, Max: 4.4765E-7
km^3/s^2

Figure 4.8: Small Body Spin State and GM Postfit Errors, Nominal Scenario

tia, which exhibit weaker (though non-negligible) observability as expected. Most importantly, the small body spin state values quickly converge to the truth values, for both tumbling body scenarios. The covariance values conservatively well represent the uncertainty in the state, as the error plots are

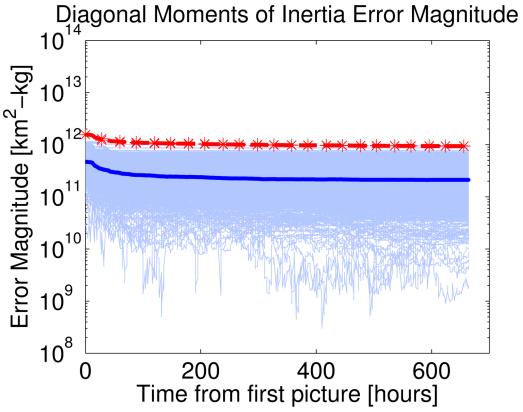

(a) Minimal Tumbling Diagonal Moments of Inertia
RMS: 3.1789E+11, Max: 1.1688E+12 km^2-kg

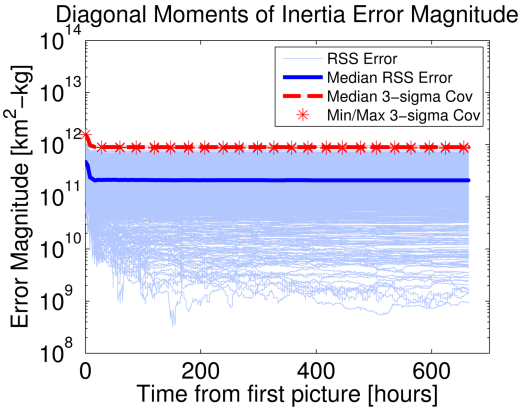

(b) Nominal Tumbling Diagonal Moments of Inertia
RMS: 2.9828E+11, Max: 1.1663E+12 km^2-kg

Figure 4.9: Small Body Diagonal Moment of Inertia Postfit Errors, Nominal And Minimal Tumbling Scenarios

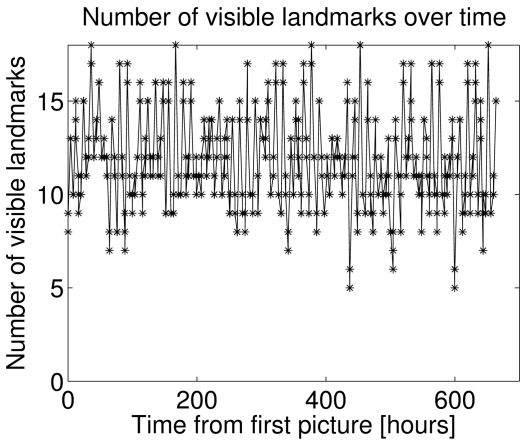

(a) Number of Visible Landmarks, All Trials

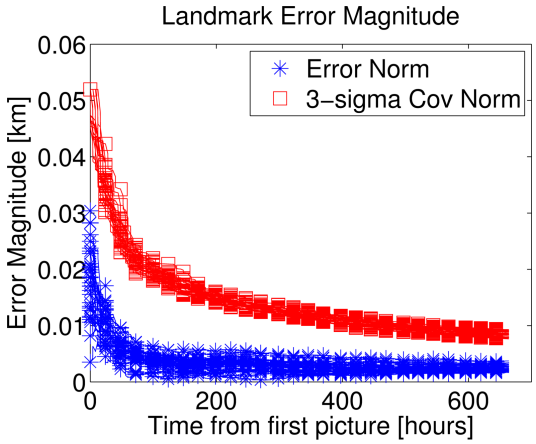

(b) Landmark Position Postfit Errors, Single Trial

Figure 4.10: Landmarks

entirely contained within the 3-σ covariance magnitudes. The postfit residuals are scattered evenly about zero, indicating no systematic biases, with an RMS

of approximately 0.78 pixels. This RMS value is consistent with the Rosetta navigation results presented by Bhaskaran [18]. Using 2 pixels (1-σ) for the measurement noise covariance produces slightly better results than using 0.5 pixels (1-σ) to match the 0.5 pixels observation error, but is not critical for successful convergence of the state parameters.

Based on the error statistics displayed in Table 4.8, the estimated parameters most sensitive to changes in the level of truth tumbling are the spin state angular velocity and the diagonal moments of inertia (and to a limited extent the spacecraft velocity). These results are logical: greater non-principal axis rotation rates make estimation of the angular velocity more challenging, and provide more observability of the moments of inertia.

Table 4.8: Ensemble Error RMS Values For Two Tumbling Scenarios

	Minimal Tumbling (10, 20, 696)* deg/day	**Nominal Tumbling (450, 450, 350)* deg/day**
Position [km]	0.4039	0.4034
Velocity [km/s]	4.3823×10^{-6}	4.5098×10^{-6}
Spin State Orientation [deg]	0.3822	0.3810
Spin State Angular Velocity [deg/day]	1.6552	1.8713
Small Body GM [km^3/s^2]	6.6865×10^{-8}	6.6139×10^{-8}
Diagonal Moments of Inertia [km^2-kg]	3.1789×10^{11}	2.9828×10^{11}

* Initial Euler angle rates (RA, Dec, PM), which are converted to body-fixed angular velocity

The attitude of the spacecraft can be further corrected at each photo time by adding it to the estimation state and using the same non-zero a priori attitude covariance at every photo time. A priori covariance values are chosen to match the Monte Carlo error distribution provided in Table 2.5, and the measurement noise covariance is reduced from 2 pixels to 1 pixel (removing the inflation to better account for non-estimated attitude errors). Errors in the attitude and other states are improved by further correcting the attitude, as seen in Table 4.9. In addition to attitude, velocity and GM errors are significantly improved, while other states are only very slightly improved or not affected.

Table 4.9: Estimation Improvements with Spacecraft Attitude Estimation Enabled

	Minimal Tumbling Scenario	**Nominal Tumbling Scenario**
Position	0.20%	0.22%
Velocity	16.24%	19.13%
Attitude	19.13%	19.13%
Spin State Orientation	0.55%	0.55%
Spin State Angular Velocity	1.66%	1.64%
Small Body GM	4.72%	4.84%
Diagonal Moments of Inertia	2.45%	-0.73%

4.8.1 Varying Initial Spin State Error

To investigate SLAM algorithm performance for different levels of initial spin state error, the 1-σ nominal error and covariance values are determinis-

tically varied for all three components of the initial orientation and angular velocity, and 100 nominal Monte Carlo trials are run for each level of initial error. The "steady state" (i.e. the time period following the first two hyperbolic arcs) error RMS and number of diverged trials for both tumbling scenarios are shown in Figures 4.11 and 4.12.

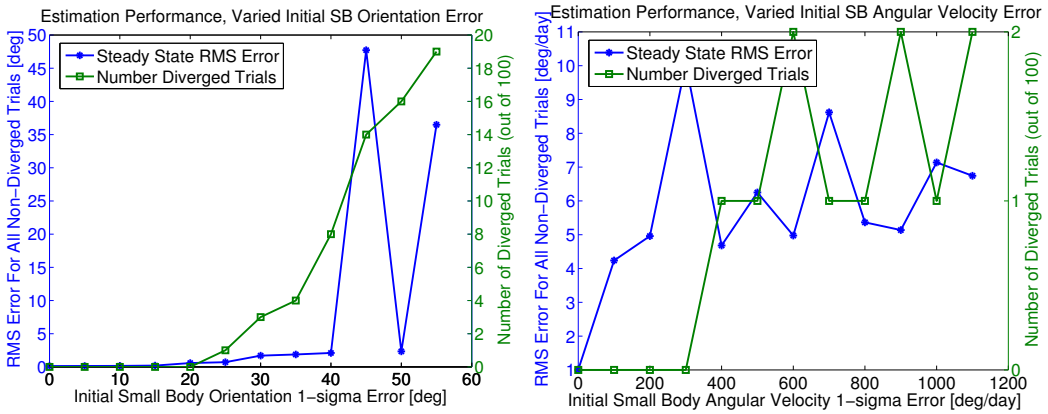

(a) Varied Initial Small Body Orientation Error

(b) Varied Initial Small Body Angular Velocity Error

Figure 4.11: Steady State Error RMS of Small Body Orientation and Angular Velocity, and Number of Diverged Trials, for Different Initial Small Body Spin State 1-σ Errors, Minimal Truth Tumbling Scenario

For the minimal truth tumbling scenario, the increase in the orientation steady state error RMS is very gradual until it reaches 45 degrees 1-σ error, at which point the error RMS spikes (Figure 4.11a). The number of trials that diverge (out of 100) is zero below 25 degrees of initial 1-σ orientation error, and increases significantly above that level of initial error. The error RMS plotted is for non-diverged trials only, so as more of the highest error trials are excluded, the error RMS of the remaining trials can improve. An example of this affect is the drop in error RMS at 50 degrees 1-σ initial orientation error.

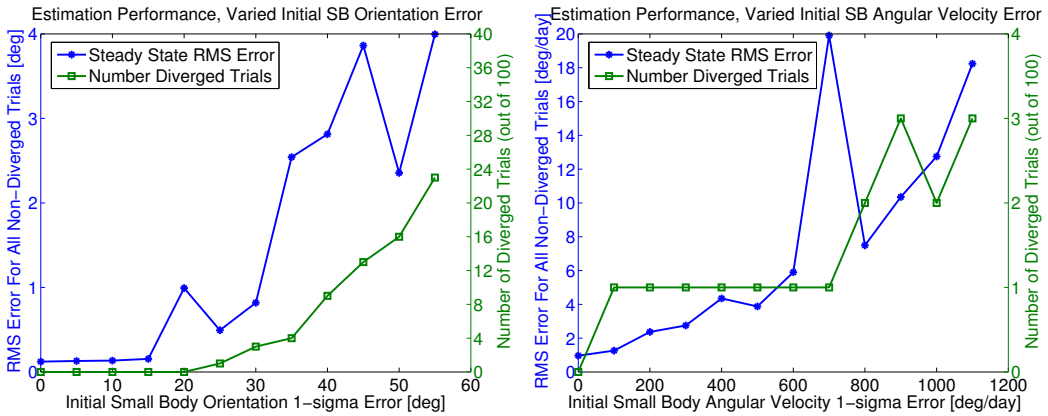

(a) Varied Initial Small Body Orientation Error

(b) Varied Initial Small Body Angular Velocity Error

Figure 4.12: Steady State Error RMS of Small Body Orientation and Angular Velocity, and Number of Diverged Trials, for Different Initial Small Body Spin State 1-σ Errors, Nominal Truth Tumbling Scenario

The angular velocity steady state error RMS and number of diverged trials are low for the range of initial 1-σ angular velocity errors evaluated. Initial error greater than this range exceeds maximum angular velocity magnitudes for many small bodies, beyond which they start to break apart. Thus, the initial values for angular velocity of the body can have high uncertainty (with errors greater in magnitude than the angular velocity values themselves) and the EKF-SLAM filter will still converge on the correct angular velocity. The overall effectiveness of the filter is significantly less sensitive to increases in the initial small body angular velocity error than increases in the small body attitude error.

4.8.2 Varying Initial Landmark Position Error

The SLAM algorithm performance is also evaluated for a range of initial landmark position errors. When the process of estimating the small body spin state begins, the landmarks may be manually identified and assigned body-fixed positions [44, 27], which will likely have significantly larger initial body-fixed position errors than those landmarks later constructed using the SPC method (which requires a strong estimate of the spin state). Thus, it is important to characterize how the spin state can be effectively estimated in the presence of larger initial landmark position errors.

The 1-σ nominal initial landmark position error and covariance values are deterministically increased by 10 meters from 0 meters to 110 meters for all three components, and 100 nominal Monte Carlo trials are run for each level of initial error. The high end of this range is based on minimum levels of surface knowledge described in Castellini [27]. The maximum 1-σ RSS initial error is $\sqrt{110^2 + 110^2 + 110^2} \approx 191$ meters ($\sim 10\%$ of the average body radius). Figure 4.13 reveals that spin state parameters are successfully estimated for the entire range of initial landmark position error. The landmark error smoothly converges for all initial landmark position errors evaluated, and there are no diverged runs. The 1-σ initial landmark errors must be increased to somewhere between 50% and 100% of the body minimum radius (1.470 km) for any runs to diverge, well beyond expected initial landmark position error using manual methods [27].

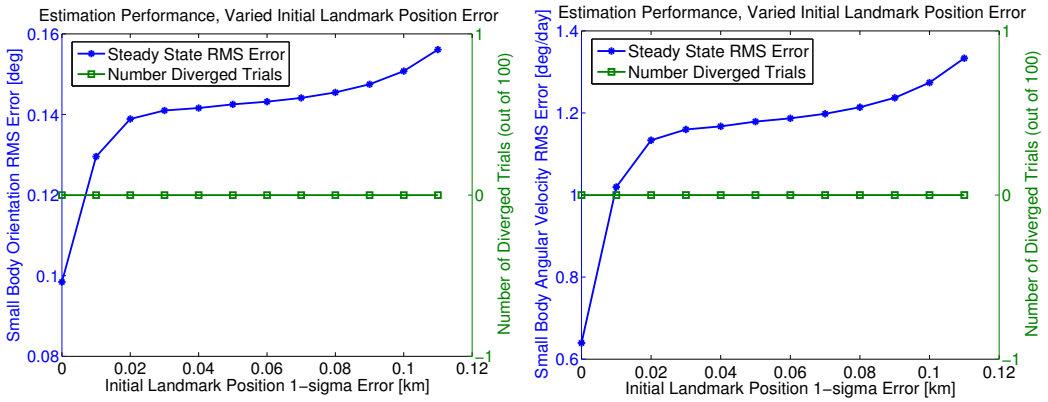

(a) Small Body Orientation Error

(b) Small Body Angular Velocity Error

Figure 4.13: Error RMS of Small Body Orientation and Angular Velocity, and Number of Diverged Trials, for Different Initial Landmark Position 1-σ Errors, Nominal Truth Tumbling Scenario

4.8.3 Varying Landmark Measurement Error

To determine how spin state estimation degrades with increasing landmark measurement error, the 1-σ landmark measurement errors are deterministically increased by 0.5 pixels from 0 pixels to 5.5 pixels for both x and y components, and 100 nominal Monte Carlo trials are run for each level of measurement error. The 1-σ measurement covariance values are set 0.5 pixels greater than the 1-σ measurement error values, to consistently underweight the measurements for each scenario. The resulting "steady state" small body orientation and angular velocity error RMS in Figure 4.14 reveals no drastic degradation of the spin state estimation for any landmark measurement error evaluated. The 1-σ landmark measurement errors must be increased to 10% to 20% of the sensor array size (1024 pixels) for any runs to diverge, well beyond worst-case expected measurement error using manual methods.

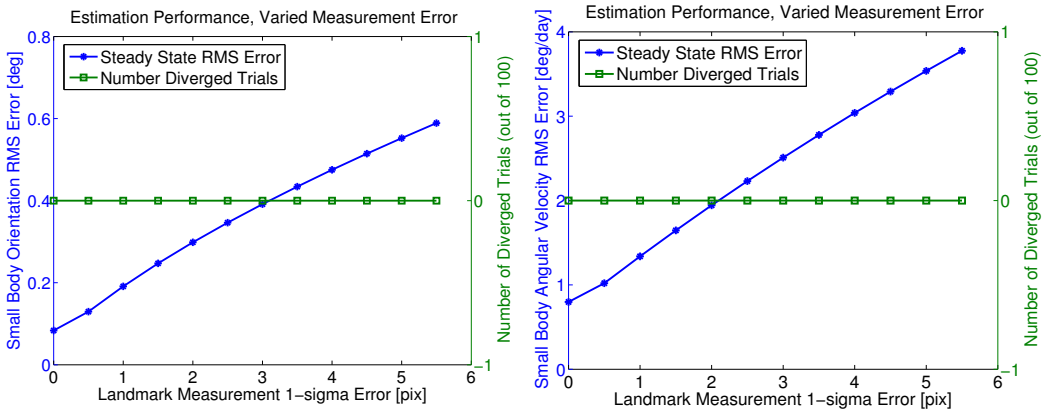

(a) Small Body Orientation Error

(b) Small Body Angular Velocity Error

Figure 4.14: Error RMS of Small Body Orientation and Angular Velocity, and Number of Diverged Trials, for Different Landmark Measurement 1-σ Errors, Nominal Truth Tumbling Scenario

4.8.4 Varying Attitude Error

Spacecraft attitude errors can also affect the performance of the spin state estimation. Further correction of the attitude estimates output by the "black-box" ADS are enabled, and the ADS attitude errors are increased deterministically (corresponding to degraded performance). The steady state small body orientation and angular velocity errors increase smoothly for increasing spacecraft attitude error (which is applied at each picture time), and no simulations evaluated in the range shown in Figure 4.15 have any diverged runs. Estimation of the spin state begins to break down between 1 and 2 degrees of 1-σ attitude error applied at each picture time, which is far greater than levels of error typically present in modern spacecraft attitude determination systems. Errors as large as 1 to 2 degrees 1-σ also begin to approach and exceed the 3 to 5 degree rotation that will place the small body entirely outside of the field of view.

These errors are applied at every picture time, whereas it is likely the ADS will converge on much lower error noise levels, even if starting from larger initial attitude error. The attitude error added in this simulation acts to represent the steady state attitude error, versus initial attitude error, which might be larger if the attitude determination system experiences a temporary disruption. In the event of a total attitude determination system failure, it is likely that the filter will need to iterate further on the attitude at each picture time. Investigation of heavily degraded or failed external attitude estimation capabilities is planned for future work.

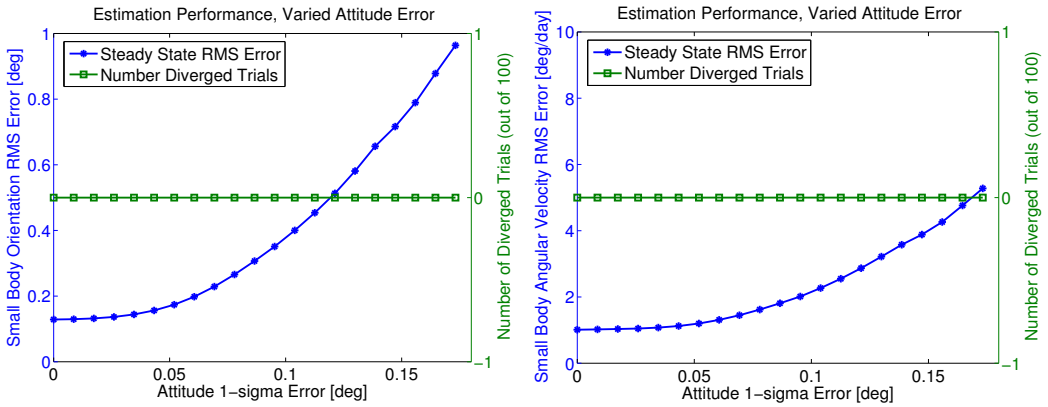

(a) Small Body Orientation Error (b) Small Body Angular Velocity Error

Figure 4.15: Error RMS of Small Body Orientation and Angular Velocity, and Number of Diverged Trials, for Different Attitude 1-σ Errors, Nominal Truth Tumbling Scenario

4.8.5 Varying Initial Spacecraft Position Error

Initial spacecraft position errors up to 50 kilometers 1-σ appear to provide consistent steady state accuracy for the estimation of the spin state,

beyond which the number of diverged trials becomes non-zero and the error RMS increases significantly (Figure 4.16). This level of initial spacecraft position error relative to the small body is significantly larger than is expected from center of brightness optical navigation [18, 81].

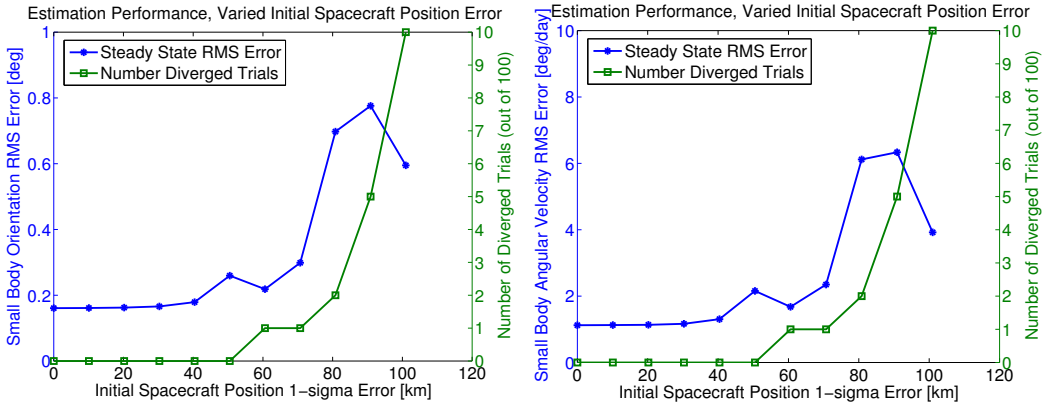

(a) Small Body Orientation Error (b) Small Body Angular Velocity Error

Figure 4.16: Error RMS of Small Body Orientation and Angular Velocity, and Number of Diverged Trials, for Different Initial Spacecraft Position 1-σ Errors, Nominal Truth Tumbling Scenario

4.8.6 Varying Truth Spin State, GM, and CM Offset

The small body spin state and other states are estimated for 1000 different truth small bodies, which are generated by varying the truth small body initial angular velocity, GM, and CM offset using uniform random variables as described in Table 4.10. The limits of these uniform random variables are based on the profiles of the small bodies throughout the solar system that are believed to tumble [110]. For each truth scenario, ten nominal Monte Carlo trials are executed. The error RMS of these ten nominal Monte Carlo trials

Table 4.10: Truth Variation Parameters

Truth Parameter	**Uniform Random Variable Range**
Small Body Initial Angular Velocity (each component)	[-700, 700] deg/day
Small Body GM	[3.0x10^{-7}, 5.6x10^{-6}] km^3/s^2
Small Body CM offset	[-0.1, 0.1] km

for each truth trial is displayed via histograms in Figures 4.17 and 4.18, for the position, velocity, small body orientation, and angular velocity.

The histogram plots exhibit near-Gaussian distributions, with a few minor outliers occurring for the spacecraft position and small body angular velocity (which do not appear to be correlated with each other). Based on these results, the SLAM algorithm appears to have no problems estimating the states (besides those states that are established to have lower observability) for the range of mass and spin state values expected for tumbling small bodies [110].

4.8.7 Observability Analysis

Besides adding or removing a particular quantity to the estimation state to determine the impact it has on the results (which was used to detect the unobservability of the small body center of mass offset and off-diagonal moments of inertia), there are other methods for investigating observability, including an analysis of the Observability Matrix. An Observability Matrix analysis can also provide the different levels of observability of the different estimated states.

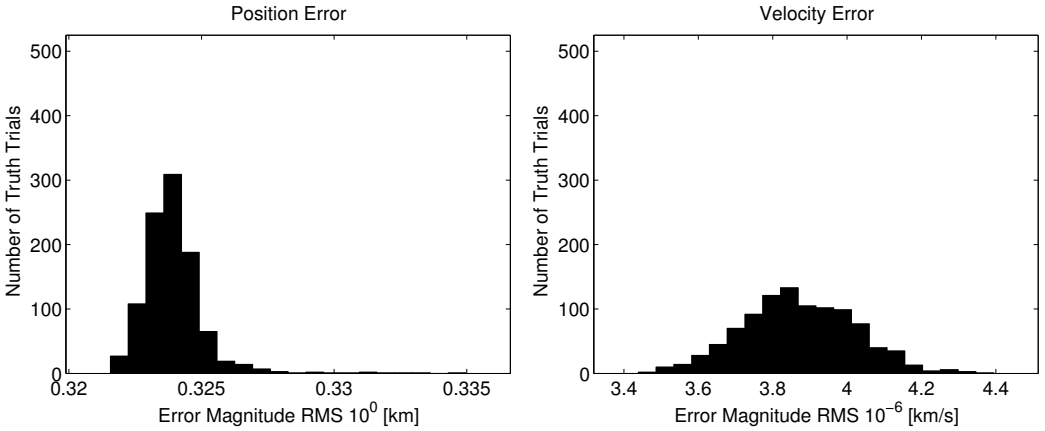

(a) Position Error (b) Velocity Error

Figure 4.17: Number of Truth Trials Within Ranges of Ensemble Spacecraft Position and Velocity Error

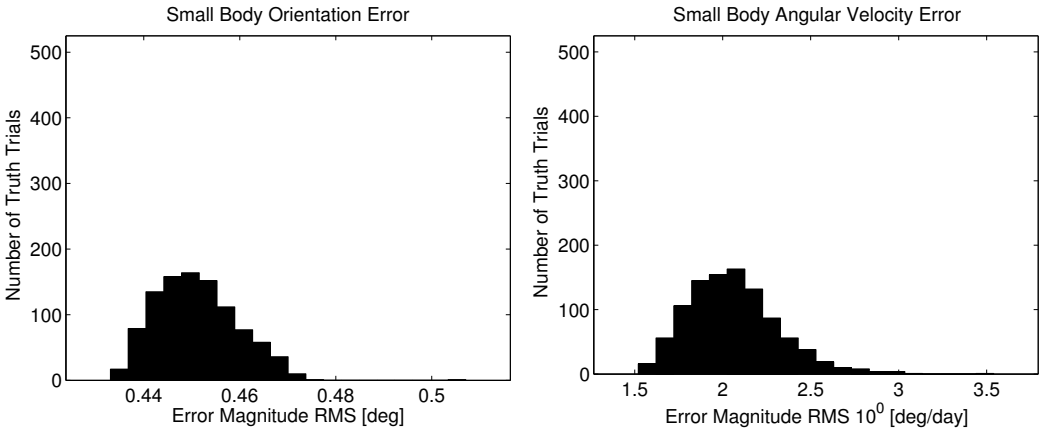

(a) Small Body Orientation Error (b) Small Body Angular Velocity Error

Figure 4.18: Number of Truth Trials Within Ranges of Ensemble Small Body Orientation and Angular Velocity Error

Due to the size of the state when all landmarks are included, and the number of measurement times in the simulations, a subset of the measurement times and landmarks are considered. The first and second times following four hour gaps in the photos are used to provide significantly different geometry,

and only the two landmarks that are visible at both times are considered. The state transition matrix (STM) Φ mapping across the four hour interval and measurement partial derivatives matrix H for these two times and landmarks are used to compute the observability matrix at each time index k:

$$O_k = \begin{bmatrix} H \\ H\Phi \\ H\Phi^2 \\ \vdots \\ H\Phi^{n-1} \end{bmatrix}_k \tag{4.3}$$

As described in Bryson [23], these separate observability matrices are combined into the Stripped Observability Matrix:

$$O = \begin{bmatrix} O_1^T & O_2^T & \cdots & O_k^T \end{bmatrix}^T \tag{4.4}$$

In this analysis, only O_1 and O_2 are computed, but observability matrices at additional times can easily be added (within computational limits). It should be noted that by using the Stripped Observability Matrix, the continuous system is approximated with a piecewise constant system. As a result, the observability metric is not guaranteed to be the same. For a linear time-varying system, the only guaranteed metric is the rank of the Observability Gramian Matrix [82], as described in equation

$$M(t_1, t_2) = \int_{t_1}^{t_2} \Phi^T(\tau, t_1) H^T(\tau) H(\tau) \Phi(\tau, t_1) d\tau \tag{4.5}$$

However, in practice the Stripped Observability Matrix will typically provide the same observability result as the Observability Gramian Matrix. Computation of the Observability Gramian Matrix in future analysis is recommended in order to verify the results obtained using the Stripped Observability Matrix.

The rank of the Stripped Observability Matrix is computed to determine the number of observable states, using a specified tolerance for the magnitude of the singular values of each mode. However, more information about the relative observability of each mode and the states that each mode includes is available through analysis of the Singular Value Decomposition (SVD) of the matrix. The SVD computes the eigenvalues and eigenvectors of $O^T O$ and OO^T, in order to compute

$$O_{p\times n} = U_{p\times p}\, S_{p\times n}\, V^T_{n\times n} \tag{4.6}$$

with the columns of U equal to the eigenvectors of OO^T, the columns of V equal to the eigenvectors $O^T O$, and S a diagonal matrix containing the square roots of the eigenvalues of $O^T O$ (or OO^T), also known as the "singular values". The eigenvectors of V, a dilution of precision measure of the observability matrix, reveal the states that correspond to the different modes of the system. The observability of these modes are dictated by the associated singular value.

The SVD of the stripped observability matrix for the two times described above is computed, and the resulting singular values are shown in Figure 4.19. To determine which states are significantly associated with each mode for these singular values, the eigenvector components with magnitude greater than 0.1 are used. The lowest singular values primarily correspond to modes that encompass the small body diagonal moments of inertia, indicating that these states possess lower observability at the simulated spacecraft altitudes (as expected based on results in Figure 4.9).

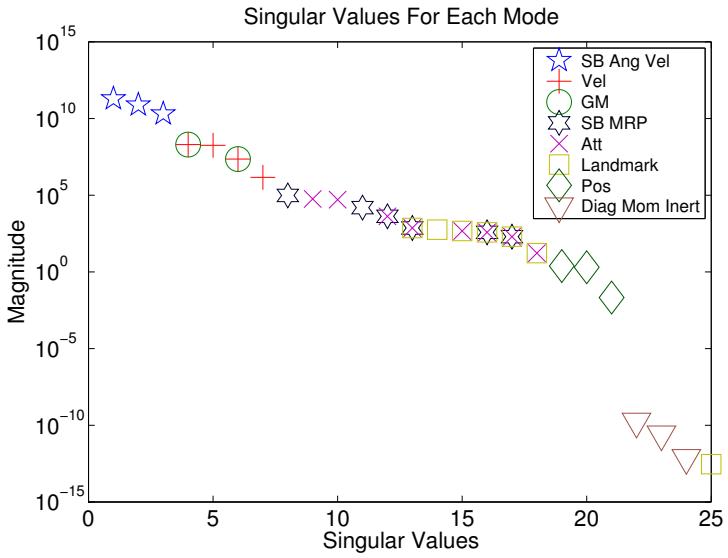

Figure 4.19: Observability Modes

Another test of the system observability for a given level of measurement noise is to run with process noise set to zero and observe if the resulting covariance for each state approaches zero. With measurement noise unchanged from the nominal scenario described above, the observability of the states is consistent with the above results. When the measurement noise is sufficiently reduced, all state covariance plots converge on zero.

A common concern regarding observability of small body landmarks and spin state is the separability of landmark longitude and body rotation: what if the nominal landmark locations are shifted in longitude by the same angle (but opposite direction) as the nominal body rotation? For a perfect sphere, such a shift would produce exactly the same computed measurements as the truth measurements (assuming no other error sources), while possessing significant error in the landmark locations and small body spin state. However,

as the small body becomes increasingly non-spherical, and the angular velocity of the body becomes less aligned with the principal axis of rotation (i.e. it increasingly tumbles), the error in the landmark locations and small body orientation becomes increasingly observable.

To demonstrate how the observability of an offset in landmark locations and body rotation increases with non-spherical shapes and tumbling motion, a five degree shift in the landmark locations and initial body rotation for three different bodies and levels of tumbling are simulated. The three bodies are defined in Table 4.11, where the "nominal" body matches what is used in the above analysis and is described in Table 4.4. Note that the GM for all bodies is identical to the nominal analysis above ($6.6692\text{x}10^{-7}$ km^3/s^2), and thus the moments of inertia have been computed assuming a triaxial ellipsoid shape and the total GM.

Table 4.11: Different Small Bodies For Landmark Rotation Offset Analysis

	Sphere	**Nominal**	**Oblong**
Max Radius	1.885 km	2.375 km	3.000 km
Med Radius	1.885 km	1.885 km	1.000 km
Min Radius	1.885 km	1.470 km	1.000 km
Inertia I_{xx}	$1.42\text{x}10^{13}$ km^2/kg	$1.38\text{x}10^{13}$ km^2/kg	$4.00\text{x}10^{12}$ km^2/kg
Inertia I_{yy}	$1.42\text{x}10^{13}$ km^2/kg	$1.89\text{x}10^{13}$ km^2/kg	$2.00\text{x}10^{13}$ km^2/kg
Inertia I_{zz}	$1.42\text{x}10^{13}$ km^2/kg	$2.22\text{x}10^{13}$ km^2/kg	$2.00\text{x}10^{13}$ km^2/kg

The three different initial angular velocities are "No Tumbling" where the rotation rate is 696 degrees per day, "Minimal Tumbling" (as described in Table 4.8), and "Nominal Tumbling" (also as described in Table 4.8). All other

aspects of the simulations are equivalent to the nominal scenario described above, with two exceptions: first, the landmark initial covariance 1-sigma is raised from 10 meters to 100 meters (reflecting the increased initial uncertainty in the initial landmark locations); second, no sampled Guassian error is added to the landmark positions or spin state (to simplify the evaluation of landmark and body rotation separability). The resulting body-fixed landmark position error over time for all thirty landmarks can be seen in Figure 4.20, for each of the scenarios.

The results in Figure 4.20 show that for a sphere, no amount of tumbling will provide observability of the offsetting landmark longitude and body rotation shift. With pure principal axis rotation (i.e. no tumbling), the shift does not become observable even for the most non-spherical shape evaluated, though some landmark body-fixed locations shift to different steady-state non-zero error locations. But with non-spherical bodies and some non-principal axis rotation, these shifts do become observable. As the body shape becomes less spherical, less tumbling is needed to effectively observe the shift, as can be seen comparing Figure 4.20e versus Figure 4.20h. The small body orientation error throughout the simulation follows the same trends as the landmark errors: with increasingly non-spherical bodies and greater levels of tumbling, the small body orientation error converges faster and more effectively. Note that in Figure 4.20e some landmarks never become visible, and thus the corresponding error values are constant.

If initial landmark uncertainty is kept at ten meters 1-sigma, convergence is much slower, so a conservatively higher initial landmark uncertainty

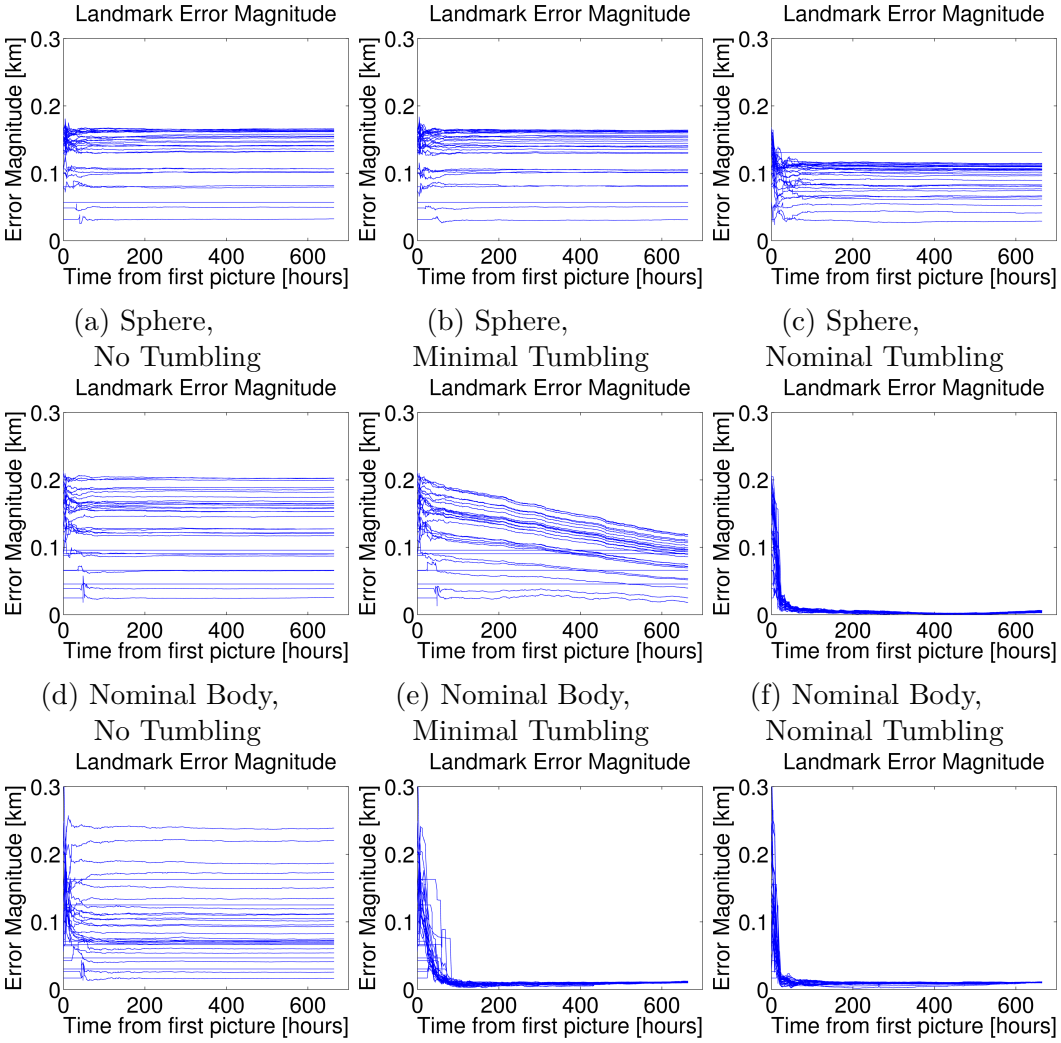

(a) Sphere, No Tumbling

(b) Sphere, Minimal Tumbling

(c) Sphere, Nominal Tumbling

(d) Nominal Body, No Tumbling

(e) Nominal Body, Minimal Tumbling

(f) Nominal Body, Nominal Tumbling

(g) Oblong Body, No Tumbling

(h) Oblong Body, Minimal Tumbling

(i) Oblong Body, Nominal Tumbling

Figure 4.20: Observability of Landmark Longitude Shift with Equal and Opposite Small Body Rotation Shift, for Different Shapes and Levels of Tumbling

should be used if an offset is possible. If additional ten meter 1-sigma Gaussian landmark error or five degrees 1-sigma Guassian initial small body orientation error are employed, there is no significant impact. Increasing offset errors up

to 30 degrees (keeping the same initial covariance values) can be corrected before the estimation begins to break down. However, increasing the initial landmark position covariance or the initial spin state orientation covariance might provide accurate correction for higher offset errors.

Much additional analysis for observability of landmark position and small body orientation offset errors is possible, including an investigation of the sensitivity of the offset observability to measurement noise and uncertainty; sensitivity to spacecraft modeling errors, initial uncertainties, and process noise; and sensitivity to small body initial angular velocity, CM offset, and moments of inertia errors and uncertainties. Monte Carlo analysis that samples each of these error sources can also be performed, and the offset error can either be sampled or deterministically varied in a trade study analysis of the body shape versus the level of tumbling.

4.8.8 Future Work

In future works, a sigma point filter (SPF) may be employed rather than the EKF to better handle the nonlinearities in the dynamics and measurement models. Possible modeling improvements include using a polyhedron shape model rather than a triaxial ellipsoid and including camera optical distortion effects. Different spacecraft trajectories may also be considered, to determine if certain orbital regimes provide better estimation of the spin state for a tumbling small body. How to better handle further degradation (or perhaps total failure) of the independent "black-box" attitude determination system may also be considered.

4.9 Conclusions

An EKF SLAM algorithm is used to effectively estimate the small body spin state for different tumbling small body scenarios, as well as the spacecraft position, velocity, and attitude; small body GM and diagonal moments of inertia; and visible landmark surface positions. The estimation converges successfully for large initial state errors, with order of magnitude error decreases in the small body attitude and angular velocity; spacecraft position and velocity; and small body GM. Landmark surface position errors are also reduced by a minimum factor of 3 for these scenarios. The small body diagonal moments of inertia have lower levels of observability for these scenarios, as expected for spacecraft trajectories many small body radii from the small body, and the small body CM offset and off-diagonal moments of inertia have no significant observability. Additionally it is observed that a small amount of measurement underweighting produces slightly better results.

When the initial small body spin state error is varied for both the minimal and nominal truth tumbling scenarios, it is seen that the steady state small body angular velocity error has remarkable resilience to larger levels of initial angular velocity error, even for errors significantly exceeding the angular velocity values. This is a critical result: if the initial angular velocity of the body is highly uncertain, the SLAM estimation algorithm can still converge on the correct values. Thus, upon arrival at a small body that is tumbling, as long as the spacecraft can determine the orientation using landmarks within reasonable accuracy (i.e. within 30 to 50 degrees in each component), then the angular velocity can be estimated with no prior knowledge.

Because the spin state is required for the SPC landmark generation method, natural feature landmarks (i.e. craters, ridge-lines, etc.) that are generated and detected using manual or computer vision techniques may be necessary to initialize the spin state estimation. These natural feature landmarks may have larger initial body-fixed position error than with the SPC method, and it is determined through a sensitivity study that the spin state parameters and the landmark positions can be effectively estimated well beyond the largest expected initial landmark position errors. The same conclusion holds for larger optical landmark measurement errors, which may occur for non-SPC methods.

The SLAM algorithm performance is also assessed for a wide range of different truth small body spin states, GM values, and CM offsets that are expected for tumbling small bodies throughout the solar system. The results reveal no issues estimating the state values, at least for the minimal number of nominal Monte Carlo trials performed for each of the 1000 different initial truth states.

To the author's knowledge, this is the first application of a SLAM algorithm to estimate the spin state of a tumbling small body. By deploying an EKF SLAM estimation algorithm, many of the relevant quantities for successful navigation of current small body missions are simultaneously estimated. Thus, the estimation technique and tuning parameters used may prove useful to future mission planners and operators of missions to small bodies. If this tool is placed in an autonomous navigation framework, it has the potential to significantly reduce the ground resources that are currently required to

navigate a small body mission, as well as increase the spacecraft autonomous capabilities.

Chapter 5

Tumbling Small Body Spin State Estimation Using Independently Simulated Images

In preparation for the Rosetta mission's arrival at Comet 67P/Churyumov–Gerasimenko in 2014, the European Space Agency ran a high fidelity simulation of a spacecraft arriving at a small body, creating simulated images of the surface. The small body was made to "tumble" (i.e. have non-principal axis rotation) in order to evaluate the European Space Operations Centre navigation tools, and the same images were sent to NASA's Jet Propulsion Laboratory (JPL) to evaluate JPL navigation tools. Following this challenging task, JPL analysts sought alternative methods for small body spin state estimation. In this work, the high fidelity tumbling small body simulation images are processed by a sequential Extended Kalman Filter (EKF) Simultaneous Localization and Mapping (SLAM) method, as described in Chapter 4. The EKF SLAM method uses a limited set of manually identified optical landmarks to estimate the small body spin state and scaled moments of inertia; the spacecraft position and velocity (the spacecraft attitude is provided by an independent attitude determination system); and the surface landmark locations. A method for generating initial landmark surface positions is provided, as well as an interpolation method for the provided spacecraft attitude

values. The SLAM method is successful in estimating the spin state of the simulated body, with final smoothed error magnitudes lower than 1 degree for the small body orientation and 2 degrees per day for the small body angular velocity.

5.1 Introduction

A major challenge when first arriving at a previously unexplored small body is the determination of its spin state. For the European Space Agency (ESA) Rosetta mission, which approached Comet 67P/Churyumov–Gerasimenko in the summer of 2014, it was not known prior to arrival whether the comet was in principal axis rotation or in a "tumbling" spin state [18, 70]. A tumbling spin state, otherwise known as "complex rotation", can be challenging to initially estimate, despite being fully predictable over short time spans using elliptic integrals in torque free scenarios [110].

To determine the effectiveness of their estimation tools in a scenario where the comet is tumbling, navigation analysts at ESA's European Space Operations Centre (ESOC) generated a simulated scenario of a spacecraft arriving at a small body with a high fidelity shape model and a tumbling spin state. The resulting simulated images were provided to NASA Jet Propulsion Laboratory (JPL) navigation analysts, as part of an effort to verify JPL navigation tools for their navigation backup role in the Rosetta mission. After significant efforts, these analysts were successful in estimating the small body spin state. However, the difficulty of the spin state estimation provided motivation to seek alternative spin state estimation methods, particularly for

future missions to other small bodies. After the Rosetta spacecraft arrived at Comet 67P/Churyumov–Gerasimenko, ESOC revealed that even though the body is in principal axis rotation, the spin rate of the body is slowing down by approximately one second per day due to gas jet activity.[1] Thus the spin rate must be continually re-calibrated, producing more work for mission operators. For the above reasons, a sequential method to estimate the spin state is desired.

The sequential estimation method chosen is the Extended Kalman Filter (EKF) Simultaneous Localization and Mapping (SLAM) filter described in Chapter 4. The objective of this chapter is to determine how effectively the previously established EKF SLAM algorithm can simultaneously estimate the spacecraft state and small body spin state using the high fidelity simulated images provided by ESOC. Unlike in Chapter 4, surface landmark identification and body-fixed landmark position initialization is addressed in this chapter.

The states that are estimated in the SLAM algorithm are the inertial spacecraft position and velocity; the inertial impulsive maneuver delta-v vectors; the small body orientation, angular velocity, and inertia tensor; and the body-fixed surface landmark positions. These quantities are estimated directly from pixel and line optical measurements of a limited set of manually identified surface landmarks in the images provided. The simulated images are taken during the small body characterization phase of the Rosetta mission, when the spacecraft is many small body radii away from the body. The spacecraft

[1] `http://aerosociety.com/News/Society-News/2998/Lecture-Report-Rosetta-How-We-Landed-on-a-Comet`

is equipped with a narrow five degree field-of-view camera that results in the small body filling most of the image array, and thus allows significant numbers of landmarks to be clearly identified.

In addition to the simulated small body images and initial nominal states provided by ESOC, initial spacecraft attitude estimates in the form of quaternions are provided from an independent attitude determination system (ADS) consisting of gyroscopes, star cameras, and an attitude determination filter. These initial attitude estimates are provided at a variety of times before, between, and after the provided images, which must be interpolated to the image times. Modified Rodrigues Parameters are used to represent the orientation of the small body in order to avoid singularities (through the standard shadow switching method described in Appendix A).

5.2 Optical Landmark Measurement Model

Optical landmark measurements are used in this scenario to estimate the spacecraft state and spin state of the body. The optical landmark measurement model is provided in section 1.1. Regarding the three major landmark types described in section 1.1, the maplet stereophotoclinometry (SPC) method requires strong knowledge of the small body spin state before the landmarks can be generated, and the significantly changing lighting conditions hinder efforts to employ standard computer vision techniques. Thus, manual selection of a limited number of landmarks is performed in this analysis.

The spacecraft-fixed frame is defined by equation 4.1 in section 4.2. The camera is assumed to be hard-mounted to the spacecraft bus, but unlike in section 4.2, the camera frame is not aligned with the spacecraft frame. There is a fixed known rotation between the frames defined as

$$\boldsymbol{R_{sc2cam}} = \begin{bmatrix} 0.001637031862182 & -0.999994400346755 & -0.002918801434789 \\ 0.999998520539662 & 0.001635482807480 & 0.000533023896782 \\ -0.000528247262468 & -0.002919669693640 & 0.999995598232000 \end{bmatrix} \quad (5.1)$$

where the camera boresight is along the camera frame z-axis. Thus the complete rotation matrix that converts inertial vectors into the camera frame is

$$\boldsymbol{R_{i2cam}} = \boldsymbol{R_{sc2cam}} \boldsymbol{R_{i2sc}} \quad (5.2)$$

The modeled camera is comparable to the Charge-Coupled Device (CCD) cameras used for navigation in previous small body missions, with a focal length of 152.4484 mm and a sensor array of 1024 by 1024 pixels, for a field-of-view of approximately 5 degrees. The diagonal terms K_x and K_y are set to 76.9231 and -76.9290, respectively, and the off-diagonal terms are set to zero. Note that the K_y value is negative as a result of a mirror in the camera optical path, reversing the image in the y-axis. Camera distortion effects on the images that are typically calibrated in flight are not included. While equation 1.5 can produce expected measurement values in increments smaller than individual pixels, the manually determined landmark observations from the images are provided in terms of whole pixels.

5.3 Spacecraft Attitude Interpolation

The spacecraft attitude is determined using an independent onboard attitude determination system (ADS) consisting of gyroscopes, star cameras, and an attitude determination filter. Using this independent estimate of the spacecraft attitude in the small body spin state estimation allows us to bypass modeling of the spacecraft attitude dynamics and maneuvers [19]. No significant additional spacecraft attitude corrections using the optical landmark measurements are necessary in this scenario. However, the provided attitude values must be interpolated to the image time.

The spacecraft attitude is provided in quaternion form at numerous times before, between, and after the provided picture times, in the same data package containing the small body images. To determine the interpolated attitude at each picture time, the first step is to determine which provided attitude quaternions are immediately before and after the photo time. The rotation matrix for each of these two quaternions (which have the scalar rotation value listed last as $q(4)$) is described by

$$\boldsymbol{R_{quat}} = \begin{bmatrix} q(4)^2 + q(1)^2 - q(2)^2 - q(3)^2 & 2(q(1)q(2) + q(4)q(3)) & 2(q(1)q(3) - q(4)q(2)) \\ 2(q(1)q(2) - q(4)q(3)) & q(4)^2 - q(1)^2 + q(2)^2 - q(3)^2 & 2(q(2)q(3) + q(4)q(1)) \\ 2(q(1)q(3) + q(4)q(2)) & 2(q(2)q(3) - q(4)q(1)) & q(4)^2 - q(1)^2 - q(2)^2 + q(3)^2 \end{bmatrix} \tag{5.3}$$

The relative rotation matrix between these two rotation matrices, $\boldsymbol{R_{Prev}}$ and $\boldsymbol{R_{Post}}$, is computed as

$$\boldsymbol{R_{rel}} = \boldsymbol{R_{Prev}}^T \boldsymbol{R_{Post}} \tag{5.4}$$

This relative rotation matrix $\boldsymbol{R_{rel}}$ is translated into quaternion form q_{rel}, as described in Diebel [41] (with the scalar rotation component listed last). The

angle of the rotation and the vector about which the rotation takes place is computed from the quaternion as

$$\begin{aligned} \theta_{rel} &= 2\cos^{-1}\left(q_{rel}(4)\right) \\ \boldsymbol{v}_{rel} &= q_{rel}(1:3) \;/\; \sin^{-1}\left(\theta_{rel}/2\right) \end{aligned} \tag{5.5}$$

The fraction of the time from the previous attitude quaternion to the image time, divided by the time between the attitude quaternions, is computed. This fraction is applied to the rotation angle θ_{rel} to obtain $\theta_{rel-frac}$ (i.e. a linear interpolation). The fractional rotation angle is then used to compute a quaternion with the same rotation vector $\boldsymbol{v}_{rel}$ and the new fractional rotation angle:

$$\begin{aligned} q_{rel-frac}(1:3) &= \boldsymbol{v}_{rel} * \sin\left(\theta_{rel-frac}/2\right) \\ q_{rel-frac}(4) &= \cos\left(\theta_{rel-frac}/2\right) \end{aligned} \tag{5.6}$$

This quaternion is then converted into the rotation matrix $\boldsymbol{R_{rel-frac}}$ using equation 5.3. The overall inertial to spacecraft-fixed frame rotation matrix at the image time is given by

$$\boldsymbol{R_{i2sc}} = \boldsymbol{R_{Prev}}\ \boldsymbol{R_{rel-frac}} \tag{5.7}$$

The average time between the provided attitude times is approximately 8 minutes, with an average rotation angle between the provided attitude quaternions of 0.26 degrees. Thus, the adjustments to the spacecraft attitude are not large using the above method are not large. Direct interpolation of the quaternion vectors is another option, using linear, quadratic, or other higher order interpolation schemes. Further study of the relative accuracy of each of these methods is needed however.

5.4 Initializing Landmark Body-Fixed Locations

A significant challenge when using landmark observations to estimate the spin state of a body is the initialization of the body-fixed locations of those landmarks on the surface of the small body. When arriving at a small body for the first time, shape models of the body can range from non-existent to more detailed models produced by radar observations of previous Earth flybys. Often only crude shape models from telescope observation campaigns are available. Without a detailed shape model (which is built after the spin state of the body has been estimated effectively), the method employed here employs a basic triaxial ellipsoid fit to the body from the initial images of the body, along with the initial landmark observations, to initialize the landmark locations on the surface.

5.4.1 Triaxial Ellipsoid Dimensions

The first step in the process to obtain initial body-fixed landmark locations for use in the SLAM estimation filter is to compute the minimum, medium, and maximum radius values of a triaxial ellipsoid that approximates the small body shape. Note that this triaxial ellipsoid is used only for initializing the landmark body-fixed positions: it is not used at any other stage of the estimation process. To obtain these radius values, the provided spacecraft state and small body spin state are propagated from the epoch time to the picture times that provide the clearest view of the minimum, medium, and maximum radius values, as determined by the analyst. In the small body mis-

sion scenario described in this chapter, the first two images provide reasonable views to measure these radius values.

The analyst selects pixel and line values in these images that they believe reasonably represent the edge points of the small body along the axes of the triaxial ellipsoid approximation. The magnitude of the two-dimensional vector between these two points for each axis are computed, and divided in half:

$$a_{pix} = \|[p1, l1] - [p2, l2]\| / 2 \tag{5.8}$$

The same equation is used for b_{pix} and c_{pix} (the other two axes). These radius values are converted to focal plane coordinates by dividing by the pixel density of the camera:

$$a_{cam} = a_{pix} / |K_x| \tag{5.9}$$

The same equation is used for b_{cam} and c_{cam}. Next the radii values are computed in Cartesian space (with units of kilometers) using the equation

$$a = a_{cam} \|\boldsymbol{r_{sc}}\| / f \tag{5.10}$$

where $\|\boldsymbol{r_{sc}}\|$ is the norm of the nominal spacecraft position that corresponds to the image time in which a_{pix} was determined, and f is the focal length of the camera. The same equation is applied to obtain b and c (the other two radii values).

5.4.2 Body-Fixed to Triaxial Ellipsoid Frame Rotation

Next the rotation matrix between the small body body-fixed reference frame and the triaxial ellipsoid frame must be determined. To start, the

$\boldsymbol{R_{i2cam}}$ and $\boldsymbol{R_{bf2i}}$ rotation matrices as described in equations 5.2 and 1.3 are obtained for one or all of the images used to compute the triaxial ellipsoid radii. The spacecraft position is then adjusted as needed perpendicular to the propagated small-body-to-spacecraft vector $\boldsymbol{r_{sc}}$, such that the user-observed approximate center of mass (CM) of the body (p_{CM}, l_{CM}) in each of the images is aligned with the computed observation pixel and line (given the spacecraft attitude). The spacecraft position is shifted instead of the spacecraft attitude because the initial position has much greater uncertainty than the spacecraft attitude provided by the ADS. To perform this shift, the inverse of equation 1.5 is first employed to compute the x and y focal plane coordinates of the CM (assuming only K_x and K_y are non-zero as described previously):

$$\begin{bmatrix} x_{CM} \\ y_{CM} \end{bmatrix} = \begin{bmatrix} (p_{CM} - p_0) / K_x \\ (l_{CM} - l_0) / K_y \end{bmatrix} \tag{5.11}$$

These x_{CM} and y_{CM} values are used to compute the vector from the spacecraft to the CM in camera coordinates (performing the opposite operation of equation 1.4):

$$\boldsymbol{O_{CM}} = \begin{bmatrix} x_{CM} * \|\boldsymbol{r_{sc}}\| / f \\ y_{CM} * \|\boldsymbol{r_{sc}}\| / f \\ \|\boldsymbol{r_{sc}}\| \end{bmatrix} \tag{5.12}$$

Note that the third component $O_{CM}(3)$ is set equal to the norm of the spacecraft nominal position prior to the shift that corresponds to the image time. The $\boldsymbol{R_{i2cam}}$ rotation matrix obtained for the image is then applied to rotate the vector from camera coordinates into inertial coordinates, and the sign is reversed to obtain the vector from the small body CM to the new spacecraft position:

$$\boldsymbol{r_{sc-shifted}} = -\boldsymbol{R_{i2cam}^T}\, \boldsymbol{O_{CM}} \tag{5.13}$$

Next the unit vectors of the body-fixed axes, multiplied by 1 kilometer, are rotated into the inertial frame and added to the new shifted vector from the spacecraft to the small body CM, producing vectors from the spacecraft to the end of the body-fixed axes vectors:

$$\begin{aligned} \boldsymbol{r_{bf-x-unit}} &= -\boldsymbol{r_{sc-shifted}} + \boldsymbol{R_{bf2i}}\ [1,0,0]^T \\ \boldsymbol{r_{bf-y-unit}} &= -\boldsymbol{r_{sc-shifted}} + \boldsymbol{R_{bf2i}}\ [0,1,0]^T \\ \boldsymbol{r_{bf-z-unit}} &= -\boldsymbol{r_{sc-shifted}} + \boldsymbol{R_{bf2i}}\ [0,0,1]^T \end{aligned} \tag{5.14}$$

These vectors are mapped into the image space using the landmark observation model, providing the user a projection of the body-fixed axes in the image. The user then rotates the body-fixed frame using one or more single-axis rotation matrices and re-maps the resulting unit vectors described in equation 5.14 until the projected vectors in the images approximately align with the maximum, medium, and minimum radii of the body as determined previously. The resulting rotation matrix $\boldsymbol{R_{bf2ell}}$ provides the rotation necessary to map the landmarks from the triaxial ellipsoid to the body-fixed frame. In the small body mission scenario described in this chapter, the resulting rotation matrix is the combination of a rotation about the first axis and the third axis:

$$\boldsymbol{R_{bf2ell}} = \boldsymbol{R_1}(20^\circ)\boldsymbol{R_3}(-55^\circ) \tag{5.15}$$

Again it is emphasized the triaxial ellipsoid axes will only approximately align with the user-determined maximum, medium, and minimum radii of the body. This manual alignment may prove more challenging for more complex shape models, but is likely to provide sufficient accuracy for the process of initializing the landmark locations.

5.4.3 Near-Side Triaxial Ellipsoid Intersections

With the dimensions of the triaxial ellipsoid approximating the small body and the rotation from that triaxial ellipsoid to the body-fixed axes determined, the near-side intersections of the triaxial ellipsoid from the initial landmark observations can be computed, providing the initial landmark body-fixed positions. Several images are necessary to obtain initial positions estimates of landmarks on all sides of the body. For each landmark, the first photo in which the landmark appears is noted. A loop over these photos is then performed, with the following steps taken for each photo.

First the spacecraft state and small body spin state are propagated from the epoch to the picture time. The small body inertial-to-body-fixed rotation matrix $\boldsymbol{R_{i2bf}} = \boldsymbol{R_{bf2i}^T}$ is computed from the propagated small body spin state, and the inertial-to-camera rotation matrix $\boldsymbol{R_{i2cam}}$ is computed for the picture time (as described in equation 5.2). Then a manual determination of the small body CM is obtained from the image by the user. The manual small body CM location, propagated spacecraft position magnitude, and $\boldsymbol{R_{i2cam}}$ are used to adjust the spacecraft position to align the observed CM location in the image with the expected location, using the method described in subsection 5.4.2, "Body-Fixed to Principal Axes Frame Rotation".

For each landmark that appears for the first time in this image, the observation pixel and line values are extracted, p_{LM} and l_{LM}. The focal plane coordinates x_{LM} and y_{LM} are computed using equation 5.11. There are now

three equations and three unknowns,

$$\begin{aligned} \boldsymbol{O_{LM}}(1) &= x_{LM} * \boldsymbol{O_{LM}}(3)/f \\ \boldsymbol{O_{LM}}(2) &= y_{LM} * \boldsymbol{O_{LM}}(3)/f \\ \|\boldsymbol{O_{LM}}\| &= 1 \end{aligned} \tag{5.16}$$

where the components of the $\boldsymbol{O_{LM}}$ unit vector from the spacecraft to the landmark in the camera frame are the three unknowns. If the expressions for $\boldsymbol{O_{LM}}(1)$ and $\boldsymbol{O_{LM}}(2)$ are used in the 2-norm equation $\|\boldsymbol{O_{LM}}\| = 1$, the third component $\boldsymbol{O_{LM}}(3)$ is solved for using

$$\boldsymbol{O_{LM}}(3) = \frac{1}{\sqrt{(x_{LM}/f)^2 + (y_{LM}/f)^2 + 1}} \tag{5.17}$$

The $\boldsymbol{O_{LM}}(1)$ and $\boldsymbol{O_{LM}}(2)$ components are then computed using this value for $\boldsymbol{O_{LM}}(3)$ and the expressions in equation 5.16.

The spacecraft-to-landmark unit vector $\boldsymbol{O_{LM}}$ is then rotated from the camera frame to the inertial frame using $\boldsymbol{R_{i2cam}}$,

$$\hat{\boldsymbol{r}}_{\boldsymbol{sc2lm}} = \boldsymbol{R}^{\boldsymbol{T}}_{\boldsymbol{i2cam}}\, \boldsymbol{O_{LM}} \tag{5.18}$$

and then further rotated into the triaxial ellipsoid frame, along with the shifted spacecraft position $\boldsymbol{r_{sc-shifted}}$, as

$$\begin{aligned} \hat{\boldsymbol{r}}^{\boldsymbol{ell}}_{\boldsymbol{sc2lm}} &= \boldsymbol{R_{bf2ell}}\, \boldsymbol{R_{i2bf}}\, \hat{\boldsymbol{r}}_{\boldsymbol{sc2lm}} \\ \boldsymbol{r}^{\boldsymbol{ell}}_{\boldsymbol{sc-shifted}} &= \boldsymbol{R_{bf2ell}}\, \boldsymbol{R_{i2bf}}\, \boldsymbol{r_{sc-shifted}} \end{aligned} \tag{5.19}$$

The equation for an ellipse is

$$x^2/a^2 + y^2/b^2 + z^2/c^2 = 1 \tag{5.20}$$

where a, b, and c are the maximum, medium, and minimum radii of the triaxial ellipsoid computed using equation 5.10. The equations for each of the triaxial ellipsoid surface position components x, y, and z are

$$\begin{aligned} x &= \hat{\boldsymbol{r}}^{\boldsymbol{ell}}_{\boldsymbol{sc2lm}}(1) * \alpha + \boldsymbol{r}^{\boldsymbol{ell}}_{\boldsymbol{sc-shifted}}(1) \\ y &= \hat{\boldsymbol{r}}^{\boldsymbol{ell}}_{\boldsymbol{sc2lm}}(2) * \alpha + \boldsymbol{r}^{\boldsymbol{ell}}_{\boldsymbol{sc-shifted}}(2) \\ z &= \hat{\boldsymbol{r}}^{\boldsymbol{ell}}_{\boldsymbol{sc2lm}}(3) * \alpha + \boldsymbol{r}^{\boldsymbol{ell}}_{\boldsymbol{sc-shifted}}(3) \end{aligned} \tag{5.21}$$

These equations for x, y, and z are fed into equation 5.20, with the intent to solve for the two possible values of α. The coefficients of the α^2, α^1, and α^0 terms are

$$\begin{aligned} A =& \hat{\boldsymbol{r}}^{\boldsymbol{ell}}_{\boldsymbol{sc2lm}}(1)^2/a^2 + \hat{\boldsymbol{r}}^{\boldsymbol{ell}}_{\boldsymbol{sc2lm}}(2)^2/b^2 + \hat{\boldsymbol{r}}^{\boldsymbol{ell}}_{\boldsymbol{sc2lm}}(3)^2/c^2 \\ B =& 2 * \Big(\boldsymbol{r}^{\boldsymbol{ell}}_{\boldsymbol{sc-shifted}}(1) * \hat{\boldsymbol{r}}^{\boldsymbol{ell}}_{\boldsymbol{sc2lm}}(1)/a^2 + \boldsymbol{r}^{\boldsymbol{ell}}_{\boldsymbol{sc-shifted}}(2) * \hat{\boldsymbol{r}}^{\boldsymbol{ell}}_{\boldsymbol{sc2lm}}(2)/b^2 + \\ & \boldsymbol{r}^{\boldsymbol{ell}}_{\boldsymbol{sc-shifted}}(3) * \hat{\boldsymbol{r}}^{\boldsymbol{ell}}_{\boldsymbol{sc2lm}}(3)/c^2 \Big) \\ C =& \boldsymbol{r}^{\boldsymbol{ell}}_{\boldsymbol{sc-shifted}}(1)^2/a^2 + \boldsymbol{r}^{\boldsymbol{ell}}_{\boldsymbol{sc-shifted}}(2)^2/b^2 + \boldsymbol{r}^{\boldsymbol{ell}}_{\boldsymbol{sc-shifted}}(3)^2/c^2 - 1 \end{aligned} \tag{5.22}$$

where $A\alpha^2 + B\alpha + C = 0$, and the value of 1 on the right hand side of equation 5.20 is moved into the C term. The value under the square root in the quadratic formula,

$$d = B^2 - 4AC \tag{5.23}$$

is checked to determine if it is greater than zero (indicating real roots and thus two valid intersections with the triaxial ellipsoid). If d is greater than zero, the root that corresponds to the near-side intersection of the triaxial ellipsoid is

$$\alpha = \frac{-B - \sqrt{d}}{2A} \tag{5.24}$$

Thus the vector from the spacecraft to the triaxial ellipsoid intersection, in the triaxial ellipsoid frame, is

$$\boldsymbol{r}_{\boldsymbol{sc2lm}}^{\boldsymbol{ell}} = \hat{\boldsymbol{r}}_{\boldsymbol{sc2lm}}^{\boldsymbol{ell}} * \alpha \tag{5.25}$$

For those landmarks that do not have an intersection with the triaxial ellipsoid (i.e. d in equation 5.23 is less than zero), the intersection of the observation unit vector with the plane located at the small body center of mass and perpendicular to the small-body-to-spacecraft vector is used. Landmarks with no triaxial ellipsoid intersections are more likely if the observation is on the edge of the body in the image, in a region of the small body that the triaxial ellipsoid doesn't include. The angle between the observation unit vector and the spacecraft position vector is computed as

$$\beta = \pi - \cos^{-1}\left(\frac{\hat{\boldsymbol{r}}_{\boldsymbol{sc2lm}}^{\boldsymbol{ell}} \bullet \boldsymbol{r}_{\boldsymbol{sc-shifted}}^{\boldsymbol{ell}}}{\left\|\boldsymbol{r}_{\boldsymbol{sc-shifted}}^{\boldsymbol{ell}}\right\|}\right) \tag{5.26}$$

where the expression is subtracted from π because the vectors are pointing in opposite directions. Then the magnitude α is computed as

$$\alpha = \frac{\left\|\boldsymbol{r}_{\boldsymbol{sc-shifted}}^{\boldsymbol{ell}}\right\|}{\cos(\beta)} \tag{5.27}$$

which is used in equation 5.25 to compute $\boldsymbol{r}_{\boldsymbol{sc2lm}}^{\boldsymbol{ell}}$. A significantly more complex "closest intersection point on the triaxial ellipsoid" method is possible to use, but not necessary for accurate estimation of the landmark positions in the scenario described in this chapter.

Finally, the initial landmark position relative to the small body CM, expressed in the body-fixed frame, is computed as

$$\boldsymbol{r}_{\boldsymbol{lm}}^{\boldsymbol{bf}} = \boldsymbol{R}_{\boldsymbol{i2bf}}\, \boldsymbol{r}_{\boldsymbol{sc-shifted}} + \boldsymbol{R}_{\boldsymbol{bf2ell}}^{\boldsymbol{T}}\, \boldsymbol{r}_{\boldsymbol{sc2lm}}^{\boldsymbol{ell}} \tag{5.28}$$

These landmark locations are used in the initial state vector that is estimated with landmark observations as described in the "Estimation and Smoothing" section.

5.5 Dynamical Models

The nominal spacecraft dynamical trajectory model includes only the central body acceleration. In the small body mission scenario described in section 5.7, the central body force at the start time is 1.289×10^{-4} N, while the solar radiation pressure (SRP) force is 1.712×10^{-6} N and the third body perturbation (TBP) force is 2.528×10^{-7} N. These values are similar to those listed in the "Max Radius" column of Table 4.1 from Chapter 4, as the mission scenario is similar (approximating the comet characterization phase of the Rosetta mission). As a result of the relatively small accelerations imparted by SRP and TBP over scenario time scale (with the gravity perturbations also likely very small, though no gravity field would be available yet), no modeling of these perturbations is necessary.

The small body spin state, which consists of the orientation and angular velocity vector, is numerically integrated via Euler's rigid body equation of motion. Torques on the small body are expected to be negligible over the scenario time span, and thus only Euler's equation of motion are needed. Torque free motion does have closed form solutions (in terms of elliptic integrals) [110], but numerical integration is chosen so that torques can be easily added in future analysis if needed. YORP effects, out-gassing effects, and other ce-

lestial bodies all can provide torques on the small body (as described in section 1.2.1.6).

Euler's rigid body equations of motion require only the ratio of the moments and products of inertia, and thus the inertia tensor can be scaled by any value [117]. As a result, the inertia tensor can only be estimated with an arbitrary scaling from the landmark observations. Typically the first diagonal moment of inertia, Ixx, is used for this scaling following a forward filter pass of the landmark observations.

Both the spacecraft and small body dynamics are numerically integrated using a variable-step seventh-order Runge-Kutta method, with a tolerance of 1×10^{-15}. In addition to the state, the state transition matrix is similarly numerically integrated using the same variable step seventh-order Runge-Kutta method, which is used to map the state covariance forward or backward in time.

5.5.1 Spin State Representation

Modified Rodrigues Parameters (MRP) are used to represent the orientation of the small body [38]. A full discussion of the advantages of using MRP values for attitude estimation, as well as their computation and how to switch to a shadow set to avoid singularities, is provided in Appendix A. The initial Euler angle values provided by the analyst are converted to MRP, and output MRP state errors and uncertainty values can be converted to Euler angles for a more intuitive representation in plotted results. The relationship between the Euler angles used to represent the small body orientation and the inertial

to body-fixed rotation matrix is as defined by the International Astronomical Union (IAU) [4]:

$$\boldsymbol{R_{i2bf}} = \boldsymbol{R_3}(\phi_{sb})\boldsymbol{R_1}(\frac{\pi}{2} - \delta_{sb})\boldsymbol{R_3}(\alpha_{sb} + \frac{\pi}{2}) \tag{5.29}$$

where ϕ_{sb} is the prime meridian (PM) twist angle, δ_{sb} is the declination, and α_{sb} is the right ascension (RA). The small body angular velocity and moments of inertia are expressed in the body-fixed frame so that the inertia tensor is constant over the integration time spans.

5.6 Estimation and Smoothing

The estimation filter employed is the standard discrete EKF, as described by Tapley, et. al. [121]. The estimated parameters are the spacecraft position and velocity; the small body orientation, angular velocity, and scaled inertia tensor; and the body-fixed locations of surface landmarks considered for navigation. The state vector is constant and does not change depending on the number of visible landmarks at each picture time. All states are simultaneously estimated directly from the landmark observations, and the standard central finite difference method is used to compute all required partial derivatives. The impulsive maneuver delta-v vectors are also indirectly estimated using the estimated states as described in subsection 5.6.1, obviating the need to including the maneuvers in the state.

To achieve the best possible estimate of the small body spin state at each picture time, as well as the other state parameters, multiple iterations of the estimation process are desired, which involves a smoothing process after

each estimation pass. Traditionally a smoother such as the 1965 Rauch, Tung, and Striebel (RTS) fixed-interval smoother [121, 118, 10] is employed, which is recommended in the literature due to its computational efficiency. However, in this analysis we deploy the smoother described in Woodburn [139]: the RTS smoother is modified to employ a full non-linear state transition to move the smoothed state backward in time for greater accuracy. While it has been well established in the literature that employing a sequential filter and smoother with no process noise is equivalent to a single iteration of the batch least squares (BLS) estimation algorithm [121], the sequential filter and smoothing approach allows for process noise to be easily and naturally included, as necessary.

Just as multiple iterations of the BLS estimation algorithm are typically performed, multiple iterations of the forward filter pass and backwards smoothing pass also provide increasingly improved state estimates. These iterations (with each iteration consisting of a single forward filter pass and backward smoothing pass) are performed over all picture times for a preset number of iterations or until corrections to the state estimates are sufficiently small. Alternatively, the filter and smoothing passes can be repeated until the measurement residuals are lower than a particular threshold. In this analysis, ten preset iterations are performed.

Note that only the spacecraft position and velocity, as well as the small body orientation and angular velocity, are modified in the smoothing pass. These state values are modified because they change in the dynamical model from one time to the next: the smoother acts to enforce the dynamics of the

system on the estimates. Thus, all "constant" states (i.e. quantities that do not change in the dynamical model) remain the same during the smoothing pass [118]. The nominal impulsive maneuver delta-v vectors are also modified during the smoothing pass, as described in the following subsection.

5.6.1 Maneuver Modeling and Estimation

The spacecraft maneuvers are treated as an impulsive change in velocity at the provided maneuver times. We assume that the maneuvers do take place at those times (i.e. we assume that the onboard clocks record the thruster fire times accurately enough for the purposes of orbit determination), and that the maneuver can be sufficiently modeled as impulsive. Maneuvers intended to change the trajectory of the spacecraft are provided as a non-zero delta-v vector, while unintentional maneuvers associated with attitude desaturation burns have an initial nominal value of zero.

During the forward filter pass, if a maneuver is known to occur between the present photo and the next photo, the most recent updated state and covariance are numerically integrated to the maneuver time. At this time, the nominal delta-v is added to the spacecraft velocity and the uncertainty in the velocity is inflated to account for the maneuver uncertainty. For the first filtering and smoothing iteration, this velocity covariance inflation is prescribed by the analyst based on previously estimated models of the spacecraft thruster performance uncertainties, in the form of a value to add directly to each of the spacecraft velocity covariance diagonal values. The overall state and covariance

are then propagated forward to the next picture time and the forward filter pass continues.

During the smoothing pass, if a maneuver is known to occur between the present photo and the previous photo, the state and covariance are smoothed to the maneuver time using the Woodburn smoothing method [139]. The state and covariance are then smoothed across the impulsive maneuver, also as described in Woodburn [139], which allows the estimation of the maneuver and its associated uncertainty. The updated maneuver delta-v is used in the following forward filter pass, and the updated uncertainty is used to inflate the spacecraft velocity uncertainty during that same forward filter pass. After updating the maneuver estimate, the smoothing pass continues backward in time. A strong advantage of this approach is that the maneuvers do not need to be added to the estimation state.

5.6.2 Truth Comparison

When comparing the nominal estimated states to the truth states provided by ESOC and JPL, care must be taken to ensure the states are represented in a consistent reference frame. The spacecraft position and velocity are expressed in inertial coordinates relative to the center of mass of the small body, for both the nominal and truth states. Thus computing the spacecraft position and velocity error involves a simple subtraction of the truth states from the nominal state estimates. However, for the remaining states, the computation of the error requires some conversion of the nominal estimated states to appropriate reference frames.

The first elements of the small body spin state are the three MRP states representing the orientation of the body. These MRP states are equivalent to a rotation matrix, or direction cosine matrix (DCM), that converts vectors from the inertial frame to the user defined body-fixed frame. In other words, it is the orientation of the body-fixed frame relative to the inertial frame. However, the small body body-fixed frame chosen by the analyst can have any orientation, as long as it is fixed to small body.

The truth orientation is provided with the body-fixed axes set equal to the principal axes of the body (i.e. inertia tensor matrix has non-zero values only for the diagonal terms). Thus the nominal estimated orientation of the body must be rotated into the principal axes as well (in order to obtain a consistent comparison of the nominal and truth orientation values), which is performed using the estimated inertia tensor. To determine the rotation from the nominal estimated body-fixed frame to the nominal estimated principal axes, the eigenvalues and eigenvectors of the estimated inertia tensor are computed, and the resulting eigenvectors are provided in three columns of a matrix,

$$\boldsymbol{R}_{pa2bf} = \begin{bmatrix} \boldsymbol{v}_1 & \boldsymbol{v}_2 & \boldsymbol{v}_3 \end{bmatrix} \tag{5.30}$$

These unit vectors define the principal axes within the previously established body-fixed frame (in which the moments of inertia are estimated by the filter). This orthogonal matrix is the rotation matrix that transforms vectors from the principal axes to the previous body-fixed frame. Thus to compute the orientation of the principal axes in the inertial frame, the original rotation

matrix describing the orientation of the body is premultiplied by $\boldsymbol{R}_{pa2bf}^{T}$:

$$\boldsymbol{R}_{i2pa} = \boldsymbol{R}_{pa2bf}^{T}\boldsymbol{R}_{i2bf} \tag{5.31}$$

which can then be transformed into MRP, Euler angles, or quaternion attitude formats. It is this transformed orientation that is then compared to the truth orientation values in order to compute the orientation error. Thus, the orientation error of the body is perhaps better described as the directional error of the estimated inertia tensor.

The error in the magnitude of the principal axes moments is readily computed as well, as the eigenvalues associated with the above eigenvectors are equivalent to the principal axes moments for the estimated inertia tensor. These eigenvalues are scaled such that the Ixx value is 1, in order to compare the scaled Iyy and Izz values to the provided truth values which are also scaled by Ixx.

This scaling by Ixx, as well as the computation of the rotation matrix from the eigenvectors described in equation 5.30, is performed using the final estimated inertia tensor from each filter pass of the observations. The rotation matrix derived from the inertia tensor is applied to all previous orientation states and then compared to the truth orientation states in order to compute the error. The rotation matrix derived from the inertia tensor eigenvectors is not computed at every filter update because the rotation varies significantly as the inertia tensor initial converges on the steady state solution.

It is important to verify that the resulting eigenvectors form a right-handed-system (RHS). This property can be confirmed by computing the de-

terminant of the matrix, with a value of positive 1 for a set of unit vectors that form a RHS. If the algorithm used to compute the eigenvectors from the inertia tensor produces a set of unit vectors that do not form a RHS, the sign of one or more of these unit vectors must be flipped in order to form a RHS. Once the set of eigenvectors forms a RHS, the rotation in equation 5.31 can be performed.

The prefit and postfit covariance values for the orientation values and inertia values are also rotated into the estimated principal axes frame by pre- and post-multiplying by the partial derivatives of the rotated values with respect to the non-rotated values:

$$P_{MRP}^{rotated} = \frac{\partial MRP_{rotated}}{\partial MRP_{original}} P_{MRP}^{original} \frac{\partial MRP_{rotated}}{\partial MRP_{original}}^{T} \tag{5.32}$$

$$P_{I}^{rotated} = \frac{\partial I_{rotated}}{\partial I_{original}} P_{I}^{original} \frac{\partial I_{rotated}}{\partial I_{original}}^{T} \tag{5.33}$$

These partial derivative matrices are computed using a standard numerical differencing approach. Note that the function used in the numerical differencing for computing the rotated inertia tensor also divides by the Ixx value to properly scale the rotated Iyy and Izz uncertainties.

The small body angular velocity, defined in the body-fixed frame, must also be rotated into a new frame in order to directly compare with the provided truth angular velocity. However, if the same rotation matrix obtained by the eigenvectors of the inertia tensor is used to rotate the angular velocity, the resulting values will be a combination of the angular velocity error and the inertia tensor error. To isolate the angular velocity error, the body-fixed

angular velocity is rotated into the inertial frame and then rotated into the truth body-fixed frame:

$$\boldsymbol{\omega}_{pa} = \boldsymbol{R}_{i2bf}^{Truth} \left(\boldsymbol{R}_{i2bf}^{Nom} \right)^{-1} \boldsymbol{\omega}_{bf} \tag{5.34}$$

Using the true difference between the nominal (prefit and postfit) body-fixed frame and the truth body-fixed frame (which is aligned with the true principal axes) allows for a more consistent determination of the angular velocity error. The angular velocity error could also be computed in the inertial frame by converting the truth body-fixed angular velocity vectors to the inertial frame.

The estimated body-fixed landmark locations are rotated into the truth body-fixed frame for error computation using the same rotation matrix defined in equation 5.34:

$$\boldsymbol{LM}_{pa} = \boldsymbol{R}_{i2bf}^{Truth} \left(\boldsymbol{R}_{i2bf}^{Nom} \right)^{-1} \boldsymbol{LM}_{bf} \tag{5.35}$$

This rotation is performed instead of using $\boldsymbol{R}_{pa2bf}$ from equation 5.30 for the same reason that the estimated body-fixed angular velocity is rotated by $\boldsymbol{R}_{i2bf}^{Truth} \left(\boldsymbol{R}_{i2bf}^{Nom} \right)^{-1}$ in equation 5.34: to isolate the error in the estimated inertia tensor from the error in the body-fixed landmark positions.

Approximate truth landmark body-fixed positions are computed by setting all other state values to the truth values (and disabling any corrections to these values) and estimating only the landmark body-fixed positions. Corrections are done for several iterations until the landmark body-fixed positions are stable and exhibit very little change with additional iteration. The body-fixed positions can also be determined from a truth shape model, but this approach

is not necessary given the stable position estimates obtained with the above method.

The prefit and postfit covariance values for the angular velocity and landmark position values are also rotated into the truth principal axes frame by pre- and post-multiplying by the same rotation matrix $\boldsymbol{R}_{i2bf}^{Truth}\left(\boldsymbol{R}_{i2bf}^{Nom}\right)^{-1}$, as this is equivalent to the partial derivative of the rotated values with respect to the original values:

$$P_{\omega}^{rotated} = \left(\boldsymbol{R}_{i2bf}^{Truth}\left(\boldsymbol{R}_{i2bf}^{Nom}\right)^{-1}\right) P_{\omega}^{original} \left(\boldsymbol{R}_{i2bf}^{Truth}\left(\boldsymbol{R}_{i2bf}^{Nom}\right)^{-1}\right)^{T} \tag{5.36}$$

$$P_{LM}^{rotated} = \left(\boldsymbol{R}_{i2bf}^{Truth}\left(\boldsymbol{R}_{i2bf}^{Nom}\right)^{-1}\right) P_{LM}^{original} \left(\boldsymbol{R}_{i2bf}^{Truth}\left(\boldsymbol{R}_{i2bf}^{Nom}\right)^{-1}\right)^{T} \tag{5.37}$$

5.7 Small Body Mission Scenario

The mission scenario is similar to the comet characterization phase of the Rosetta mission [46, 71]. In this phase, the spacecraft flies in hyperbolic trajectories with respect to the comet approximately 100 kilometers from the body [138], with minimal delta-v needed to change trajectories due to the radial distance and weak gravity of the small body. The sixty provided images are from a portion of two of these hyperbolic trajectories. The small body is well lit in the images due to the relative geometry of the sun, spacecraft, and small body. Twenty two unique landmarks are manually selected, spaced apart as much as feasible, to provide a sufficient number of landmarks in all images. Figure 5.1 displays the number of observed landmarks at each image time. The body-fixed locations for seventeen of the twenty two landmarks (77%) are initialized using the triaxial ellipsoid method described by equations 5.16

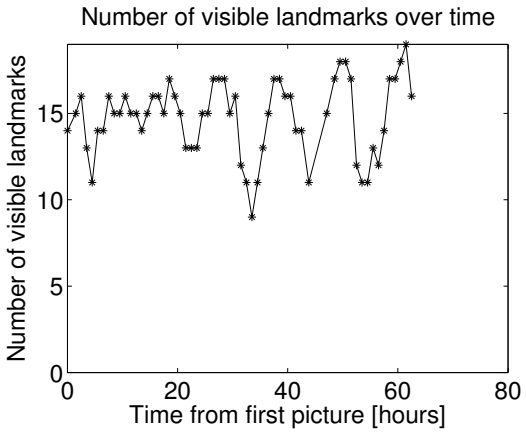

Figure 5.1: Number of Visible Landmarks For Each Picture

through 5.25, while the remaining five landmark locations (22%) are initialized using the plane intersection method described by equations 5.25 through 5.27.

In addition to the provided images and initial attitude estimates, there is a single provided non-zero nominal maneuver of [-0.7260, -0.0115, -0.4629] m/s between images 44 and 45. There are also seven provided desaturation maneuver times, which have nominal delta-v values of zero. However, the first desaturation maneuver occurs before the first picture time, and two more occur during the same measurement gap as the orbit maneuver. Thus only the remaining four desaturation maneuvers are included in the simulation. The exact times associated with these maneuvers, along with the first and last picture times, are provided in Table 5.1. The filter starts at the first picture time, and the provided initial state values are shown in Table 5.2.

Table 5.1: Event Timing

Event	**Time**
First Picture	08-Aug-2014 11:37:00.000
Desaturation Maneuver #1	08-Aug-2014 22:31:51.350
Desaturation Maneuver #2	09-Aug-2014 10:31:51.350
Desaturation Maneuver #3	09-Aug-2014 22:31:51.350
Orbit Maneuver	10-Aug-2014 09:08:00.600
Desaturation Maneuver #4	10-Aug-2014 22:27:01.400
Final Picture	11-Aug-2014 02:07:00.000

Table 5.2: Initial State Values

State	**Initial Values**
Position (Inertial)	[-19.703, 57.181, 79.557] km
Velocity (Inertial)	[4.0515×10^{-4}, 1.3679×10^{-4}, 1.5926×10^{-5}] km/s
Pole Right Ascension	220 deg
Pole Declination	-70 deg
Longitude of the Prime Meridian	142.472 deg
Body-Fixed Angular Velocity	[0, 0, 679.2454] deg/day
GM	8.067722×10^{-7} km^3/s^2
Scaled Diagonal Inertia Moments (I_{xx}, I_{yy}, I_{zz})	[1, 1, 1]
Scaled Off-Diagonal Inertia Moments (I_{xy}, I_{xz}, I_{yz})	[0, 0, 0]
Landmark Body-Fixed Positions	See section 5.4: "Initializing Landmark Body-Fixed Locations"

5.7.1 Filter Tuning

Some initial state uncertainty parameters are provided with the observations and initial nominal states received from JPL and ESOC, but are presented only as crude starting values which likely need significant adjustment. However, in a more realistic mission scenario, the initial spacecraft uncertain-

ties are likely to be significantly lower due to preliminary optical navigation using center-of-brightness measurements of the small body, in addition to radiometric tracking measurements. The initial covariance values, along with other filter parameters such as measurement noise and state process noise, are varied systematically to determine the how the results are affected. The prefit, postfit, and smoothed residuals are studied for the first and last iteration, as well as the level of state correction in the last iteration, to obtain a measure of the filter performance and the strength of the final results. Typically this systematic variation involves reducing and increasing each value one at a time by 50% to 200%. If improvement is seen by either reducing or increasing the value, it is further modified until an approximate optimum value is found (defined by the final postfit residuals RMS). The initial and final tuned EKF filter parameters resulting from this systematic variation are listed in Table 5.3.

Table 5.3: Filter Tuning Parameters

Simulation Parameter (1-σ)	**Initial Values**	**Tuned Values**
Epoch Position Covariance (Radial-Transverse-Normal)	[100, 100, 100] km	[1.4, 0.04, 0.02] km
Epoch Velocity Covariance	[1, 1, 1]$\times 10^{-1}$ km/s	[3, 3, 3]$\times 10^{-6}$ km/s
Epoch Small Body Orientation Covariance	[60, 60, 10] deg	[0.0125, 0.05, 0.05] (MRP format)
Epoch Small Body Angular Velocity Covariance	[518.4, 518.4, 518.4] deg/day	[120, 200, 2] deg/day
Epoch Small Body Scaled Diagonal Moments of Inertia Covariance	0.5	0.5
Epoch Small Body Scaled Off-Diagonal Moments of Inertia Covariance	0.05	0.05
Epoch Small Body Landmark Position Covariance	[1, 1, 1] km	[1, 1, 1] km
Measurement Noise Covariance	[3, 3] pixels	[3, 3] pixels
Process Noise q for Position and Velocity	0 km^2/s^3	1×10^{-16} km^2/s^3
Process Noise for Small Body Angular Velocity Components	0 deg/day	0.25 deg/day
Velocity Covariance Inflation - Orbit Maneuver	2×10^{-5} (km/s)^2	2×10^{-5} (km/s)^2
Velocity Covariance Inflation - Desat Maneuvers	1×10^{-6} (km/s)^2	1×10^{-6} (km/s)^2

When the simulated images and initial nominal states and covariances were initially provided by JPL and ESOC, the author attempted to estimate the spin state of the small body along with the other states listed in section 5.6, with no knowledge of the truth states. After some tuning of the initial states and process noise, a solution was found that possessed low residuals and minimal state corrections after several iterations. However, it was discovered after comparing the generated solution to the truth (using the process described in section 5.6.2), that while the spin state estimates were reasonably close to the truth values, the spacecraft states possessed error larger than the 3-sigma covariance values. A miscommunication was quickly discovered: the provided spacecraft attitude values were much more certain and close to the truth values than was originally assumed when generating the first solution (which made significant corrections to the spacecraft attitude at most observation times). This discovery led to the realization that the initial spacecraft position and velocity uncertainty would be much lower as well, in order to consistently have the small body in the images. Additionally it was recognized that initial spacecraft position uncertainty in the radial direction would be higher than the other two orthogonal directions (given the distance to the small body and assuming center of brightness measurements were used to refine the spacecraft initial state). Thus the initial position uncertainty was modified such that the provided radial uncertainty is significantly larger than the other two orthogonal directions. With these changes, along with process noise introduced in the filter to slightly inflate the spacecraft state and the small body angular velocity state, the error in the estimated solution drops

significantly. The error is also much better represented by the filter's formal covariance.

In an actual mission, without the benefit of the truth, the initial state uncertainties should be carefully considered and reduced as much as possible using radiometric tracking, center-of-brightness measurements, and laser ranging measurements (assuming the range to the small body is feasible for the laser ranging). Additionally, during the small body characterization phase the measurements from radiometric tracking and laser ranging should be either incorporated into the filter, or used to verify the SLAM solution derived from the landmark observations alone. The laser ranging measurements should prove particularly helpful in reducing the uncertainty and error in the spacecraft radial position, which has lower observability if optical navigation alone is used during mission phases in which the spacecraft is a significant distance (i.e. multiple small body radii) away from the small body [18].

The question remains however: why did the filter appear to converge on a solution (i.e. small final residuals and minimal state changes) with significant error when the initial uncertainties were larger? Two hypotheses are one, that there remains an observability problem in the overall SLAM estimation formulation, or two, that there is a non-linear convergence problem with multiple minima. To assess these two possibilities, in future work an extensive observability analysis is needed, as well as the application of alternative higher order nonlinear filters such as the Iterated EKF [13], ADF, or many other more recently developed nonlinear filters [144].

To gain greater confidence that the filter is tuned affectively such that estimated state has low error and formal covariance values effectively represent the error, Monte Carlo analysis can also be performed. Using the initial nominal states and uncertainties, many different initial truth states can be generated and the resulting collection of error and covariance values for all the trials can provide insight into the effectiveness of the current tuning parameters (as well as the sensitivity of the final estimated solutions to the initial state errors). Additionally, the process of mapping uncertainties in the dynamical models of the spacecraft and small body into the estimated state space in order to compute an appropriate level of process noise at each measurement should be pursued, as described in Chapter 3.

To improve the performance of the filter when it is initialized, the landmark body-fixed coordinates are not corrected in the first picture time (as they are either initialized using that image or an image in the future for landmarks not yet visible). Similarly the small body orientation is not corrected for the first observation of the second filter pass, for the same reason: to stabilize the filter initialization. Without these stabilizing actions in the first two iterations (when significant state error and uncertainty are still present), attempts to simultaneously correct the spacecraft position, small body orientation, and landmark positions can result in large errors and unrealistic formal uncertainties.

Process noise that acts to inflate the state uncertainty over propagation intervals is also added to improve the performance of the filter. The traditional process noise format, as defined in Tapley [121], is used for the spacecraft

position and velocity. The q value used to tune that process noise is provided in Table 5.3. Process noise is also added to the angular velocity diagonal covariance elements, via a direct addition of constant user-provided values at the end of every covariance propagation. While this direct addition method is effective in this scenario, a small body spin state process noise model that accounts for different propagation time intervals is saved for future work.

5.8 Results

The manually determined landmark image locations are provided to the EKF SLAM algorithm, which is then followed by a smoothing pass of the same data. This combination of filtering and smoothing is repeated ten times, leading to negligible changes in the state estimates in the final iterations. Figure 5.2 provides the spacecraft position prefit and postfit error magnitudes, as well as the 3-σ prefit and postfit covariance magnitudes, for the final iteration. Figure 5.2 also provides the position values for each picture time of the scenario, for the final iteration. The resulting smoothed inertial trajectory is shown in Figure 5.3.

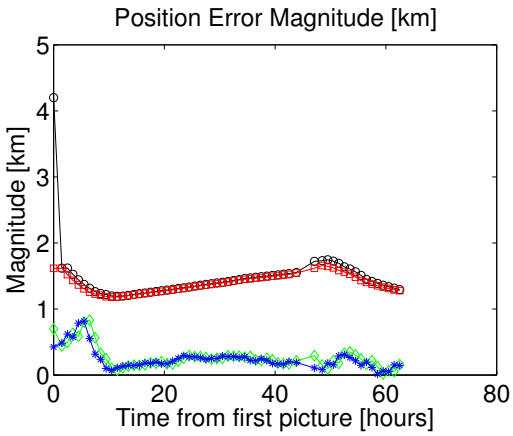

(a) Iteration 1 Error, Covariance

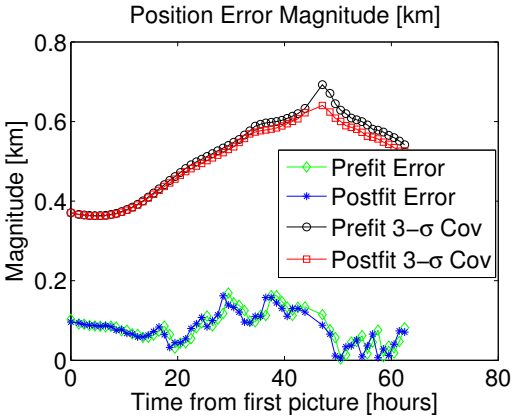

(b) Iteration 10 Error, Covariance

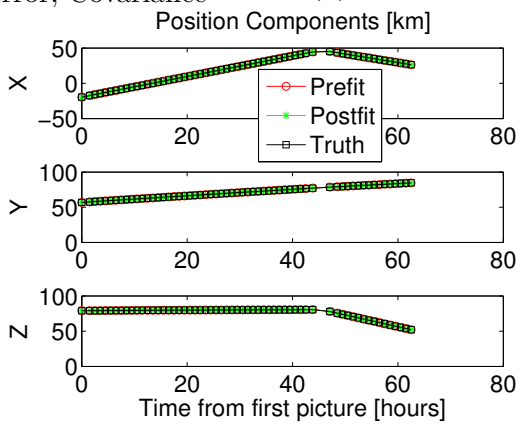

(c) Iteration 10 State Components

Figure 5.2: Spacecraft Position

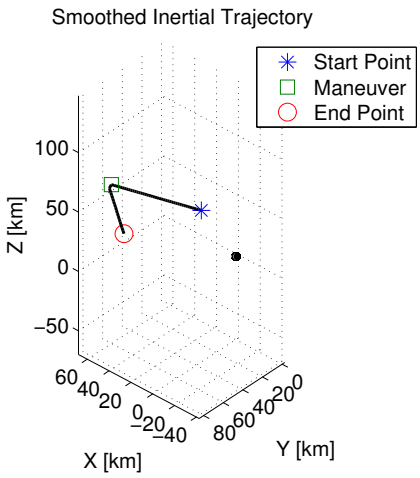

Figure 5.3: Smoothed Inertial Spacecraft Trajectory

Figure 5.4 provides the spacecraft velocity prefit and postfit error magnitudes, as well as the 3-σ prefit and postfit covariance magnitudes, for the first and final iteration. Note the increases in the velocity uncertainties at the maneuver times in the first iteration, as the filter opens up the velocity covariance to account for the maneuver uncertainty. The error in the impulsive delta-v

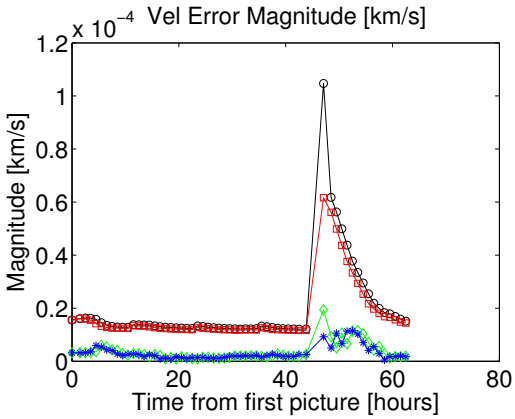

(a) Iteration 1 Error, Covariance

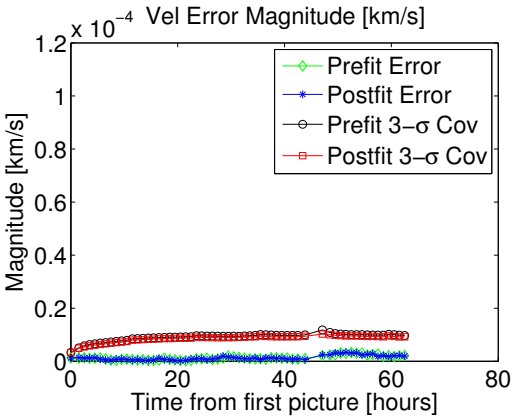

(b) Iteration 10 Error, Covariance

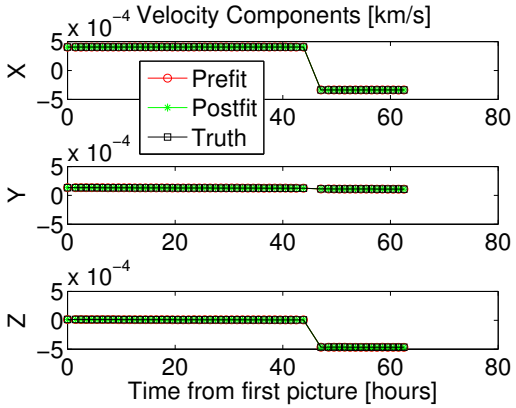

(c) Iteration 10 State Components

Figure 5.4: Spacecraft Velocity

of the orbit maneuver at hour 45 is reduced from 17.4 mm/s to 2.8 mm/s, an 84% reduction. The much smaller desaturation maneuvers initially have error

magnitudes ranging from 0.5 to 1 mm/s, and these errors are reduced by an average of 45%.

Figure 5.5 provides the small body orientation prefit and postfit error magnitudes, as well as the 3-σ prefit and postfit covariance magnitudes, for the first and last iteration. To avoid singularities in the Euler angle representation that occur when using the nominal body-fixed frame, first the estimated MRP states and uncertainties are rotated into the principal axes frame as described in section 5.6.2. These MRP states and the associated covariance matrices are then converted to Euler angles and Euler angle uncertainties. Note that some spikes remain in the covariance and errors in Figure 5.5b, corresponding to the minimum declination values shown in Figure 5.5c. The MRP error and covariance magnitudes are shown in Figure 5.5d, with much smoother plots of the error and covariance. The peak values in the MRP covariance plot are a result of the shadow switching, which occur at the points when these peak values occur. The much larger spikes in the Euler angle error and magnitude may be a result of the small additional sensitivity in the mapping from MRP values to Euler angles as the declination approaches the singularity value of -90 degrees, but additional investigation is needed to verify this hypothesis.

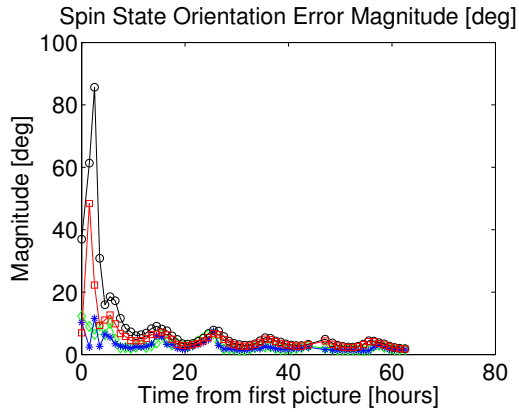

(a) Iteration 1 Error, Covariance

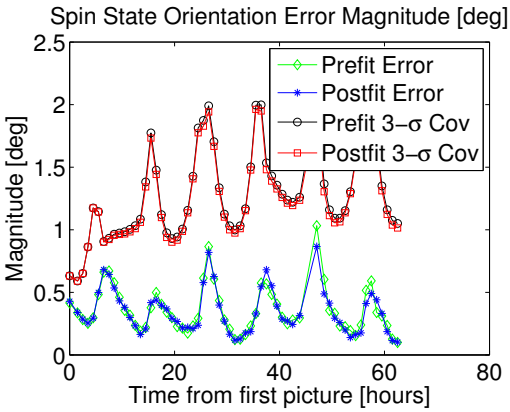

(b) Iteration 10 Error, Covariance

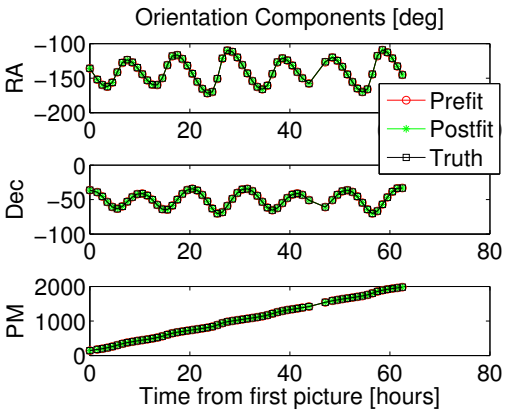

(c) Iteration 10 State Components

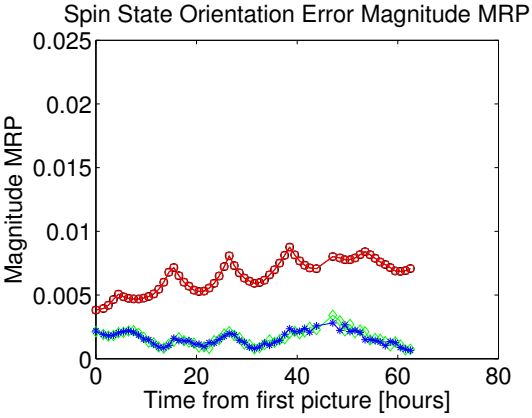

(d) Iteration 10 MRP Error, Covariance

Figure 5.5: Small Body Orientation

Figure 5.6 provides the small body body-fixed angular velocity prefit and postfit error magnitudes, as well as the 3-σ prefit and postfit covariance magnitudes, for the first and last iteration. The angular velocity is specified in the small body body-fixed frame to allow a constant inertia tensor in the numerical integration of the spin state. Note that the estimated angular velocity values used to compute the error and the associated covariance values

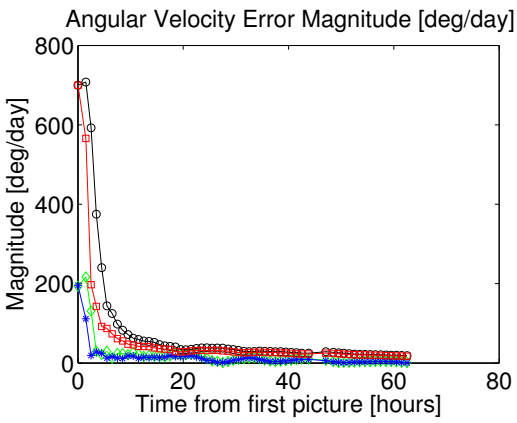

(a) Iteration 1 Error, Covariance

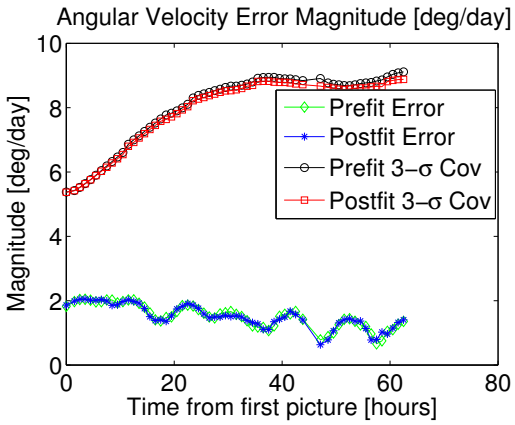

(b) Iteration 10 Error, Covariance

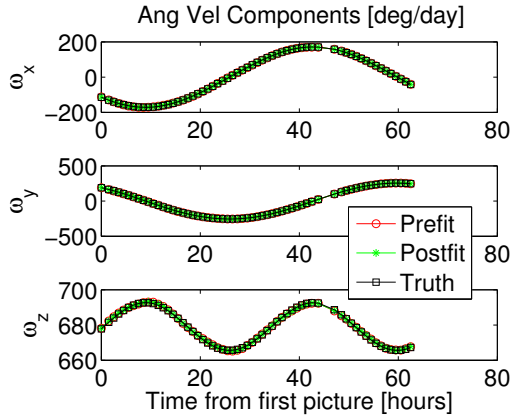

(c) Iteration 10 State Components

Figure 5.6: Small Body Angular Velocity

are rotated into the truth principal axes frame as discussed in section 5.6.2, "Truth Comparison".

Figure 5.7 displays the first and last iteration estimated principal axes moments, as computed by the rotation into the principal axes of the final estimated inertia tensor in each iteration (see section 5.6.2). The principal axes moments (along with the converted covariance values) are scaled by the Ixx value, and thus only the Iyy and Izz are plotted. The 3-σ covariance values are shown via the error bars added to the estimated states. Note that the last iteration estimated values better match the truth values and the uncertainties are smaller as well.

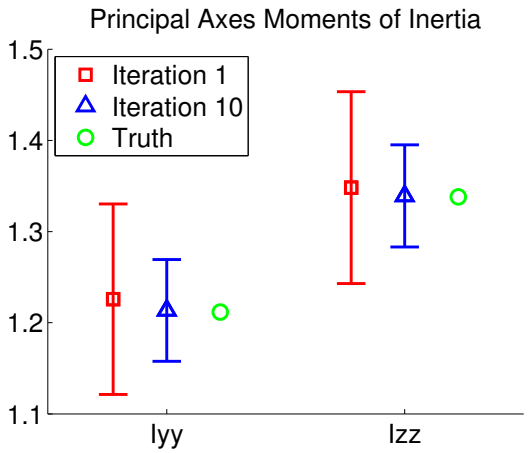

Figure 5.7: Small Body Principal Axes Moments of Inertia - Scaled by Ixx

Figure 5.8 provides the body-fixed landmark position error for the first landmark identified, for the first and last iteration, as well as the median error and covariance of all twenty two landmarks identified. Note that the variation in the landmark errors in Iteration 10 is due almost entirely to variations in the small body orientation, as these body-fixed landmark locations values are rotated from the nominal body-fixed frame to the truth body-fixed frame at each picture time (as described in section 5.6.2). The landmark locations do not shift significant amounts in the final iteration. The final positions in the body-fixed frame for the final iteration are displayed in Figure 5.9.

Figure 5.10 provides the prefit, postfit, and smoothed residuals for the first iteration and the final iteration. The improvement achieved in the estimated states from the first to final iteration is summarized effectively by the plots of the measurement residuals. The final image provided of the high fidelity simulated small body is displayed in Figure 5.11, along with the final iteration smoothed prefit, postfit, and actual observations of the landmarks.

Overall the estimated states converge reasonably well in the first iteration, particularly the spin states and landmark locations, and additional iteration allows significantly lower errors and uncertainties for the final state estimates. However, this strong performance is a result of an extensive tuning process and significant changes to the initial state uncertainties from those initially provided. The provided truth states illuminated the incorrect initial assumptions about the uncertainty in the spacecraft states (especially regarding the provided spacecraft attitude values), which reinforces the importance of carefully considering the initial states and uncertainties resulting from prior

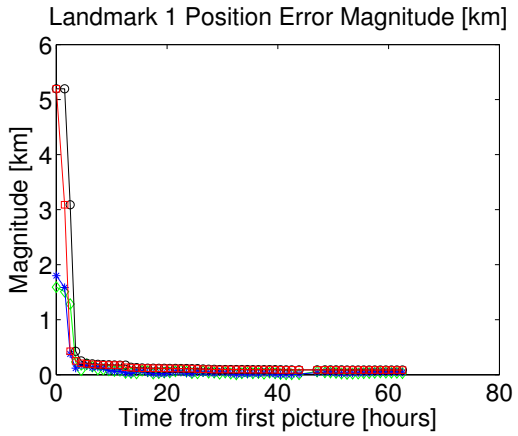

(a) Iteration 1, Landmark 1

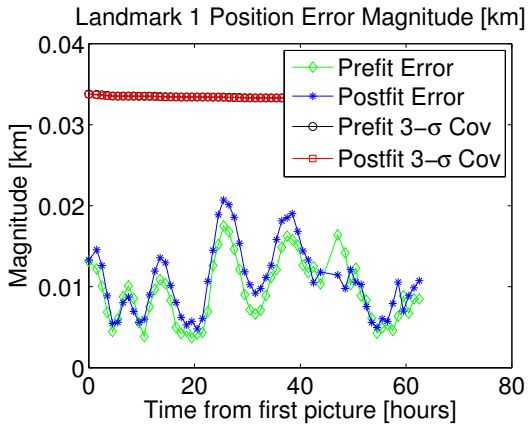

(b) Iteration 10, Landmark 1

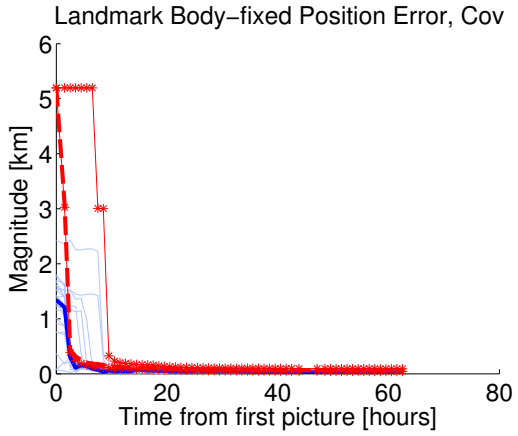

(c) Iteration 1, Median Error, Cov

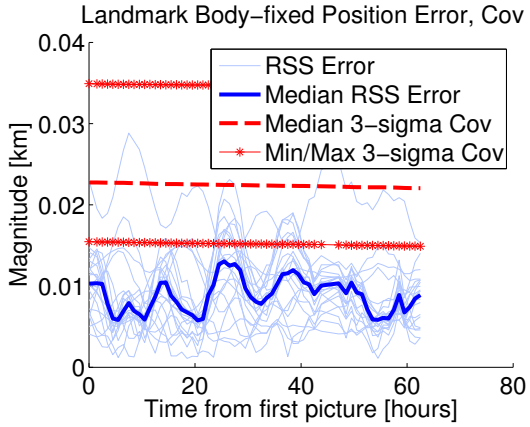

(d) Iteration 10, Median Error, Cov

Figure 5.8: Body-Fixed Landmark Position Error, Covariance

radiometric tracking, optical navigation using center-of-brightness measurements, and the independent spacecraft ADS.

The next important steps towards the goal of a fully autonomous initial spin state estimation capability include an automated method that can consistently and accurately identify a limited set of surface landmarks spaced sufficiently apart, as well as an algorithm that can automatically fit a 3D triax-

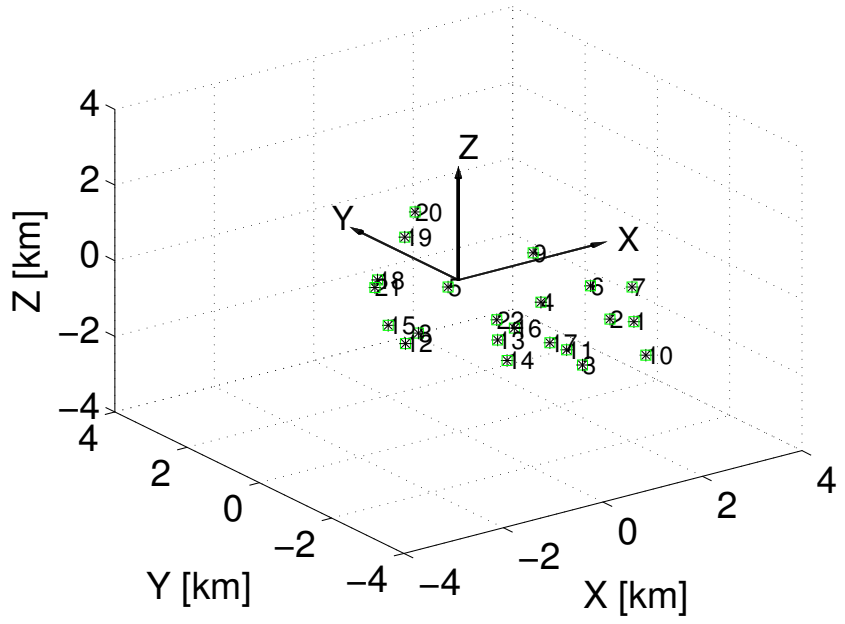

Figure 5.9: Smoothed Body-Fixed Landmark Positions

ial ellipsoid to the body based on the first few images taken (for the landmark position initialization). If onboard application of these algorithms is desired, computational efficiency must be carefully considered. For ground processing, additional iteration via repeated filtering and smoothing passes can further refine the state estimates (and allow for process noise to be used, unlike the standard BLS).

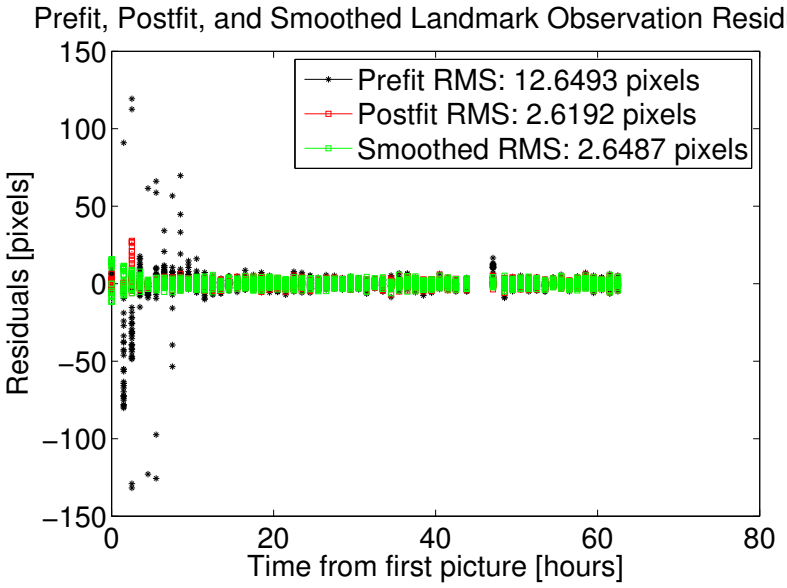

(a) Iteration 1

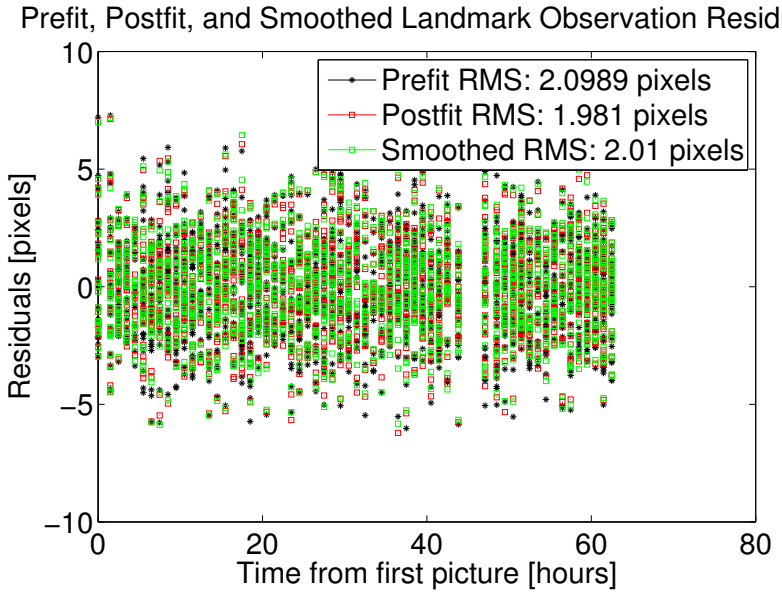

(b) Iteration 10

Figure 5.10: Measurement Residuals

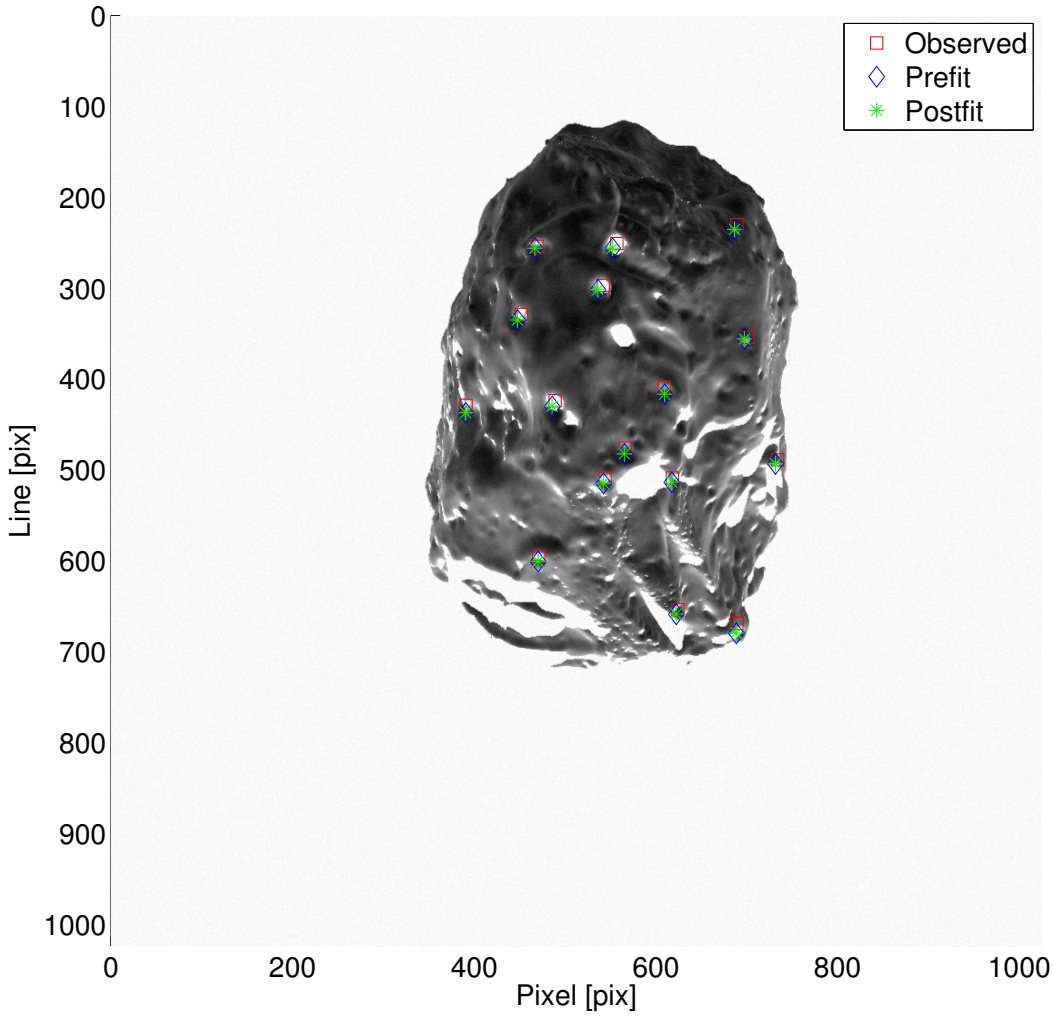

Figure 5.11: Prefit, Postfit, Actual Observations at Final Picture Time (colors inverted for printing purposes)

5.9 Conclusions

A sequential EKF SLAM method effectively estimates the spin state of a high fidelity simulated tumbling small body using images provided by the ESA's ESOC and NASA's JPL. A limited set of landmarks are manually identified in the images, and the method for generating initial body-fixed

surface positions for those landmarks is provided. Initial spacecraft attitude quaternions are also provided, specified at times before, between and after the images. These attitude values are interpolated to the image times.

In addition to estimating the small body spin state, the following states are also successfully estimated: the spacecraft position and velocity, the small body scaled inertia tensor, and the landmark surface positions. Multiple iterations of filtering and smoothing passes are performed, providing final smoothed spin state estimates and indirect estimates of the impulsive maneuver delta-v vectors. A method for rotating the spin states, inertia tensor, and landmark locations into reference frames that allow a consistent comparison to the provide truth states is provided. The procedure for converting the associated formal state uncertainties is also described.

The sequential EKF SLAM implementation provides a new method to estimate the spin state of a small body, which has the potential to significantly boost initial spin state estimation capabilities in future missions to small bodies. In particular, small bodies that are tumbling have proven challenging for heritage tools when initially estimating the spin state, which provided the motivation for this work. The sequential approach, instead of the BLS approach used previously, allows process noise to be incorporated as needed, and lends itself better to any future onboard estimation capabilities. Additionally, torques delivered to the body via outgassing or other sources can be accounted for over time. The archival of the filter structure and tuning parameters is also important, as the literature is generally absent those details.

As discussed in Section 5.7.1, tuning of the filter initially proved challenging due to unrealistically high uncertainties in the initial spacecraft states. Upon receiving the truth states, this discrepancy was revealed, leading to significant improvements in the initial state uncertainties. Without knowledge of the truth, as will be the case in an actual mission, the initial state uncertainties from prior spacecraft navigation using radiometric tracking and center-of-brightness optical measurements should be carefully considered. The author also strongly recommend employing additional measurements of the spacecraft during the small body characterization phase such radiometric tracking and laser ranging to the small body surface to verify the SLAM algorithm is effectively estimating the combined spacecraft and small body state.

Chapter 6

Conclusions

This dissertation has described advances in estimation methods that are focused on small body optical navigation, and in particular techniques that can assist in NASA's goal of greater autonomous navigation capabilities. Section 1.3 lists the primary contributions made to the state-of-the-art, and Appendix B lists the publications associated with the research from each chapter. The primary conclusions are reviewed in this chapter, with a focus on how these estimation method advances can contribute to future missions. Avenues for related future research are explored as well.

Chapter 2 describes the use of standard and higher order sequential estimation methods to estimate the spacecraft state from optical small body surface landmark measurements, in an effort to provide an estimation framework amenable to the sequential nature of autonomous onboard navigation and achieve greater filter accuracy and uncertainty representation. The standard Extended Kalman Filter (EKF) and higher order Additive Divided-Difference sigma point Filter (ADF) are implemented, and extensive Monte Carlo analyses are performed to compare the different estimation techniques. Significantly improved estimation performance is achieved by the ADF over the EKF for larger initial state errors and time between measurements. The measurement

update portion of the ADF provides most of the improvement over the EKF, with much longer measurement interval times necessary to show improvement from the state propagation step of the ADF (versus standard numerical propagation).

By employing the ADF instead of the EKF, significant improvement can be achieved in the state error and uncertainty representation for scenarios with larger initial state errors (which may easily occur) and scenarios with longer intervals between measurements (which can also easily occur). The computational costs are slightly higher for the ADF versus the EKF, but still well within computational limitations of onboard systems. Additionally, by using only the measurement update portion of the ADF, the vast majority (if not all) of the improvement in estimation performance can be achieved, for a significantly lower computational cost than employing the full ADF.

While the use of higher order filters can reduce the errors introduced by the linearization of non-linear dynamics and measurements models, errors and uncertainties in the dynamical models themselves can lead to significant problems in the estimation and uncertainty representation of the state parameters. To address this problem, a novel method to precompute a process noise profile along a reference trajectory using consider covariance analysis tools and filters is presented in Chapter 3. The process noise profile is intended for use in an onboard navigation filter, allowing the filter to account for time- and state-dependent perturbations in the dynamics. Little to no traditional extensive manual tuning is required. The new process noise method also produces

formal uncertainties that better match the estimate errors in scenarios with highly variable dynamics.

There are limitations for the new process noise computation method however. A reference trajectory must exist, and the vehicle must not deviate too far from the reference path for the precomputed process noise to be effective. The errors in the considered model parameters must also approximately match the model parameter uncertainties used for the process noise precomputation.

The improvements to state errors and uncertainties can enable missions to meet more stringent navigation requirements in mission phases with rapidly changing dynamics, as well as significantly reduce the time required by the ground operators to tune the onboard filter. The method can also be applied to numerous other fields that employ onboard robotic navigation, including many terrestrial applications. Any robotic vehicles that operate in highly variable dynamical environments and possess onboard navigation would be excellent candidates for this new process noise profile method.

The first half of the dissertation focuses on innovations that have strong potential to assist with small body navigation when the spacecraft has moved into orbit about the body, and in particular the lower orbits. However, significant challenges also exist for the initial approach phase of missions to small bodies, primarily due to the lack of detailed knowledge regarding the shape and spin state of the body (as well as the spacecraft state relative to the body). To address these challenges, chapter 4 explores the use of Simultaneous Local-

ization And Mapping (SLAM) to estimate not only the spacecraft state but also the spin state of the small body and the surface landmarks during the initial approach phase of a mission (also known as the small body characterization phase). The Rosetta mission scenario is used to demonstrate the SLAM algorithm, where state estimates converge successfully for large initial state errors. The convergence for some states occurs within two to three photos, and all states are converged within two arcs of the eight-arc trajectory.

The steady state small body angular velocity error has remarkable resilience to larger levels of initial angular velocity error, even for errors significantly exceeding the angular velocity values. This is a critical result: if the initial angular velocity of the body is highly uncertain, the SLAM estimation algorithm can still converge on the correct values (i.e. the angular velocity can be estimated with no prior knowledge). The SLAM estimation algorithm also remains effective for a range of different truth spin states, masses, and center of mass offsets that correspond to expected tumbling small bodies throughout the solar system. Additionally the SLAM algorithm performs well for the largest expected initial landmark position errors and optical landmark measurement errors.

Extensive observability analyses employing the Stripped Observability Matrix and the Singular Value Decomposition is used to determine the relative observability of each of the states, with the small body angular velocity fortunately having the greatest observability of all the estimated states. One common observability problem is differentiating a consistent error in the longitude of the landmark surface positions from an error in the rotation of the

body. Exploring the space of different body shapes (spherical to highly non-spherical) and tumbling states (principle axis rotation to highly tumbling) reveals some level of non-sphericity and non-principal axis rotation is needed to differentiate these errors, with increasing non-sphericity and non-principal axis rotation leading to faster convergence of these quantities.

Chapter 5 uses the SLAM spin state estimation method developed in Chapter 4 to estimate the spin state of a high fidelity tumbling small body independently simulated by the European Space Agency (ESA). Also successfully estimated are the spacecraft position and velocity; small body inertia tensor; landmark surface positions; and via an indirect estimation process the impulsive maneuver delta-v vectors. A method for initializing the small body landmark locations is provided, as well as an interpolation technique for the provided spacecraft quaternions.

After performing a forward filter pass of the landmark optical measurements at each photo time, the results are processed in a backward smoothing pass. The forward and backward passes are repeated a total of ten iterations to further refine the state estimates. The maneuvers are indirectly estimated via this smoothing process as well. However, the frequency of the desaturation maneuvers, the small magnitude of those maneuvers, and the process noise added to the spacecraft state prevent significant refinement of the desaturation maneuver estimates. Despite the limited accuracy of the desaturation maneuver estimates, the spacecraft and spin states are well estimated.

The use of sequential SLAM techniques in future missions to small bodies may allow mission operators to overcome the limitations of current navigation tools that are not designed to handle tumbling bodies. Additionally, SLAM may enable spacecraft to approach the small body surface on a shorter timeline, which can reduce risk in scenarios where poorly understood and unpredictable forces such as comet outgassing can occur. The use of SLAM in an onboard filter also has the potential to significantly reduce required ground resources for navigation of the spacecraft and estimation of the small body spin state and shape.

6.1 Future Work

In addition to the higher order ADF employed in Chapter 2, many other higher order filters have the potential to provide enhanced navigation performance, such as the particle filter [118] or the Gaussian Sum Filter [2]. The EKF, ADF, and other higher order sequential filters can also be compared in greater detail to a wide variety of BLS approaches (with varying arc-lengths). Performance of all of these filters can be studied in many different small body scenarios as well, with particular interest in the performance for descent trajectories to the surface when filter accuracy can significantly affect landing accuracy.

The novel method to compute a process noise profile from dynamical model uncertainties also has the potential to significantly improve the measurement uncertainty used in a filter to account for errors in the measurement model. One example is the optical landmark measurement model, which can

have errors in the camera properties as well as the process used to determine the landmark location in the image.

A preliminary analysis is performed in Chapter 3 investigating the effect on the performance of the filter when the model parameter uncertainty used to compute the process noise profile does not match the actual error in those model parameters. A more complete analysis that examines the sensitivity of the filter performance to this mismatch in the model parameter uncertainty versus error would likely provide significant value, especially if the analysis could be performance for a wide range of mission scenarios.

The application of this novel process noise precomputation method to other estimation problems that possess mismodeled or unmodeled perturbations, particularly for large, state-dependent perturbations, would also be of great interest. Examples include modeling the spacecraft mass, area, and reflectivity coefficient as consider parameters for the process noise computation to better account for SRP and TBP errors, as well as time-dependent atmospheric properties to better account for drag errors. Many other terrestrial applications likely exist as well. Employing a simplified non-linear problem that bridges the gap between the linear example problem and higher fidelity nonlinear scenarios is also recommended for future work, to better explore the strengths and limitations of the new precomputed process noise method.

To assist mission designers and navigators as they assess different possible trajectories for future missions, it would be helpful to generate averaged process noise profiles that are functions only of the spacecraft radius mag-

nitude or other temporal/spatial variations. These averaged process noise values could also be employed onboard if it is determined they provide sufficiently accurate process noise profiles. Along the same lines, an exploration of the effectiveness of different interpolation techniques used to represent the precomputed process noise profile would likely be useful for future mission navigators, as an onboard interpolation scheme could prove necessary to fit within the computational constraints of an onboard processor. Further, also useful would be an investigation of how these interpolation techniques are affected by changes in the measurement frequency and structure, as well as how the filter is affected when a particular measurement is not obtained (or the measurement times are not as planned).

Perhaps the most critical future work for the problem of initial small body spin state estimation is the application of the new process noise generation method described in Chapter 3 to better determine the process noise that should be employed for the spacecraft and small body state, based on the predicted uncertainty in the dynamical models. By employing the new process noise method, a significant amount of the tuning now required could be eliminated. Along these same lines, mapping uncertainties in the observations and the size and orientation of the triaxial ellipsoid used for landmark location initialization has the potential to provide significantly improved initial landmark uncertainties for the SLAM process. More realistic initial state uncertainties from center-of-brightness optical measurements and radiometric tracking measurements should also be investigated.

While relatively few landmarks are needed to successfully estimate the spin state of a tumbling small body (thus making manual selection feasible), the use of modern open source image processing algorithms such as Scale-Invariant Feature Transform (SIFT) and Speeded Up Robust Features (SURF) could prove particularly useful in reducing operator work load, as well as potentially reduce measurement errors. However, an investigation is needed to determine if these algorithms can consistently recognize landmarks in very different lighting conditions and re-acquire the landmarks after they have rotated out of sight. Along these same lines, also useful would be an analysis of how the number of landmarks and the distribution of the identified landmarks on the surface affects the spin state estimation performance. Also of value would be an investigation of the limits of the SPC method for generating and identifying landmarks on tumbling small bodies, to determine what level of tumbling will necessitate other landmark methods for initial spin state estimation.

Other potential future work regarding the use of the SLAM algorithm for small body spin state estimation includes a comparison of the EKF to the BLS method and higher order sequential filters such as the ADF from Chapter 2, an investigation of how the inclusion of camera optical distortion parameters affect the filter performance, and a study how different orbit regimes in the approach phase affect the spin state estimation of a tumbling small body.

Appendices

Appendix A

Modified Rodrigues Parameters

Modified Rodrigues Parameters (MRP) [38] are used to represent the orientation of an object, providing an alternative to standard representations such as Euler angles and quaternions. If Euler angles are provided by the analyst, these can be converted to MRP for internal use within the program. Similarly the output attitude states, errors, and uncertainties intended for plots and illustrations can be reverted to Euler angle values from MRP, for a more intuitive representation.

A.1 Computation and Time Derivative

If converting from an Euler angle attitude representation, these angles must initially be converted to quaternion format [41]. The three-component MRP vector is computed directly from the quaternion representation:

$$\boldsymbol{\sigma} = \frac{\boldsymbol{q}}{1 + q_0} \tag{A.1}$$

where $\boldsymbol{q}$ is the vector portion of the quaternion and q_0 is the scalar part. The MRP vector is converted back to a quaternion [22] using

$$\begin{aligned} q_0 &= \frac{1 - \|\boldsymbol{\sigma}\|^2}{1 + \|\boldsymbol{\sigma}\|^2} \\ \boldsymbol{q} &= \frac{2\boldsymbol{\sigma}}{1 + \|\boldsymbol{\sigma}\|^2} \end{aligned} \tag{A.2}$$

The quaternion can be used to compute the appropriate Euler angles for output as desired.

The time derivative of the MRP representation used in dynamical models is

$$\dot{\boldsymbol{\sigma}} = \frac{1}{4}\left[\left(1 - \boldsymbol{\sigma}^T\boldsymbol{\sigma}\right) I + 2\boldsymbol{\sigma}^x + 2\boldsymbol{\sigma}\boldsymbol{\sigma}^T\right]\boldsymbol{\omega} \tag{A.3}$$

where $\boldsymbol{\omega}$ is the angular velocity, $\boldsymbol{\sigma}^x$ is the skew-symmetric cross product matrix, and I is the 3x3 identity matrix.

A.2 Shadow Set Switching

The primary advantage of the MRP representation is how easily the singularity (which must exist in any three-state attitude representation) can be avoided. The MRP singularity only exists at a 360 degree rotation, and can easily remain far from the singularity by switching to what is known as a shadow set. As described in Karlgaard [61], the shadow switch is performed when the magnitude of the MRP vector exceeds 1, which is equivalent to a rotation of 180 degrees (and thus exactly halfway between the singularities of the standard MRP set and the shadow MRP set). The switch to the shadow MRP values is done via

$$\boldsymbol{\sigma}^{\boldsymbol{S}} = -\frac{\boldsymbol{\sigma}}{\boldsymbol{\sigma}^{\boldsymbol{T}}\boldsymbol{\sigma}} \tag{A.4}$$

where $\boldsymbol{\sigma}^{\boldsymbol{s}}$ is the "switched" MRP vector. Note that the magnitude of the nominal MRP vector dictates when the switching is done, and the truth MRP vector used for computing the error is switched only when the nominal MRP is switched (regardless of the truth MRP vector magnitude). The dynamical

propagation and filter update equations are identical for the standard MRP and shadow MRP values, another strong advantage of the MRP representation.

The covariance must also be adjusted for each shadow set switch, as described by

$$\bar{P}_k^S = \Lambda \bar{P}_k \Lambda^T \tag{A.5}$$

where Λ is the identity matrix with dimension equal to the estimated state except for those elements associated with the MRP:

$$\Lambda = \begin{bmatrix} I & 0 & 0 & 0 & 0 \\ 0 & \ddots & 0 & 0 & 0 \\ 0 & 0 & \Lambda_{MRP} & 0 & 0 \\ 0 & 0 & 0 & \ddots & 0 \\ 0 & 0 & 0 & 0 & I \end{bmatrix} \tag{A.6}$$

Λ_{MRP} is defined using the partial of the switched MRP vector with respect to the original MRP vector,

$$\Lambda_{MRP} = \frac{\partial \boldsymbol{\sigma}^{\boldsymbol{S}}}{\partial \boldsymbol{\sigma}} = 2\left(\boldsymbol{\sigma}^T\boldsymbol{\sigma}\right)^{-2}\boldsymbol{\sigma}\boldsymbol{\sigma}^T - \left(\boldsymbol{\sigma}^T\boldsymbol{\sigma}\right)^{-1} I \tag{A.7}$$

It is important to convert the full covariance by pre-multiplying and post-multiplying by Λ rather than converting only the MRP covariance diagonal elements using Λ_{MRP}, in order to also convert the associated cross-correlation terms.

A.3 Other Advantages for Attitude Estimation

The MRP attitude representation is particularly advantageous when used as part of an attitude estimation process. Crassidis [38] shows that an additive estimation approach such as the standard additive EKF is effective for

the MRP representation, particularly when the measurement model is function of a rotation matrix (defined by the MRP) multiplied by a vector (as is the case for optical navigation). Thus the multiplicative kalman filter that is often necessary for attitude estimation can be avoided, and as a result the spacecraft attitude can be estimated simultaneously with other state values such as the position and velocity. Additionally, Karlgaard [61] shows that attitude estimation using the MRP is computationally more efficient than other standard techniques such as the quaternion multiplicative filter.

Appendix B

Publications

Accepted for Publication, Refereed Journals

Chapter 2

Olson, C., Russell, R., Carpenter, J.R., "Small Body Optical Navigation Using The Additive Divided Difference Sigma Point Filter," AIAA Journal of Guidance, Control and Dynamics, Vol. 39, No. 4, April 2016, pp. 922-928.

Chapter 4

Olson, C., Russell, R., Bhaskaran, S., "Spin State Estimation of Tumbling Small Bodies," The Journal of the Astronautical Sciences, Vol. 63, No. 2, June 2016, pp. 124-157. 10.1007/s40295-015-0080-y

In Review, Refereed Journals

Chapter 3

Olson, C., Russell, R., Carpenter, J.R., "Precomputing Process Noise For Onboard Sequential Filters," AIAA Journal of Guidance, Control and Dynamics, submitted April 5, 2016.

Planned

Chapter 5

Olson, C., Russell, R., Bhaskaran, S., "Tumbling Small Body Spin State Estimation Using Independently Simulated Images," Journal TBD.

Other Publications

Bhaskaran, S., Nandi, S., Broschart, S., Wallace, M., Alberto Cangahuala, L., and Olson, C., "Small Body Landings Using Autonomous Onboard Optical Navigation," The Journal of the Astronautical Sciences, Vol. 58, No. 3, Sept. 2011, pp. 409–427. 10.1007/bf03321177

Olson, C., "Analysis of Asteroid Landing Capabilities Using Autonomous Optical Navigation," Masters Thesis, The University of Texas at Austin, 2009.

Conference And Presentations

Chapter 2

Olson, C., Russell, R., Carpenter, J.R., "Small Body Optical Navigation Using The Additive Divided Difference Sigma Point Filter," 25th AAS/AIAA Spaceflight Mechanics Meeting, Santa Fe, NM, Jan 2014, AAS 14-422.

Chapter 3

Olson, C., Russell, R., "Precomputing Process Noise for Onboard Sequential Filters," 27th AAS/AIAA Spaceflight Mechanics Meeting, Napa, CA, Feb 2016, AAS 16-475.

Chapter 4

Olson, C., Russell, R., Bhaskaran, S., "Spin State Estimation of Tumbling Small Bodies," 26th AAS/AIAA Spaceflight Mechanics Meeting, Williamsburg, VA, Jan 2015, AAS 15-363.

Other Conference And Presentations

Bhaskaran, S., Nandi, S., Broschart, S., Wallace, M., Cangahuala, L., Olson, C., "Small Body Landing Accuracy Using In-Situ Navigation", AAS Guidance, Navigation, and Control Meeting, Breckenridge, CO, Feb 2011, AAS 11-056.

Olson, C., Wright, C., Long, A., "Expected Navigation Flight Performance for the Magnetospheric Multiscale (MMS) Mission," 23rd AAS/AIAA Spaceflight Mechanics Meeting, Charleston, SC, Jan 2012, AAS 12-199.

Olson, C., Long, A., Carpenter, J. R., "Sensitivity of Magnetospheric Multi-Scale (MMS) Mission Navigation Accuracy to Major Error Sources," 22nd AAS/AIAA Spaceflight Mechanics Meeting, New Orleans, LA, Feb 2011, AAS 11-207.

Olson, C., "Navigation Concepts for the Magnetospheric Multi-Scale (MMS) Mission," AIAA Region I Young Professional, Student, and Education Conference, Applied Physics Laboratory, Laurel, MD, Nov 2011.

Olson, C., Scaperoth, P., "Mission Orbit Navigation Analysis Approach and Modeling Assumptions", NASA Magnetospheric Multi-Scale (MMS) Flight Dynamics Subsystem Critical Design Review (CDR), June 2010.

Bibliography

[1] M. Abrahamson and S. Bhaskaran. Lidar and optical-based autonomous navigation for small body proximity operations. In *25th AAS/AIAA Space Flight Mechanics Meeting*, Santa Fe, NM, 2014. AAS 14-420.

[2] D. Alspach and H. Sorenson. Nonlinear bayesian estimation using gaussian sum approximations. *IEEE transactions on automatic control*, 17(4):439–448, 1972.

[3] P.G. Antreasian, S.R. Chesley, J.K. Miller, J.J. Bordi, and B.G. Williams. The design and navigation of the near shoemaker landing on eros. In *AAS/AIAA Astrodynamics Specialists Conference, Quebec City, Quebec, Canada*, 2001. AAS 01-372.

[4] B.A. Archinal, M.F. A'Hearn, E. Bowell, A. Conrad, G.J. Consolmagno, R. Courtin, T. Fukushima, D. Hestroffer, J.L. Hilton, G.A. Krasinsky, et al. Report of the iau working group on cartographic coordinates and rotational elements: 2009. *Celestial Mechanics and Dynamical Astronomy*, 109(2):101–135, 2011.

[5] N. Arora and R.P. Russell. Fast, efficient and adaptive interpolation of the geopotential. *Advances in the Astronautical Sciences*, 142:1511–1530, 2011.

[6] S.W. Asmar, A.S. Konopliv, R.S. Park, B.G. Bills, R. Gaskell, C.A. Raymond, C.T. Russell, D.E. Smith, M.J. Toplis, and M.T. Zuber. The gravity field of vesta and implications for interior structure. In *Lunar and Planetary Institute Science Conference Abstracts*, volume 43, page 2600, 2012.

[7] E. Asphaug. Critical crater diameter and asteroid impact seismology. *Meteoritics & Planetary Science*, 43(6):1075–1084, 2008.

[8] T. Bailey and H. Durrant-Whyte. Simultaneous localization and mapping (slam): Part ii. *IEEE Robotics & Automation Magazine*, 13(3):108–117, 2006.

[9] T. Bailey, J. Nieto, J. Guivant, M. Stevens, and E. Nebot. Consistency of the ekf-slam algorithm. In *Intelligent Robots and Systems, 2006 IEEE/RSJ International Conference on*, pages 3562–3568. IEEE, 2006.

[10] Y. Bar-Shalom, X.R. Li, and T. Kirubarajan. *Estimation with applications to tracking and navigation: theory algorithms and software*. John Wiley & Sons, 2004.

[11] J. Bauman, K. Getzandanner, B. Williams, and K. Williams. Advanced navigation strategies for an asteroid sample return mission. In *AAS/AIAA Astrodynamics Specialist Conference, Girdwood, Alaska*, 2011.

[12] D. Bayard and P. Brugarolas. An estimation algorithm for vision-based exploration of small bodies in space. In *IEEE American Control Conference*, pages 4589–4595, 2005.

[13] B.M. Bell and F.W. Cathey. The iterated kalman filter update as a gauss-newton method. *IEEE Transactions on Automatic Control*, 38(2):294–297, 1993.

[14] J. Bellerose and D.J. Scheeres. Dynamics and control for surface exploration of small bodies. In *Proceedings of AIAA/AAS 2008 Astrodynamics Specialist Conference*, pages 18–21, 2008.

[15] K. Berry, P. Antreasian, M.C. Moreau, A. May, and B. Sutter. Osiri-rex touch and go (tag) navigation performance. In *38th Annual AAS Guidance and Control Conference*, 2015. AAS 15-125.

[16] K. Berry, B. Sutter, A. May, K. Williams, B.W. Barbee, M. Beckman, and B. Williams. Osiris-rex touch-and-go (tag) mission design and analysis. *Advances in the Astronautical Sciences*, 149:667–678, 2013.

[17] S. Bhaskaran. Autonomous navigation for deep space missions. In *SpaceOps 2012 Conference*, 2012.

[18] S. Bhaskaran et al. Rosetta navigation at comet churyumov-gerasimenko. In *38th AAS GN&C Conference*, 2015. AAS 15-122.

[19] S. Bhaskaran, S. Nandi, S. Broschart, M. Wallace, L.A. Cangahuala, and C. Olson. Small body landings using autonomous onboard optical navigation. *The Journal of the Astronautical Sciences*, 58(3):409–427, 2011.

[20] W.L. Brogan. *Modern control theory*. Pearson Education India, 1974. p. 474.

[21] S.B. Broschart and D.J. Scheeres. Control of hovering spacecraft near small bodies: Application to asteroid 25143 itokawa. *Journal of Guidance, Control, and Dynamics*, 28(2):343–354, 2005.

[22] C. Bruccoleri, D. Lee, and D. Mortari. Single-point optimal attitude determination using modified rodrigues parameters. *Advances in the Astronautical Sciences*, 122:137–147, 2006.

[23] M. Bryson, J. Kim, and S. Sukkarieh. Information and observability metrics of inertial slam for on-line path-planning on an aerial vehicle. In *IEEE international conference on robotics and automation, Spain*, 2005.

[24] S.M. Byram, D.J. Scheeres, and M.R. Combi. Models for the comet dynamical environment. *Journal of Guidance, Control, and Dynamics*, 30(5):1445–1454, 2007.

[25] J.R. Carpenter, S. Hur-Diaz, and F.L. Markley. Generalized covariance analysis of additive divided-difference sigma-point filters. In *AAS/AIAA Spaceflight Mechanics Meeting*, Feb 2011. AAS 11-201.

[26] S. Casotto and R. Casotto. Cartesian development of the gravitational potential within the hotine sphere. In *AAS/AIAA Spaceflight Mechanics Meeting*, Feb 2016. AAS 16-308.

[27] F. Castellini, R. Pardo de Santayana, D. Wokes, and S. Kielbassa. Optical navigation for rosetta operations near comet churyumov-gerasimenko.

In *AAS/AIAA Astrodynamics Specialist Conference*, Hilton Head, SC, 2013. AAS 13-812.

[28] F. Chandler et al. Nasa technology roadmaps, technology area 5: Communications, navigation, and orbital debris tracking and characterization systems, July 2015. Office of Chief Technologist.

[29] L. Chappaz. *The dynamical environment in the vicinity of small irregularly-shaped bodies with application to asteroids*. PhD thesis, PURDUE UNIVERSITY, 2011.

[30] C. Chen. *Linear system theory and design*. Oxford University Press, Inc., 1995. p. 367.

[31] A. Cheng, A. Rivkin, P. Michel, C. Lisse, K. Walsh, K. Noll, D. Ragozzine, C. Chapman, W. Merline, L. Benner, and D. Scheeres. Binary and multiple systems. Technical report, Johns Hopkins University Applied Physics Lab, 2011.

[32] Y. Cheng, D. Clouse, A. Johnson, W. Owen, and A. Vaughan. Evaluation and improvement of passive optical terrain relative navigation algorithms for pinpoint landing. In *AAS/AIAA Spaceflight Mechanics Meeting*, Feb 2011. AAS 11-221.

[33] J.A. Christian and G.E. Lightsey. Onboard image-processing algorithm for a spacecraft optical navigation sensor system. *Journal of Spacecraft and Rockets*, 49(2):337–352, 2012.

[34] J. Civera, A.J. Davison, and J.M.M. Montiel. *Structure from motion using the extended Kalman filter*, volume 75. Springer Science & Business Media, 2011. p.31.

[35] C. Cocaud and T. Kubota. Autonomous navigation near asteroids based on visual slam. In *Proceedings of the 23rd International Symposium on Space Flight Dynamics, Pasadena, California*, 2012.

[36] C. Cocaud and T. Kubota. Slam-based navigation scheme for pinpoint landing on small celestial body. *Advanced Robotics*, 26(15):1747–1770, 2012.

[37] A. Colombi, A.N. Hirani, and B.F. Villac. Adaptive gravitational force representation for fast trajectory propagation near small bodies. *Journal of guidance, control, and dynamics*, 31(4):1041–1051, 2008.

[38] J.L. Crassidis and F.L. Markley. Attitude estimation using modified rodrigues parameters. In *Flight Mechanics/Estimation Theory Symposium*, 1996.

[39] W. Curdt, K. Wilhelm, A. Craubner, E. Krahn, and H.U. Keller. Position of comet p/halley at the giotto encounter. *Astronomy and Astrophysics*, 191:L1–L3, 1988.

[40] K.J. DeMars and R.H. Bishop. Projecting high-dimensional parametric uncertainties for improved state estimation error confidence. *Journal of Guidance, Control, and Dynamics*, 38(9):1659–1672, 2015.

[41] J. Diebel. Representing attitude: Euler angles, unit quaternions, and rotation vectors. *Matrix*, 58:15–16, 2006.

[42] S. Dutta, R. Braun, R. Russell, S. Striepe, and I. Clark. Comparison of statistical estimation techniques for mars entry, descent, and landing reconstruction. *Journal of Spacecraft and Rockets*, 50(6):1207–1221, 2013.

[43] R.W. Gaskell. Automated landmark identification for spacecraft navigation. *Advances in the Astronautical Sciences*, 2002.

[44] R.W. Gaskell, O.S. Barnouin-Jha, D.J. Scheeres, A.S. Konopliv, T. Mukai, S. Abe, J. Saito, M. Ishiguro, T. Kubota, T. Hashimoto, et al. Characterizing and navigating small bodies with imaging data. *AIAA Meteoritics & Planetary Science*, 43(6):1049–1061, 2008.

[45] C.R. Gates. A simplified model of midcourse maneuver execution errors. Technical Report 32-504, Jet Propulsion Laboratory, Pasadena, CA, October 15, 1963.

[46] K. Glassmeier, H. Boehnhardt, D. Koschny, E. Kührt, and I. Richter. The rosetta mission: flying towards the origin of the solar system. *Space Science Reviews*, 128(1-4):1–21, 2007.

[47] B. Godard, F. Budnik, P. Muñoz, T. Morley, and V. Janarthanan. Orbit determination of rosetta around comet 67p/churyumov-gerasimenko. In *25th International Symposium on Space Flight Dynamics*, 2015.

[48] S. Grey and M. Ziebart. Developments in high fidelity surface force models and their relative effects on orbit prediction. American Institute of Aeronautics and Astronautics, 2014. AIAA/AAS Astrodynamics Specialist Conference.

[49] D. Hahnel, R. Triebel, W. Burgard, and S. Thrun. Map building with mobile robots in dynamic environments. In *Robotics and Automation, 2003. Proceedings. ICRA'03. IEEE International Conference on*, volume 2, pages 1557–1563. IEEE, 2003.

[50] C.M. Hartzell and D.J. Scheeres. Dynamics of levitating dust particles near asteroids and the moon. *Journal of Geophysical Research: Planets*, 118(1):116–125, 2013.

[51] T. Hashimoto, T. Kubota, J. Kawaguchi, M. Uo, K. Shirakawa, T. Kominato, and H. Morita. Vision-based guidance, navigation, and control of hayabusa spacecraft-lessons learned from real operation. *IFAC Proceedings Volumes*, 43(15):259–264, 2010.

[52] M. Hawkins and B. Wie. Impact-angle control of asteroid interceptors/penetrators. In *21st AAS/AIAA Space Flight Mechanics Meeting*, pages 2011–271, 2011.

[53] S. Hawkins III. Overview of the multi-spectral imager on the near spacecraft. *Acta Astronautica*, 39(1):265–271, 1996.

[54] W.A. Heiskanen and M. Moritz. *Physical Geodesy*. A series of books in geology. W.H. Freeman, 1967.

[55] D. Idle. *TALON and CRADLE : systems for the rescue of tumbling spacecraft and astronauts : a preliminary design*. PhD thesis, The University of Texas at Austin, 1989.

[56] M. Ishiguro et al. The hayabusa spacecraft asteroid multi-band imaging camera (amica). *Icarus*, 207(2):714–731, 2010.

[57] B.A. Jones, D.S. Bryant, B. Vo, and B. Vo. Challenges of multi-target tracking for space situational awareness. In *Information Fusion (Fusion), 2015 18th International Conference on*, pages 1278–1285. IEEE, 2015.

[58] L. Juan and O. Gwun. A comparison of sift, pca-sift and surf. *International Journal of Image Processing (IJIP)*, 3(4):143–152, 2009.

[59] E. Jurado, A. Blazquez, T. Martin, E. Canalias, R. Garmier, T. Ceolin, J. Biele, and K. Geurts. Rosetta lander philae mission: Flight dynamics studies for landing site selection on comet churyumov âĂŞ gerasimenko. In *24th AAS/AIAA Space Flight Mechanics Meeting*, 2014. AAS 14-357.

[60] P.H. Kallemeyn et al. Galileo orbit determination for the gapra encounter. In *AIAA/AAS Astrodynamics Specialist Conference*, August 1992. AIAA-92-4523.

[61] C.D. Karlgaard and H. Schaub. Nonsingular attitude filtering using modified rodrigues parameters. *The Journal of the Astronautical Sciences*, 57(4):777–791, 2009.

[62] W.M. Kaula. *Theory of Satellite Geodesy: Applications of Satellites to Geodesy*. Dover Earth Science Series. Dover Publications, 2000.

[63] J. Kawaguchi, T. Hashimoto, T. Kubota, S. Sawai, and G. Fujii. Autonomous optical guidance and navigation strategy around a small body. *Journal of Guidance, Control, and Dynamics*, 20(5):1010–1017, 1997.

[64] A.S. Konopliv, S.W. Asmar, B.G. Bills, N. Mastrodemos, R.S. Park, C.A. Raymond, D.E. Smith, and M.T. Zuber. The dawn gravity investigation at vesta and ceres. In *The Dawn Mission to Minor Planets 4 Vesta and 1 Ceres*, pages 461–486. Springer, 2012.

[65] A.S. Konopliv et al. The vesta gravity field, spin pole and rotation period, landmark positions, and ephemeris from the dawn tracking and optical data. *Icarus*, 240:103–117, 2014.

[66] A.S. Konopliv, J.K. Miller, W.M. Owen, D.K. Yeomans, J.D. Giorgini, R. Garmier, and J. Barriot. A global solution for the gravity field, rotation, landmarks, and ephemeris of eros. *Icarus*, 160(2):289–299, 2002.

[67] D. Koschny, R. Solaz, and C. Vallat. Rosetta project glossary, Jan 2007. RO-EST-LI-5012.

[68] T. Kubota, T. Hashimoto, J. Kawaguchi, M. Uo, and K. Shirakawa. Guidance and navigation of hayabusa spacecraft for asteroid exploration and sample return mission. In *2006 SICE-ICASE International Joint Conference*, pages 2793–2796. IEEE, 2006.

[69] T. Kubota, T. Hasimoto, J. Kawaguchi, K. Shirakawa, H. Morita, and M. Uo. Vision based navigation by landmark for robotic explorer. In *Robotics and Biomimetics, 2008. ROBIO 2008. IEEE International Conference on*, pages 1170–1175. IEEE, 2009.

[70] P.L. Lamy, I. Toth, B.J.R. Davidsson, O. Groussin, P. Gutiérrez, L. Jorda, M. Kaasalainen, and S.C. Lowry. A portrait of the nucleus of comet 67p/churyumov-gerasimenko. *Space science reviews*, 128(1-4):23–66, 2007.

[71] A. Landi, F. Boldrini, and D. Procopio. Mars express and rosetta autonomous str: in flight experience. In *Guidance, Navigation and Control Systems*, volume 606, page 55, 2006.

[72] G. Lantoine and R. Braun. Optimal trajectories for soft landing on asteroids. *AE8900 MS Special Problems Report*, 2006.

[73] G. Lanyi, D.S. Bagri, and J.S. Border. Angular position determination of spacecraft by radio interferometry. *Proceedings of the IEEE*, 95(11):2193–2201, 2007.

[74] D. Lee and K.T. Alfriend. Additive divided difference filtering for attitude estimation using modified rodrigues parameters. *Journal of the Astronautical Sciences*, 57(1-2):93–111, 2009.

[75] P. Lee. Dust levitation on asteroids. *Icarus*, 124(1):181–194, 1996.

[76] C. Liebe. Accuracy performance of star trackers-a tutorial. *Aerospace and Electronic Systems, IEEE Transactions on*, 38(2):587–599, 2002.

[77] M.E. Lisano. Nonlinear consider covariance analysis using a sigma-point filter formulation. 2006. AAS 06-035.

[78] A.C. Long and T. Lee. Gps enhanced onboard navigation system (geons) mathematical specifications. Version 3.

[79] J.M. Maciejowski. *Multivariable feedback design*. 1989. p. 223.

[80] N. Mastrodemos, B. Rush, A. Vaughan, and W. Owen Jr. Optical navigation for the dawn mission at vesta. In *Proceedings of the 23rd International Symposium on Space Flight Dynamics, Pasadena, CA, USA, Oct*, 2012.

[81] N. Mastrodemos, B.P. Rush, and W.M. Owen, Jr. Optical navigation for the rosetta mission. In *38th AAS GN&C Conference*, 2015. AAS 15-123.

[82] P.S. Maybeck. *Stochastic models, estimation, and control*, volume 3. Academic press, 1982.

[83] J. McMahon, D. Scheeres, D. Farnocchiaz, and S. Chesley. Optimizing small body gravity field estimation over short arcs. In *AAS/AIAA Astrodynamics Specialist Conference*, 2015. AAS 15-669.

[84] J.W. McMahon and D.J. Scheeres. Improving space object catalog maintenance through advances in solar radiation pressure modeling. *Journal of Guidance, Control, and Dynamics*, 38(8):1366–1381, 2015.

[85] J.K. Miller, A.S. Konopliv, P.G. Antreasian, J.J. Bordi, S. Chesley, C.E. Helfrich, W.M. Owen, T.C. Wang, B.G. Williams, D.K. Yeomans, et al. Determination of shape, gravity, and rotational state of asteroid 433 eros. *Icarus*, 155(1):3–17, 2002.

[86] P. Muñoz, F. Budnik, V. Companys, B. Godard, C.M. Casas, T. Morley, and V. Janarthanan. Rosetta navigation during lander delivery phase and reconstruction of philae descent trajectory and rebound. In *25th International Symposium on Space Flight Dynamics*, 2015.

[87] E. Mysen, A.V. Rodionov, and J.F. Crifo. An analysis of outgassing pressure forces on the rosetta orbiter using realistic 3d coma simulations. *Astronomy and Astrophysics*, 512:69, 2010.

[88] M. Nørgaard, N.K. Poulsen, and O. Ravn. Advances in derivative-free state estimation for nonlinear systems. Technical Report IMM REP 1998 15, Technical University of Denmark, 2800 Lyngby, Denmark, 2000.

[89] M. Nørgaard, N.K. Poulsen, and O. Ravn. New developments in state estimation for nonlinear systems. *Automatica*, 36(11):1627–1638, 2000.

[90] C. Olson. Analysis of Asteroid Landing Capabilities Using Autonomous Optical Navigation. Master's thesis, The University of Texas at Austin, Austin, TX, 2009.

[91] C. Olson, R. Russell, and S. Bhaskaran. Spin state estimation of tumbling small bodies. *The Journal of the Astronautical Sciences*, 2016.

[92] C. Olson, R. Russell, and J. Carpenter. Small body optical navigation using the additive divided difference sigma point filter. In *25th AAS/AIAA Space Flight Mechanics Meeting*, 2014. AAS 14-422.

[93] C. Olson, R. Russell, and J. Carpenter. Small body optical navigation using the additive divided difference sigma point filter. *Journal of Guidance, Control, and Dynamics*, 2015. Accepted Sept 2015.

[94] C. Olson, C. Wright, and A. Long. Expected navigation flight performance for the magnetospheric multiscale (mms) mission. In *22nd AAS/AIAA Space Flight Mechanics Meeting*, 2012. AAS 12-199.

[95] W.M. Owen, Jr. Methods of optical navigation. In *21st AAS/AIAA Space Flight Mechanics Meeting*, New Orleans, LA, 2011. AAS 11-215.

[96] R. Pardo de Santayana and M. Lauer. Optical measurements for rosetta navigation near the comet. In *25th International Symposium on Space Flight Dynamics*, 2015.

[97] P. Pravec, A.W. Harris, D. Vokrouhlickỳ, B.D. Warner, P. Kušnirák, K. Hornoch, D.P. Pray, D. Higgins, J. Oey, A. Galád, et al. Spin rate distribution of small asteroids. *Icarus*, 197(2):497–504, 2008.

[98] J. Riedel, T. Wang, R. Werner, A. Vaughan, D. Myers, N. Mastrodemos, G. Huntington, C. Grasso, R. Gaskell, and D. Bayard. Configuring the deep impact autonav system for lunar, comet and mars landing. In *AIAA/AAS Astrodynamics Specialist Conference and Exhibit, Honolulu, Hawaii*, 2008. AIAA 2008-6940.

[99] M.S. Robinson, P.C. Thomas, J. Veverka, S. Murchie, and B. Carcich. The nature of ponded deposits on eros. *Nature*, 413(6854):396–400, 2001.

[100] C.T. Russel, C.A. Raymond, T.C. Fraschetti, M.D. Rayman, C.A. Polanskey, K.A. Schimmels, and S.P. Joy. Dawn mission and operations. *Proceedings of the International Astronomical Union*, 1(S229):97–119, 2005.

[101] C. Russell et al. Dawn mission to vesta and ceres. *Earth, Moon, and Planets*, 101(1-2):65–91, 2007.

[102] R. Russell. Survey of spacecraft trajectory design in strongly perturbed environments. *Journal of Guidance, Control, and Dynamics*, 35(3):705–720, 2012.

[103] R. Russell, D. Lantukh, and S. Broschart. Heliotropic orbits with zonal gravity and shadow perturbations: Application at bennu. *Journal of Guidance, Control, and Dynamics*. To appear.

[104] R. P. Russell. Missions to dynamic environments. In D.J. Scheeres, R. Blockley, and W. Shyy, editors, *Encyclopedia of Aerospace Engineering*, pages 3123–3138. John Wiley and Sons Ltd, Chichester, UK, 2010.

[105] R.P. Russell and N. Arora. Global point mascon models for simple, accurate, and parallel geopotential computation. *Journal of Guidance, Control, and Dynamics*, 35(5):1568–1581, 2012.

[106] D. Scheeres, R. Gaskell, S. Abe, O. Barnouin-Jha, T. Hashimoto, J. Kawaguchi, T. Kubota, J. Saito, M. Yoshikawa, N. Hirata, et al. The actual dynamical environment about itokawa. 2006.

[107] D. Scheeres, A. Rosengren, and J. Mcmahon. The dynamics of high area-to-mass ratio objects in earth orbit: the effect of solar radiation pressure. *Spaceflight Mechanics*, 140, 2011.

[108] D.J. Scheeres. Orbit mechanics about asteroids and comets. *Journal of Guidance Control and Dynamics*, 35(3):987, 2012.

[109] D.J. Scheeres. Orbital mechanics about small bodies. *Acta Astronautica*, 72:1–14, 2012.

[110] D.J. Scheeres. *Orbital Motion in Strongly Perturbed Environments*. Springer, 2012.

[111] D.J. Scheeres, C.M. Hartzell, P. Sánchez, and M. Swift. Scaling forces to asteroid surfaces: The role of cohesion. *Icarus*, 210(2):968–984, 2010.

[112] D.J. Scheeres and R.L. Schweickart. The mechanics of moving asteroids. In *2004 Planetary Defense Conference: Protecting Earth from Asteroids*, pages 23–26, 2004.

[113] D.J. Scheeres, B.G. Williams, and J.K. Miller. Evaluation of the dynamic environment of an asteroid: Applications to 433 eros. *Journal of Guidance, Control, and Dynamics*, 23(3):466–475, 2000.

[114] F.H. Schlee and N.F. Toda. Autonomous orbital navigation by optical tracking of unknown landmarks. *Journal of Spacecraft and Rockets*, 4(12):1644–1648, 1967.

[115] S.F. Schmidt. Applications of state space methods to navigation problems. *Advances in Control Systems*, 3:293–340, 1966.

[116] P.K. Seidelmann, B.A. Archinal, M.F. AâĂŹhearn, A. Conrad, G.J. Consolmagno, D. Hestroffer, J.L. Hilton, G.A. Krasinsky, G. Neumann, J. Oberst, et al. Report of the iau/iag working group on cartographic coordinates and rotational elements: 2006. *Celestial Mechanics and Dynamical Astronomy*, 98(3):155–180, 2007.

[117] D. Sheinfeld and S. Rock. Rigid body inertia estimation with applications to the capture of a tumbling satellite. In *19th AAS/AIAA Space Flight Mechanics Meeting*, 2009. AAS 09-123.

[118] D. Simon. *Optimal state estimation: Kalman, H infinity, and nonlinear approaches*. John Wiley & Sons, 2006.

[119] J. Stauch and M. Jah. Unscented schmidt–kalman filter algorithm. *Journal of Guidance, Control, and Dynamics*, 38(1):117–123, 2014.

[120] Y. Takahashi, D.J. Scheeres, and R.A. Werner. Surface gravity fields for asteroids and comets. *Journal of Guidance, Control, and Dynamics*, 36(2):362–374, 2013.

[121] B.D. Tapley, B.E. Schutz, and G.H. Born. *Statistical Orbit Determination*. Elsevier Academic Press, 2004.

[122] S. Tardivel and D.J. Scheeres. A strategy for landings on small binary bodies: Application to asteroid system 1999 kw 4. *Spaceflight Mechanics*, 140, 2011.

[123] P.C. Thomas and M.S. Robinson. Seismic resurfacing by a single impact on the asteroid 433 eros. *Nature*, 436(7049):366–369, 2005.

[124] S. Thrun, Y. Liu, D. Koller, A.Y. Ng, Z. Ghahramani, and H. Durrant-Whyte. Simultaneous localization and mapping with sparse extended information filters. *The International Journal of Robotics Research*, 23(7-8):693–716, 2004.

[125] P. Tricarico and M.V. Sykes. The dynamical environment of dawn at vesta. *Planetary and Space Science*, 58(12):1516–1525, 2010.

[126] C. Tubiana. *Characterization of the physical properties of the ROSETTA target comet 67P/Churyumov-Gerasimenko*. Copernicus Publ., 2008.

[127] D.A. Vallado and W.D. McClain. *Fundamentals of Astrodynamics and Applications*. Managing Forest Ecosystems. Springer, 2001.

[128] R. Van Der Merwe and E.A. Wan. The square-root unscented kalman filter for state and parameter-estimation. In *Acoustics, Speech, and Signal Processing, 2001. Proceedings.(ICASSP'01). 2001 IEEE International Conference on*, volume 6, pages 3461–3464. IEEE, 2001.

[129] R.M. Vaughn, J.E. Riedel, R.P. Davis, W.M. Owen, Jr., and S.P. Synnott. Optical navigation for the galileo gaspra encounter. In *AIAA/AAS Astrodynamics Specialist Conference*, August 1992. AIAA-92-4522.

[130] J. Veverka, M. Belton, K. Klaasen, and C. Chapman. Galileo's encounter with 951 gaspra: Overview. *Icarus*, 107(1):2–17, 1994.

[131] C. Wang, C. Thorpe, and S. Thrun. Online simultaneous localization and mapping with detection and tracking of moving objects: Theory and results from a ground vehicle in crowded urban areas. In *Robotics and Automation, 2003. Proceedings. ICRA'03. IEEE International Conference on*, volume 1, pages 842–849. IEEE, 2003.

[132] J.D. Weiss and D.S. Kee. A direct performance comparison between loosely coupled and tightly coupled gps/ins integration techniques, 04 1995. TY: CPAPER; SuppNotes - Proceedings (A96-14001 02-32; Last updated - 2011-11-11.

[133] R.A. Werner. Spherical harmonic coefficients for the potential of a constant-density polyhedron. *Computers & Geosciences*, 23(10):1071–1077, 1997.

[134] R.A. Werner and D.J. Scheeres. Exterior gravitation of a polyhedron derived and compared with harmonic and mascon gravitation representations of asteroid 4769 castalia. *Celestial Mechanics and Dynamical Astronomy*, 65(3):313–344, 1996.

[135] W.E. Wiesel. *Spaceflight Dynamics*. McGraw-Hill series in aeronautical and aerospace engineering. McGraw-Hill, 1997.

[136] B. Williams, P. Antreasian, J. Bordi, E. Carranza, S. Chesley, C. Helfrich, J. Miller, M. Owen, and T. Wang. Navigation for near shoemaker

- the first spacecraft to orbit an asteroid. *Advances in the Astronautical Sciences*, pages 973–988, 2002.

[137] B.G. Williams. Technical challenges and results for navigation of near shoemaker. *Johns Hopkins APL technical digest*, 23(1):34–45, 2002.

[138] D. Wokes and J. Essert. Development of rosetta's initial stage comet rendezvous guidance systems. In *AIAA/AAS Astrodynamics Specialist Conference*, 2012.

[139] J. Woodburn, J. Carrico, and J.R. Wright. Estimation of instantaneous maneuvers using a fixed interval smoother. *Advances in the Astronautical Sciences*, 116:243–260, 2003.

[140] D. Woodbury and J. Junkins. On the consider kalman filter. In *AIAA Guidance, Navigation, and Control Conference*, page 7752, 2010.

[141] J.R. Wright. Sequential orbit determination with auto-correlated gravity modeling errors. *Journal of Guidance, Control, and Dynamics*, 4(3):304–309, 1981.

[142] H. Yano, T. Kubota, H. Miyamoto, T. Okada, D. Scheeres, Y. Takagi, K. Yoshida, M. Abe, S. Abe, O. Barnouin-Jha, et al. Touchdown of the hayabusa spacecraft at the muses sea on itokawa. *Science*, 312(5778):1350–1353, 2006.

[143] T. Yoshimitsu, J. Kawaguchi, T. Hashimoto, T. Kubota, M. Uo, H. Morita, and K. Shirakawa. Hayabusa-final autonomous descent and landing

based on target marker tracking. *Acta Astronautica*, 65(5):657–665, 2009.

[144] R. Zanetti. Recursive update filtering for nonlinear estimation. *IEEE Transactions on Automatic control*, 57(6):1481–1490, 2012.

[145] R. Zanetti, K. DeMars, and R. Bishop. Underweighting nonlinear measurements. *Journal of Guidance, Control, and Dynamics*, 33(5):1670–1675, 2010.

[146] R. Zanetti and K.J. DeMars. Joseph formulation of unscented and quadrature filters with application to consider states. *Journal of Guidance, Control, and Dynamics*, 36(6):1860–1864, 2013.

Vita

Corwin Grant Olson was born in Dallas, Texas. As an undergraduate student at the University of Texas at Austin, he worked as a co-operative education student in 2005 and 2006 for United Space Alliance at NASA's Johnson Space Center. There he worked in the International Space Station Training Division, becoming a certified instructor in three courses. He graduated with a Bachelor of Science degree in Aerospace Engineering from the University of Texas at Austin in 2007. He received a Master of Science degree in Aerospace Engineering from the University of Texas at Austin in 2009. He worked as an Aerospace Engineer for a.i. solutions from 2009 to 2012, performing navigation and mission design analysis for the NASA Magnetospheric Multi-Scale mission. He began his PhD at the University of Texas at Austin in 2012, and was awarded a NASA Space Technology Research Fellowship for graduate studies. As part of the fellowship, he visited NASA's Goddard Space Flight Center, Jet Propulsion Laboratory, and Ames Research Center for extended periods to work with NASA mentors and colleagues on research problems relevant to NASA missions.

Permanent address: corwinolson-at-gmail.com

This dissertation was typeset with LaTeX[†] by the author.

[†]LaTeX is a document preparation system developed by Leslie Lamport as a special version of Donald Knuth's TeX Program.